Chair of Physics

Master's Thesis

Preparation and 3D – characterization of porous $BaTiO_3$

Philipp Aldo Wieser, BSc

November 2019

AFFIDAVIT

I declare on oath that I wrote this thesis independently, did not use other than the specified sources and aids, and did not otherwise use any unauthorized aids.

I declare that I have read, understood, and complied with the guidelines of the senate of the Montanuniversität Leoben for "Good Scientific Practice".

Furthermore, I declare that the electronic and printed version of the submitted thesis are identical, both, formally and with regard to content.

Date 28.11.2019

Signature Author
Philipp Aldo, Wieser

Acknowledgement

I would like to offer my special thanks to my supervisor, Priv. Doz. Dr. Roland Brunner (Materialcenter Leoben Forschung GmbH, Leoben, Austria and Institute of Physics, Montanuniversität Leoben, Austria), for his expert advice and encouragement throughout this difficult project.

Also, I would like to thank Dr. Marco Deluca (Materialcenter Leoben Forschung GmbH, Leoben, Austria) and Dr. Vincenzo Buscaglia (CNR-ICMATE, Genoa, Italy) for their support in this thesis project.

I would like to express thanks Dr. Maria Teresa Buscaglia, Dr. Giovanna Canu and Mag. Jördis Rosc for their technical and scientific support in this work. I would like to thank particularly Dr. Giovanna Canu for her patience with me in the laboratory.

I would also like to thank Dr. Fereshteh Falah Chamasemani, MSc. Thomas Vorauer, MSc. Andi Wijaya and MSc. Vignaswaran Kaliyaperumal Veerapandiyan for their support and collaboration. You supported me greatly and were always willing to help me.

This work would have been impossible without the financial support of the COMET-program in the K2 centre „Integrated Computational Material, Process and Product Engineering (IC-MPPE)“ (Projektnummer 859480) and the JECS Trust of the European Ceramic Society through grant N.2018171 to perform the production of porous ceramic samples at the CNR-ICMATE, Genoa (Italy).

I would also like to thank my family, Dr. Clemens Wieser and Dr. Silvia Wieser-Mitzner, for their financial and emotional support as well as my sister, Laura Wieser, and my friends and colleagues. You were a great support throughout the whole period of my studies and my life.

Die vorliegende Arbeit wurde am Materialcenter Leoben Forschung GmbH im Rahmen von COMET (Proj.Nr. kp860-04) sowie in Kooperation mit der Forschungseinrichtung CNR-ICMATE, Genua (Italien), im Rahmen von JECS-TRUST (Förderung Nr.2018171) durchgeführt.

Der Autor bedankt sich für die finanzielle Unterstützung im Rahmen des COMET-Programms im K2 Zentrum „Integrated Computational Material, Process and Product Engineering (IC-MPPE)“ (Projektnummer 859480). Dieses Programm wird von den österreichischen Bundesministerien für Verkehr, Innovation und Technologie (BMVIT) und für Digitalisierung und Wirtschaftsstandort (BMDW), vertreten durch die österreichische Forschungsförderungsgesellschaft (FFG), und den Bundesländern Steiermark, Oberösterreich und Tirol gefördert. Desweiter bedankt er sich für die finanzielle Unterstützung durch JECS-Trust.

Abstract

The aim of this work was to produce porous $BaTiO_3$ ceramics with defined porosity and pore morphology for application as dielectrics/ferroelectrics. The porosity was designed via the so-called pore forming method, which includes the mixing of the ceramic powder with a pore former. The pore former is then burned out in the sintering process, yielding pores in the ceramic. To attain different pore morphologies and porosity two different types of pore formers were added to the $BaTiO_3$, namely graphite and corn starch. In addition, the pore former content was varied. The resulting microstructure was analysed using 2D and 3D imaging methods. A chemical analysis was performed via RAMAN spectroscopy.

Conclusion:

-The analysis of the pore structure in 3D led to a clear distinction of the pore morphology, i.e. pore size and shape, of the samples.

-Samples produced with graphite had more elongated pores than samples produced with corn starch.

-The morphology was also influenced by adding a pore former or changing the mixing medium. Both led to higher pore sizes and less elongated pores in the samples produced with graphite.

-The porosity of the samples increased with the amount of the pore former.

-The analysis of the RAMAN spectra provides information regarding the orthorhombic phase.

-Changing the pore former did not affect the chemical composition of the samples.

Kurzfassung

Ziel dieser Arbeit war es, poröse $BaTiO_3$ - Keramiken herzustellen, die eine definierte Porosität und Porenmorphologie aufweisen. Diese Keramiken finden Anwendung als Ferroelektrika/Dielektrika. Porosität und Porenmorphologie wurden mittels sogenannter Pore-forming Methode eingestellt, bei welcher das Keramik-Pulver mit einem Poreformer gemischt wird. Der Poreformer wird im Sinterprozess ausgebrannt und hinterlässt Poren in der Keramik. Um unterschiedliche Porenmorphologien und Porositäten in der Keramik zu erhalten, wurden unterschiedliche Poreformer hinzugefügt, Graphit und Maisstärke. Außerdem wurde der Poreformergehalt der Mischung variiert. Die resultierende Mikrostruktur wurde mittels bildgebender Verfahren in 2D und 3D analysiert. Die chemische Analyse wurde mittels RAMAN-Spektroskopie durchgeführt.

Schlussfolgerungen der Untersuchungen:

-Die Analyse der Porenstruktur in 3D führte zu einer klaren Unterscheidung der Porenmorphologie, d.h. der Porengröße und -form, der Proben.

-Proben, die mit Graphit hergestellt wurden, weisen länglichere Poren auf als Proben, die mit Maisstärke hergestellt wurden.

-Die Porenmorphologie wurde durch das Hinzufügen eines Binders und durch Änderung des Mischmediums beeinflusst. Beide führten zu höheren Porengrößen und weniger länglichen Poren in Proben, die mit Graphit hergestellt wurden.

-Die Porosität stieg mit höherem Poreformergehalt.

-Analysen der RAMAN-Spektren geben Aufschluss über die orthorombische $BaTiO_3$-Phase der Matrix.

-Die Änderung des Poreformers hatte keinen Einfluss auf die chemische Zusammensetzung der Proben.

Content

1 Introduction

Producing ceramics, usually a porosity as low as possible is desired. This way, a reduced critical flaw content and consequently a higher mechanical strength of the ceramic is achieved [1]. However, porous ceramics offer a wide range of interesting properties. Therefore, they are promising materials for several structural and functional applications, such as thermal insulation and filtration systems, and their range of use is still expanding into other areas [2]. Porous ceramics have been studied regarding their electrical properties, for example porous piezoelectric PZT ceramics [3] or $BaTiO_3$-based materials [4]. Also ceramic cathode materials used in solid oxide fuel cells have been investigated regarding their mechanical properties after introducing porosity [5].

The wide range of functionalities requires distinct properties of the porous material. Parameters regarding the pore structure, such as pore size, shape, distribution and connectivity play an important role in changing the properties of the porous material [2,6]. For example, filtration membranes have an open cell structure to allow fluid flow, while ceramics for thermal insulation have a closed cell structure. To achieve distinct pore structures there are several processing techniques [2][7].

In the present work, the pore forming method is used to produce porous ceramic samples. This method includes mixing of the ceramic powder with a pore former, which is then burned out in the sintering process, yielding pores in the ceramic. This method yields three-dimensionally interconnected pores [3,7] with reported porosity of up to 52% [3]. The pore size and shape changes depending on the pore former [3].

3D – characterization methods such as X-ray computed tomography or FIB-SEM tomography are promising methods to analyse three-dimensional structures such as pores. X-ray computed tomography is commonly used in earth sciences to analyse the porosity of rocks [8]. In metals, it has been applied to investigate pores introduced by accident (e.g. in welding [9]) or on purpose (e.g. metal foams[10] [11]). In ceramics, microstructural characteristics of ceramic films with different porosities were characterized via FIB-SEM tomography [5]. The studies were combined with FEM simulations of the elastic moduli. Holzer et al. [12] investigated porous $BaTiO_3$ regarding porosity and pore size distribution via FIB-SEM tomography and compared results to mercury intrusion porosimetry.

$BaTiO_3$-based materials, such as $(Ba,Sr)TiO_3$, were investigated regarding their change in microstructure and permittivity with increasing porosity [4]. The microstructure was investigated via phase analysis with X-ray diffraction and scanning electron microscopy of the fractured surface. The permittivity was also measured on porous PZT materials, and simulations of the measurement have been performed [7,13]. Olariu et al. [7] measured the dielectric constant of porous $Pb(Zr,Ti)O_3$ samples with elongated pores and compared it to simulations via finite element method.

Due to its high relative dielectric constant and its low losses, $BaTiO_3$ is used in the microelectronic industry in multi-layered chip capacitors (MLCC) as a dielectric [14],[15]. Donor-doped $BaTiO_3$ based ceramics show a positive temperature coefficient of resistivity

(PTCR) [16]. The introduction of porosity substantially improved the PTCR characteristics [17]. Porous $BaTiO_3$-based ceramics are potential candidates for ceramic gas and humidity sensors. Also, $BaTiO_3$ ceramics are potentially a lead-free alternative for lead zirconate titanate (PZT) in piezoelectric applications [18].

The aim of this work is to produce porous $BaTiO_3$ ceramics with defined porosity and pore morphology using different pore formers. The distribution of the pores in the sample and the pore morphology, i.e. the pore size and shape, are then analysed using 2D and 3D characterization methods, and a chemical analysis is done.

The porosity is introduced via pore forming method which allows the formation of distinct pore morphology, i.e. distinct pore shape and size. The pore formers are corn starch and graphite, added at different percentages to the $BaTiO_3$-powder before pressing and sintering. The pore forming method is described in sections 3.1 to 3.3. The effect of the different pore formers and other parameters regarding the processing of the samples on the microstructure were analysed via 2D (i.e. scanning electron microscopy, SEM) and 3D (i.e. X-ray computed microtomography, µ-XCT) characterization methods. The porosity is measured via µ-XCT, with Archimedes method and by calculating its density from weight and volume measurements of the samples. The microstructure is qualitatively investigated with a scanning electron microscope (SEM). The pore-size distribution is analysed via µ-XCT. The spatial distribution of the pores and the interconnectivity is analysed on skeletonized 3D representations of the samples. The chemical analysis is performed via RAMAN spectroscopy.

2 Theoretical part

2.1 Overview of processing techniques of porous ceramics

The processing of porous materials has become an important field in materials science. Processing routes have been investigated for porous metals [19], polymers (i.e. porous organic materials) [20] and ceramics (i.e. inorganic non-metallic materials). In the present work, the focus is put on porous ceramics. In the field of porous ceramics, there is a variety of different processing routes, each yielding a different pore morphology.

Galassi [21] wrote a review on processing porous ceramics, focusing on piezoelectric PZT (lead zirconate titanate) ceramics, which as ferroelectrics with a Perowskite chrystal structure are similar to $BaTiO_3$.

According to Galassi, porous ceramics can be classified regarding their pore size (from the order of nanometres to several millimetres) and basic pore structure (open cell structure, closed cell structure). At very high porosity degrees, the porous ceramic is also called reticulated ceramic.

Galassi distinguishes between dry and wet processing methods. The wet processing methods involve the preparation of a colloidal suspension [22,23], where the ceramic powder is dispersed in a liquid with dispersant, binders, plasticizers pore forming agents etc. The rheological properties of the slurry enable a high flexibility in the design of porous ceramics, with techniques such as solid freeform fabrication [23], sol-gel processing [24] and casting of slurries with different types of pore-forming agents [25].

The dry processing methods include the partial sintering technique [26] and the pore forming method [3]. For the partial sintering technique, the thermal treatments involve only microstructure evolution and no chemical change of phase (such as burning of a phase). The ceramic powder is compacted to a green in a pressing step. Then, the green is sintered. As indicated by the name of the technique, the sintering process is not complete. The particles form a strong bond or neck, but the sintering of the ceramic proceeds only to a certain point. The resulting ceramic contains a high amount of porosity. The porosity of the ceramic can be controlled by changing the sintering degree [1]. The pore size can be controlled by changing the particle size of the ceramic powder.

The pore forming method is reported to yield ceramics with three-dimensionally-interconnected porosity [3]. Pores are introduced by adding appropriate amounts of organic or fugitive substances (i.e. pore formers) to the ceramic powder before pressing and sintering. Pore formers can be poly vinyl butyral (PVB) [27], methyl-hydroxyethyl-cellulose (MHEC) [3], graphite [17], corn starch [28] or potato [29] starch. The ceramic powder and the pore former are mixed, dried and pressed. In the sintering step, the pore former is then burned out yielding voids in the ceramic.

2.2 Computed Tomography

2.2.1 Computed Tomography – fields of use

Computed tomography (CT) is a common method to perform 3D-characterisation in various fields of research. In Palaeontology, the CT scan is a useful tool because it allows three-dimensional reconstructions of skeletons without having to manipulate the pieces [30]. The same argument counts for heritage sciences [31], where it is potentially used in combination with 3D printers to create exact replicas of ancient relics [32]. It is a well-established diagnostic method in the medical field; there are numerous commercially available CT scanners for medical applications [33], and there is a wealth of ongoing research [34]. In earth sciences and rock mineralogy, investigations are currently applying CT scan technology to evaluate the porosity of rocks [8]. Porosity is a very important parameter in rocks as it is strongly linked to their water absorption capacity [35].

In physical metallurgy, CTs were used to analyse the mechanical behaviour of porous metals, in combination with 3D FEM simulations [10]. CTs were used to characterize composite metals, i.e. metals composed of foamy metallic matrix and fibres or particles added to improve their strength and rigidity [11]. In welding, CTs were used to detect the presence or absence of large pores [9].

CT is of growing importance in the ceramics industry. Particularly in nanotechnology, there is an increasing demand for 3D characterization, which is “the basis for parametrization and quantification of microstructural features” [12]. Holzer et al. [12] investigated porous $BaTiO_3$ regarding porosity and pore size distribution. Yan et al. [36] studied $Ni/BaTiO_3$ multilayers using µ-XCT and FIB-SEM tomography. Chen et al. [5] studied the microstructural characteristics of ceramic films with different porosities via FIB-SEM tomography and performed FEM simulations of the elastic moduli.

2.2.2 Challenge – characterization and parametrization of porous structures

The main challenge in the characterization of porous structures is “to describe properties of the pore-network in a reliable way without destroying or altering the samples” [37]. The most common measure to describe a porous structure is the porosity [4,5], which is mostly determined using the fraction of pore volume to the total volume or with the relative density of the sample (density of the sample relative to the theoretical density of the substrate). Depending on the preparation technique and on the material, the pores have different sizes and shapes (i.e. pore morphology) [3]. Also, the pore connectivity is a common parameter to describe the properties of a pore-network [38]. Studies of Stanculescu et al. [4] found a strong decrease in effective permittivity of ceramic samples with increasing porosity. Local variations in the porosity, i.e. the spatial distribution of pores, might also play a role in characterization of the pore network. Parameters regarding the characterization of porous structures are summed in Figure 1.

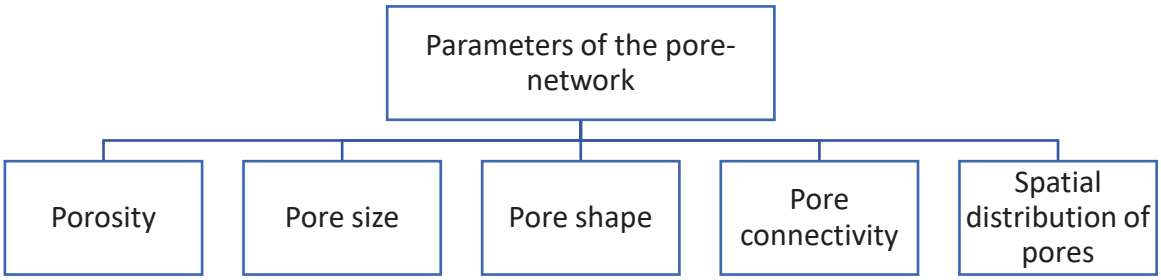

Figure 1:Summary of parameters to describe a porous network.

2.2.3 X-ray computed microtomography - Principle of use

The principle of a µ-XCT scan is shown in Figure 2. X-ray radiation from a tube source traverses the sample to be measured. Passing through the sample, it is attenuated according to the law of Beer [39]. According to Beer's law, the intensity I of the outcoming X-ray beam is to be calculated as in equation (1):

$$I = I_0 \cdot e^{-\int \mu(s) \cdot ds} \qquad (1)$$

Where I_0 is the incoming intensity and $\mu(s)$ is the linear attenuation coefficient along the trajectory s of the beam. The quotient of μ/ρ correlates with Z^3, where ρ is the density and Z the atom number of the traversed material.

A radioscopic image of the sample is then projected on an X-ray detector. The radioscopic image is taken several times on the sample, from different angles. This is done by rotating the sample or the source of radiation and the detector. The 2D images are then reconstructed to a three-dimensional digital image, using mathematical principles of tomography [40,41]. Each voxel, i.e. volume pixel, represents the X-ray absorption at that point.

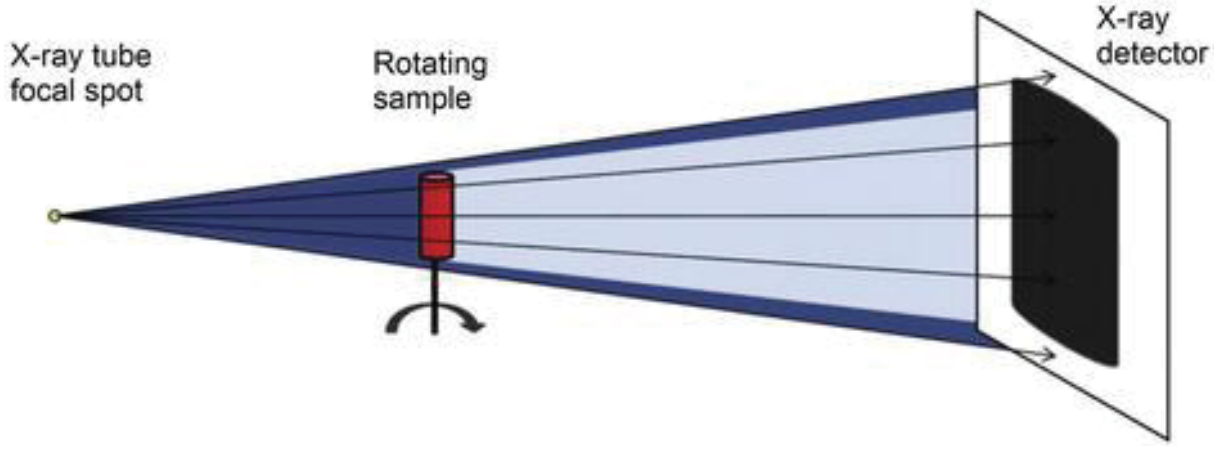

Figure 2:Operation principle of a CT scan [42]. X-ray radiation from a tube source traverses the sample to be measured. Passing through the sample, it is attenuated according to the law of Beer [39]. A radioscopic image of the sample is then projected on an X-ray detector.

2.2.4 Comparison of µ-XCT with other 3D characterization methods

Beside µ-XCT scans, there are several other ways to analyse pore-networks. Often, indirect methods such as helium, nitrogen or mercury injection porosimetry are used to determine

porosity, pore size distribution [3] and interconnectivity [38] of pores. However, this method is limited in comparison to the 3D imaging approach as closed porosity cannot be reached by helium, nitrogen or mercury, whereas 3D image analysis enables the characterization of the total pore content of the sample [43]. Measuring the pore size distribution, mercury injection porosimetry is strongly affected by the geometry of pore necks. This so-called ink-bottle effect is an important source of error in measuring the pore size distribution [44]. Holzer et al. [12] reported differences in porosity measured with mercury intrusion porosimetry and FIB-SEM tomography.

2D representations of the samples, i.e. cross-sections, are often used to characterize the porosity of a sample, e.g. with scanning electron microscopy [3]. However, for complex pore-networks the results may lead to misinterpretation of the images [45].

The synchrotron µCT operates on the same principle as a laboratory µ-XCT. The difference is that the light source is an X-ray beam emitted via synchrotron radiation [37]. According to Ramos et al. [37], it is more efficient at detecting small details i.e. it requires shorter scanning time as synchrotron radiation exhibits radiation of higher brilliance. The trade-off of a synchrotron µ-XCT is the availability since you need synchrotron radiation for the set-up.

The set-up for FIB-SEM tomography consists in a scanning electron microscope to scan the surface of the sample to be measured and a focused ion beam to erode slice by slice the material of the sample. Potentially, FIB-SEM tomography offers a higher resolution compared to µ-XCT [12]. A trade-off however is that the method is destructive. Moreover, FIB-SEM tomography scans are limited in their scanning range (up to 100 μm^3). In some applications, the typical scanning range is smaller than the characteristic length scales of spatial homogeneity of the material to be measured [46].

2.3 Application of analysis algorithms to 3D data

In the present work, several algorithms and methods were applied to enable the analysis attained from µ-XCT. Generally, the processing of 3D data can be subdivided into several steps:

- **Pre-processing:** is needed to enhance the signal to noise ratio of the CT scans. It includes image enhancement with filters, a histogram alignment and (if needed) image step alignment.
- **Segmentation:** is the process of binarizing the scan. There are several methods to binarize the CT scans.
- **Post-processing:** After binarizing the image, there are several techniques to extract data and parameters of the scan.

2.3.1 Pre-processing

Non-local-means filter

According to the Avizo user's manual [47], "this filter is extremely effective on noisy data while preserving edges (best with white noise). However, it can be very time consuming."

The median filter

The median filter is effective in removing salt-and-pepper noise (i.e. sharp disturbances in the image) [48]. It works by identifying the median grey value of the neighbourhood of a pixel (or voxel), which is the new value of the pixel. A problem of the median filter is that it fails to distinguish thin lines and boundaries from noise, which results in filtering out of fine details [49].

Opening

The opening algorithm is a combination of erosion and dilation of the (binarized) image [50]. In erosion, a pixel is set to 0 if any of the neighbouring pixels have the value 0. Morphological erosion removes islands and small objects so that only substantive objects remain. In dilation, a pixel is set to 1 if any of the neighbouring pixels have the value 1. Morphological dilation makes objects more visible and fills in small holes in objects.

2.3.2 Segmentation

Watershed segmentation

Watershed segmentation is a method to segment greyscale images [51]. The grayscale image can be viewed as a topographic surface, with high intensity indicating peaks and hills and low intensity indicating valleys. The valleys are filled with water. The level of the water rises till the valleys are filled and merge. The merging lines (i.e. watershed) are the segmentation results.

Otsu's method

Otsu's method is a histogram-based segmentation method. [52] It returns a grey value threshold that separates pixels (or voxels) into two classes, fore ground and background. The threshold is determined by minimizing intra-class intensity variance, or equivalently, by maximizing inter-class variance. [53]

2.3.3 Post-processing

Skeletonization

Skeletonization shown in Figure 3. It is the process of reducing foreground regions in a binary image to a skeletal remnant [54]. This is done making successive passes of the image. At each pass, border pixels are identified and removed (eroded) on the condition that they do not break the connectivity of the object. At collision points of the eroding flanks, the resulting skeleton is produced. [55]

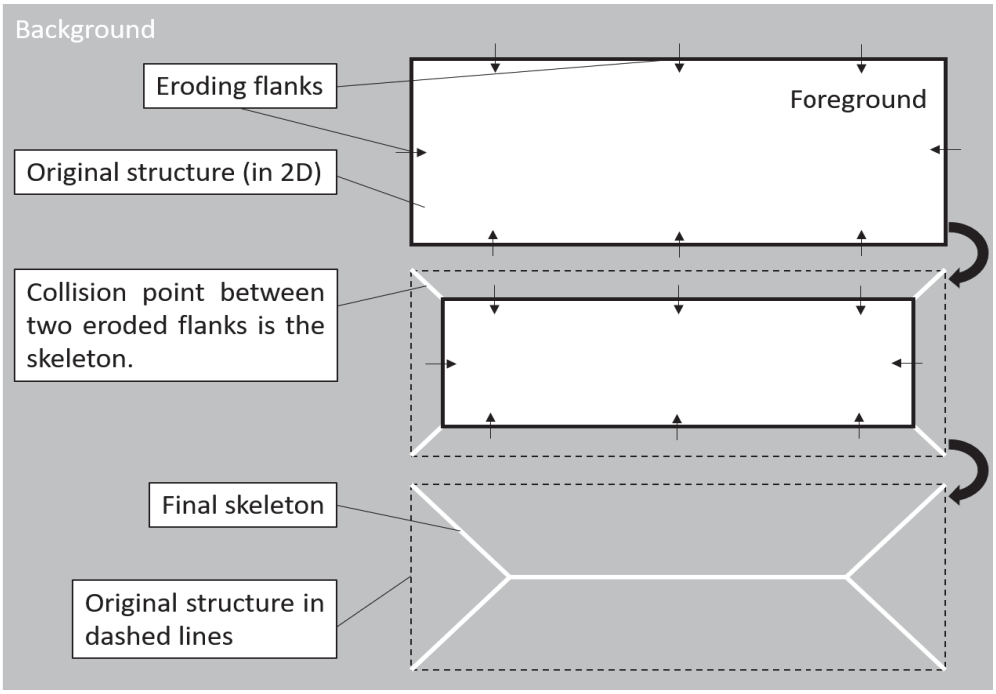

Figure 3: Schematic representation of the skeletonization process in 2D. The foreground object is eroded until eroding flanks collide. The resulting structure is the skeleton.

Feret diameter

In mineralogy, the Feret diameter is already a well-established method to characterize particle sizes, e.g. in static or dynamic image analysis [56]. An illustration of the measurement of the Feret diameter is illustrated in Figure 4. The measurement is done on a two-dimensional object. In 2D, the Feret diameter is defined as the distance between two parallel lines touching the object on opposite sides. In case of 3D, the distance between two parallel planes is measured. The Ferret diameter changes depending on the angle at which it is measured.

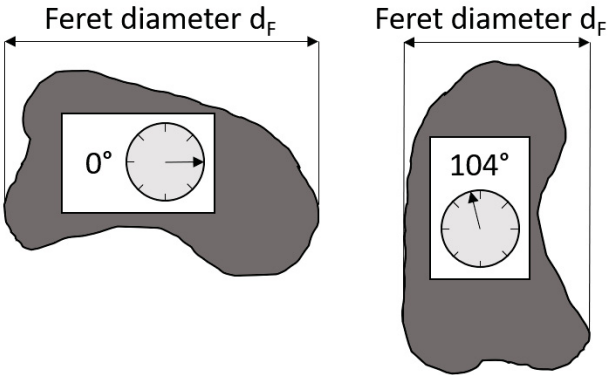

Figure 4: 2D representation of a measurement of the Feret diameter of an object rotated at different angles (namely 0° and 104°). The Feret diameter is defined as the distance between two parallel lines touching the object (without overlapping) on opposite sides of the object. The Feret diameter depends on the orientation of the object.

2.4 RAMAN

RAMAN spectroscopy is an analytical technique commonly used to identify inorganic phases [57] or to investigate phase transformations in ceramics such as $BaTiO_3$ [58,59]. Effects of

different grain size on the electrical properties of $BaTiO_3$ were investigated combining the use of XRD and RAMAN [60]. Also, the presence of graphite or organic materials can be proven via RAMAN performing measurements at the respective RAMAN shift [61–63].

RAMAN spectroscopy relies on inelastic light scattering by optical phonons, also termed RAMAN scattering [57]. According to Gardiner et al. [64], when a photon interacts with a molecule, it can be scattered in one of three ways. It can be elastically scattered and therefore retain its incident energy, which is called Rayleigh scattering. Or it can be inelastically scattered by giving (Stokes scattering) or removing (anti-Stokes scattering) energy from the molecule. According to quantum theory, the vibrational energy of a molecule is quantized. Non-linear molecules will have 3N-6 normal vibrations and linear molecules 3N-5, where N is the number of atoms in the molecule. The energy $E = h \cdot \nu$ of these vibrations is quantized as shown in Figure 5, where h is the Planck constant and ν the vibrational frequency.

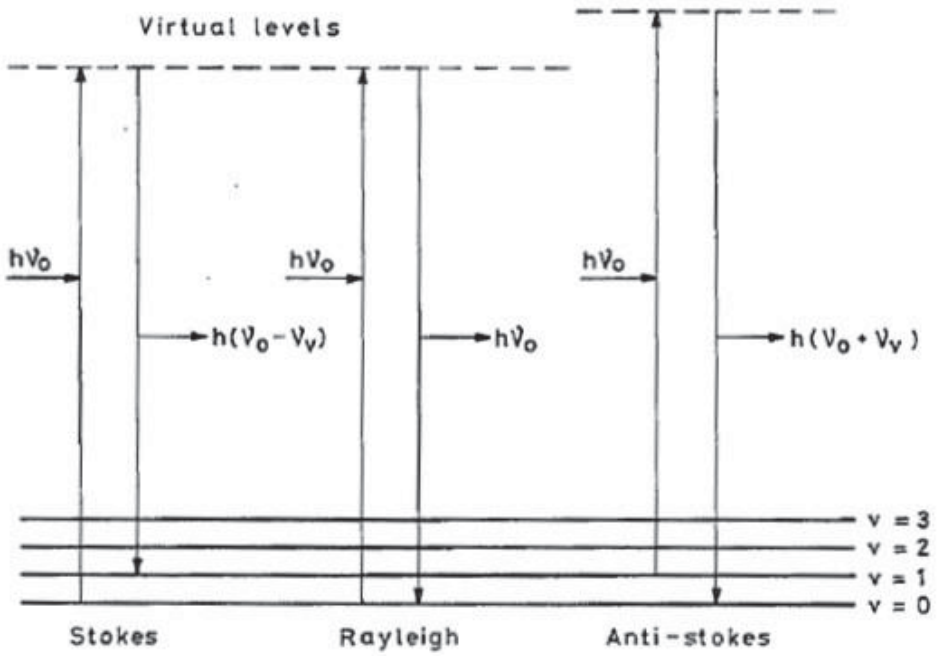

Figure 5: Idealised model of Rayleigh scattering and Stokes and anti-Stokes RAMAN scattering [64], where h is the Planck constant, ν the vibrational frequency and v is the vibrational quantum number of the energy of that particular vibration having values 0, 1, 2, 3, etc.

The Rayleigh scattering arises from transitions which start and finish at the same vibrational energy level. Stokes RAMAN scattering involves transitions which start at the ground state vibrational energy level v=0 and finish at a higher energy level, anti-Stokes RAMAN scattering involves transitions from higher to lower energy levels. An example of the complete Stokes and anti-Stokes RAMAN spectrum is shown in Figure 6.

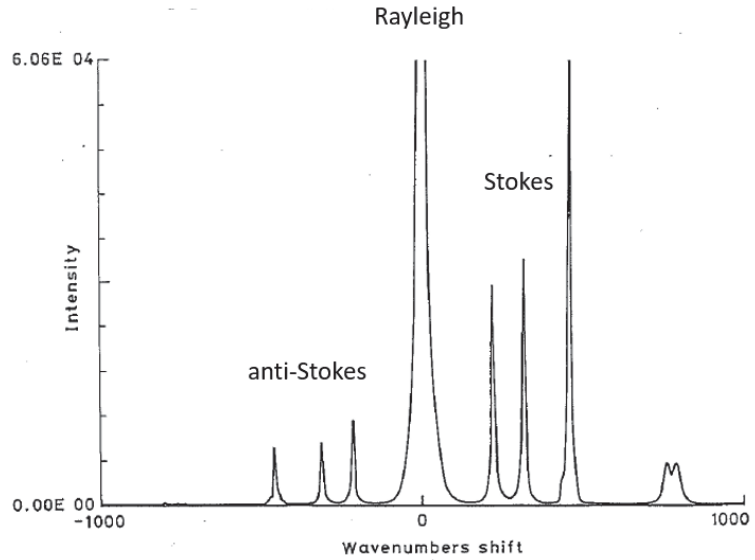

Figure 6: Stokes and anti-Stokes RAMAN spectrum of carbon tetrachloride [64](adapted).

RAMAN spectroscopy provides peaks that represent Raman-active molecular or crystal-lattice vibrations [57]. The peaks appear at specific wavenumbers (RAMAN shift, unit cm^{-1}). In Figure 7, a schematic RAMAN spectrum is shown with the corresponding information about the material.

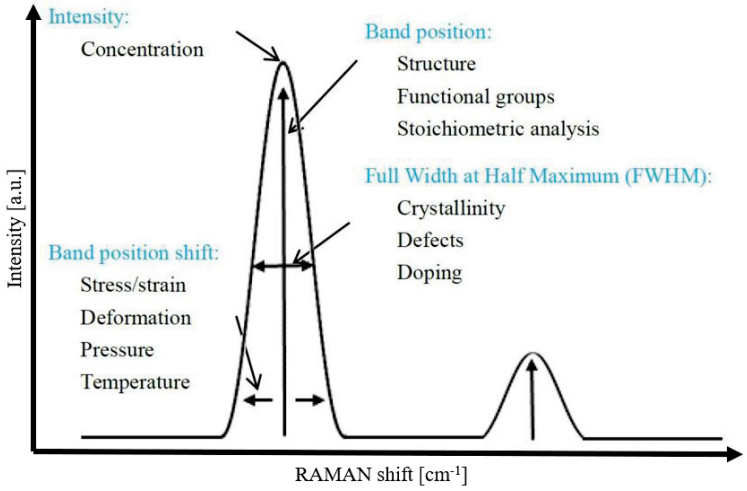

Figure 7: Schematic RAMAN spectrum with typical spectral signatures (commented in blue colour) and the corresponding material information (commented underneath in black colour). [65]

3 Methods

3.1 Processing of $BaTiO_3$ - powder

To produce porous $BaTiO_3$ samples, a $BaTiO_3$ powder was mixed with pore formers. The $BaTiO_3$ powder was obtained by solid state reaction, as described by Buscaglia et al. [14]. $BaCO_3$ and TiO_2 were mixed in stoichiometric proportions according to equation (1):

$$BaCO_3\,(s) + TiO_2\,(s) \rightarrow BaTiO_3\,(s) + CO_2\,(g) \qquad (1)$$

Ammonium polyacrylate was used as dispersant. Mixing was performed via wet ball milling, using zirconia media of varying sizes. The mixture was dried via freeze drying (laboratory freeze dryer Christ Alpha 1-2, Martin Christ Gefriertrocknungsanlagen GmbH, Osterode am Harz, Germany) and sieved (180µm mesh size, Retsch Italia Verder Scientific S.r.l., Torre Boldone (BG), Italy). It was calcined in air at 1100°C for 4 hours, with a plateau at 300°C for 4 hours needed for dispersant burn-out. The heating and cooling rates were 300°C/hour. For the heat treatment, a box furnace was used (Lindberg/MPH, Riverside, MI, USA). The powder was placed in a zirconia crucible.

3.2 Mixing with pore formers

The pore formers were powders of graphite and corn starch. The graphite powder was purchased by Timrex (Timrex KS5-44, Imerys Graphite & Carbon Ltd., Bodio, Switzerland). According to the data sheet, it has a highly anisometric particle shape with a particle size distribution of d_{10} = 10.8 µm, d_{50} = 27.0 µm, d_{90} = 53.0 µm. SEM images of the graphite particles are shown in Figure 8a. Its density was 2,25 g/cm³. The corn starch powder was purchased by Sigma-Aldrich (Sigma-Aldrich, S4126-2kg, lot., Sigma-Aldrich S.r.l., Milan, Italy). According to the data sheet, it has a particle size of less than 10 µm, the particle shape is globular. SEM images of the corn starch particles are shown in Figure 8b. Estimated qualitatively from the SEM image, the size of corn starch particles is about 10 to 20 µm. The density of corn starch was measured with a helium picnometer (Micromeritics AccuPyc 1330, Micromeritics Instrument Corp., Norcross, GA, USA). Before, it was put in oven (mechanical convection oven model SSTO-R, ATSfaar SPA, Milan, Italy) for 12 hours at a temperature of 70 °C. Also, its weight was measured before and after putting it in oven. That way, the weight loss was calculated.

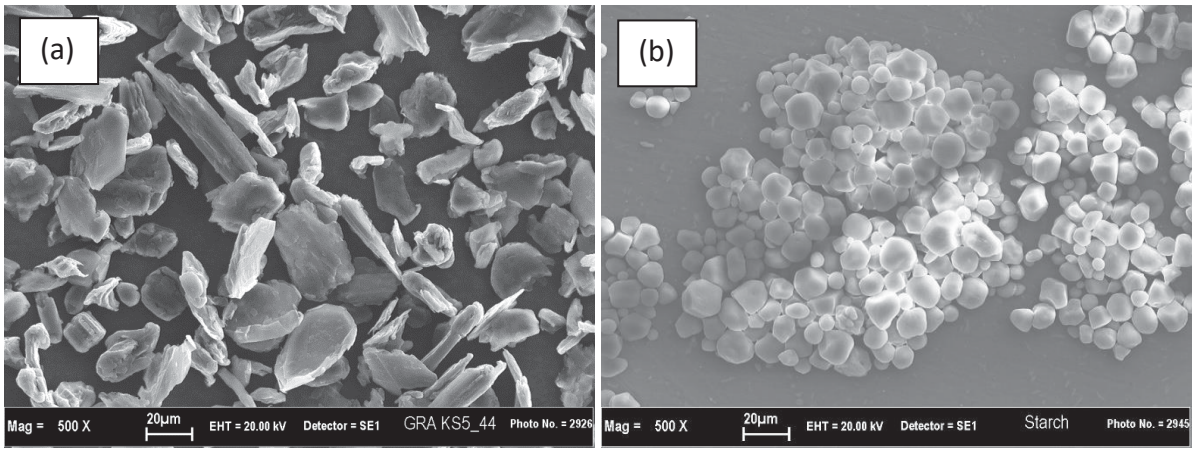

Figure 8: Secondary electron-SEM images of graphite(a) and corn starch(b) particles, used as pore formers.

The calcined $BaTiO_3$ powder was mixed with graphite and corn starch of varying compositions. Mixing was performed via wet ball milling using small zirconia milling media. In the case of graphite as pore former, the $BaTiO_3$ powder was mixed with graphite, a dispersant (Ammonium polyacrylate) and a binder (Resigel V/4, Saschim S.p.A., Lamberti S.p.A., Albizzate, Italy) in water. In the case of corn starch, the $BaTiO_3$ powder was mixed with corn starch and a dispersant (Ammonium polyacrylate) in ethanol. Parameters regarding mixing of the samples prepared in this work are summed up in Table 1. The sample names indicate processing parameters of the respective sample. The nomenclature consists in (1) the pore former ("G" for graphite, "C" for corn starch), (2) the amount of pore former (3 means 30 vol%, 5 means 50 vol%) and (3) the solvent (W for water, E for Ethanol). For samples processed with a binder, a B was added to the name.

Table 1: Parameters regarding mixing of the samples prepared in this work.

Sample name	Pore former (PF)	Solvent	Binder	Vol-% PF
G3W	Graphite	Water	No	30
G3WB	Graphite	Water	Yes	30
C3E	Corn starch	Ethanol	No	30
G5WB	Graphite	Water	Yes	50
C5E	Corn starch	Ethanol	No	50
GC3E	Graphite and Corn starch	Ethanol	No	30 (15 + 15)
G3E	Graphite	Ethanol	No	30

It is important to put as low mechanical stress as possible on the powder while mixing. Otherwise, the pore former particles can be damaged in the wet ball milling process. Damaging the pore former particles can lead to a change of the pore morphology in the resulting ceramic. A lower mechanical stress was achieved by only using zirconia balls with a small size (a diameter of 2mm), and by mixing at reduced rotation speed (about 90 rpm). The duration was 5 hours.

After wet ball milling, the mix was dried in oven (mechanical convection oven model SSTO-R, ATSfaar SPA, Milan, Italy) at 70°C for 24h. The dried powder was sieved (at a mesh size of 180

µm) to remove the zirconia balls and to avoid large agglomerates that could lead to irregular compaction in the pressing step.

3.3 Pressing & sintering

The sieved powder mix was filled into cylindrically shaped polymer moulds and pressed via cold isostatic pressing. The pressure was 1500 bar.

Finally, the green bodies were sintered in air at 1400°C for 4 hours. There were two additional plateaus at 400°C for 2 hours and 850°C for 2 hours to assure the complete burn out of the organic additives and pore formers. The heating and cooling rates were 180°C/hour. For sintering, the same furnace was used as for calcination of $BaTiO_3$. The sintering cycle is illustrated in Figure 9.

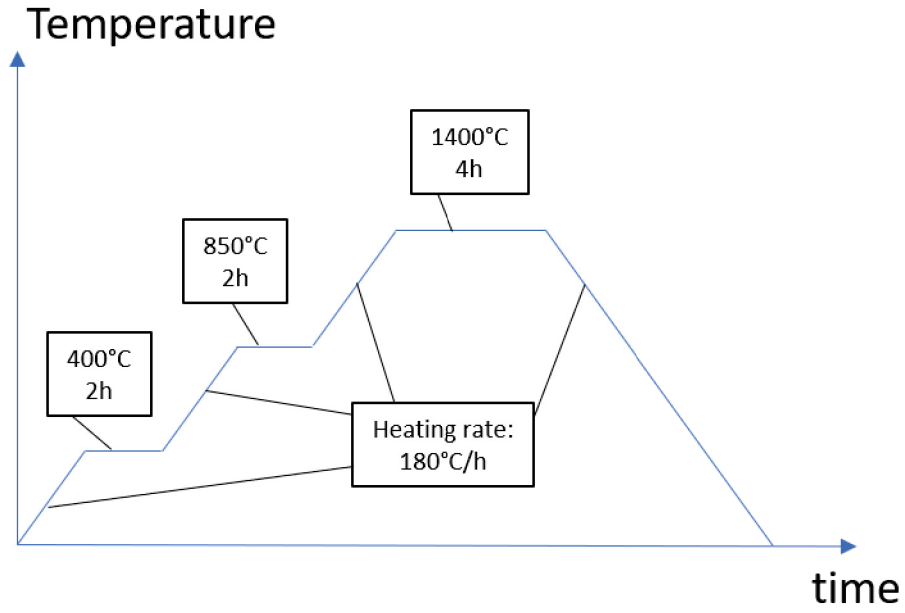

Figure 9: Temperature vs time - diagram of the sinter cycle of the samples produced in this work. The green bodies were sintered at 1400°C for 4 hours. Two additional plateaus at 400°C for 2 hours and 850°C for 2 hours assured the complete burn out of the organic additives and pore formers. The heating and cooling rates were 180°C/hour.

3.4 Density & porosity estimation via geometrical and Archimedes method

After sintering, the density of the sintered samples was measured. With, the theoretical density of $BaTiO_3$, a porosity was calculated. Two different techniques were used to measure the density of the samples. The height and diameter of the sample were measured, assuming an ideal cylindrical form, and a volume was calculated. Height and diameter were measured with a Vernier Calliper (Bocchi calliper, Pontiglio, Italy). A scheme of the measurements is shown in Figure 10. The mass was measured with an analytical balance (Gibertini E42S, Gibertini Elettronica S.R.L., Novate Milanese MI, Italy). From the values of mass and volume, the density was calculated. This technique is referred to as the geometrical method. Additionally, the mass of the sample was measured under water. The density was calculated with the Archimedes method.

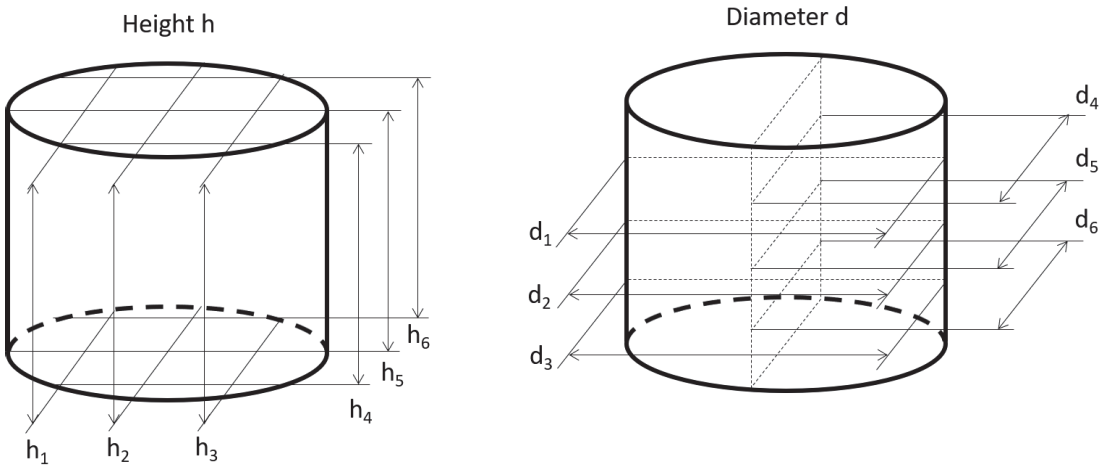

Figure 10: Scheme of the measurements of diameter and height of the samples. Mean values and standard deviation were calculated. The volume was calculated from the mean values of diameter and height, assuming an ideal cylindrical shape of the samples. A standard deviation of the volume was calculated via propagation of error.

3.5 Qualitative 2D characterization of the microstructure via SEM

The 2D microstructures of the samples were investigated with a SEM in secondary electron detector mode. Images were taken of the fractured surface and the polished surface of the samples. The fractured surface neither requires the sample to be cut nor polished. A green body is difficult to polish due to its structural instability. Therefore, the fractured surfaces of the green and the sintered samples were investigated with SEM and compared. To compare the microstructure of the sintered samples, SEM images were taken on the polished surface of the samples. The pore structure is easier to compare on a flat surface. The appearance of the pores is not distorted by the roughness of the surface as it would be on a fractured surface.

To attain the fractured surface of the samples, the samples were fractured with hammer and chisel. The fractured surface was coated with an Au-Pd film (Polaron SC7640 Sputter Coater, Quorum Technologies LTD, Lewes, United Kingdom) and images of the fracture surface were taken with a SEM (LEO 1450VP, Carl Zeiss S.p.A., Milano MI, Italy).

To attain a polished surface of the samples, the samples were (1) embedded in resin (ResinPRO, Resin Pro SRL, Arcola, Italy), (2) cut (precision sectioning saw IsoMet 1000, Buehler, Lake Bluff, Illinois, USA) and (3) polished (SiC-paper with roughness 2500 and 4000, grinder/polisher Planopol 2, Struers S.a.r.l., Arese (MI), Italy). Like the fractured surfaces, the polished surfaces were then coated, and images were taken with the SEM.

3.6 3D characterization via µ-XCT

To characterize the samples via µ-XCT, the samples were embedded in resin, then cut in slices (as done for the investigations with SEM). The slices were then cut with a target preparation device (Leica Target Surfacing System EM TXP, Leica Microsysteme Leica Mikrosysteme Handelsges.m.b.H, 1170 Wien) so that they were smaller than 1 mm in two axes. Then they were glued onto a glass rod and positioned in the µ-XCT chamber (X-ray Nanotom m research edition by General Electric). The µ-XCT is equipped with an X-ray tube with maximum voltage of 180 kV and a flat panel detector with a resolution of 3052 x 2400 pixel. Samples were scanned in 360 degrees, capturing 2000 radioscopic images on the flat panel detector. The

imaging time was 800 ms/frame. The acceleration voltage was 67 kV, the current 220 µA. Setting the measurements to high resolution generally leads to a low signal to noise ratio. Therefore, at each position, 7 images were taken and averaged to reduce noise. The scanning time was about 4 hours per sample. The reconstruction of the 3D volume was carried out on a proprietary software provided by General Electric. The output was a grey value-image with a voxel size of about 500 nm in x, y and z. The output is a greyscale with colour depth 16bit unsigned. The size of the data after reconstruction in 3D was 15.4 GB.

3.7 Image Analysis

3.7.1 Pre-processing and segmentation of the CT images

For pre-processing and segmentation, software application Avizo Version 2019.1 (Thermo Fisher Diagnostics Austria GmbH, Vienna, Austria) was used. To analyse the samples, for each sample a volume of interest (VOI) of roughly the same dimensions was cropped. Particular attention was put on artefacts attributed to backscattering of X-ray radiation that could not be entirely removed in the pre-processing step. Since the artefacts are primarily located in the centre of the scanned volume, a VOI outside the centre was cut out for every single sample. In Table 2, the exact voxel size and the size of a VOI is shown.

Table 2: Voxel size and size of the volume of interest for each sample.

Sample name	Voxel size $V_x = V_y = V_z$[µm]	VOI size [µm]
C3E	0.576783	290.70
C5E	0.581747	290.29
G3W	0.562401	290.76
G3WB	0.581303	290.65
G5WB	0.565114	290.47
G3E	0.583938	290.22
GC3E	0.581303	290.65

Several approaches were tried, combining different segmentation methods with filters for pre-processing. Filtering was necessary to reduce noise in the images. The filtering methods used in this work were the non-local-means filter, the median filter, opening and several edge preserving filters from Avizo. Images of pre-processing and segmentation are shown as flow chart in Figure 11. The segmentation methods were the automated threshold method (Otsu's method), the adaptive thresholding method (Otsu's method with an adaptive threshold) and the watershed segmentation method.

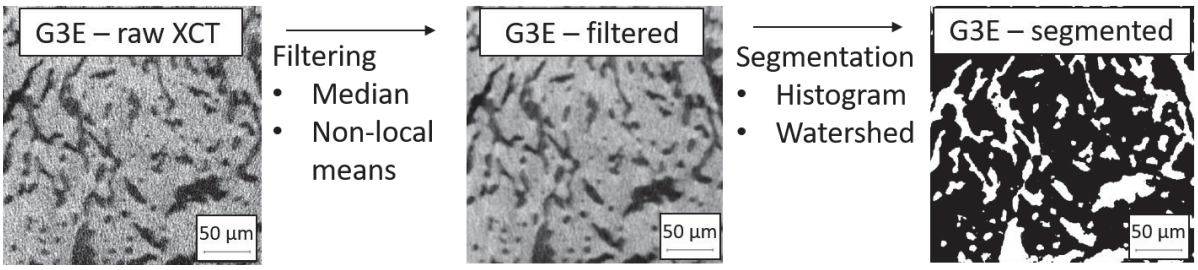

Figure 11: Workflow for pre-processing and segmentation, shown on sample G3E.

Filtering

For illustration purposes, images of sample G3E filtered with different methods are shown in Figure 12. The aim in filtering the sample is to enhance the signal to noise – ratio.

The median filter is reported to be very effective for reducing salt-and-pepper noise, i.e. sharp disturbances in the image [49]. For the samples analysed in this work, the median filter blurred the image. This led to an over-detection (or over-segmentation) of the pore phase, i.e. the pore volume increased with respect to the matrix volume. Like the median filter, the nonlocal means-filter is used for image denoising. In the present work, it filtered out most of the noise while preserving the edges between pores and matrix. Opening is used on binarized images to filter small elements in the binarized image. It is used after segmentation.

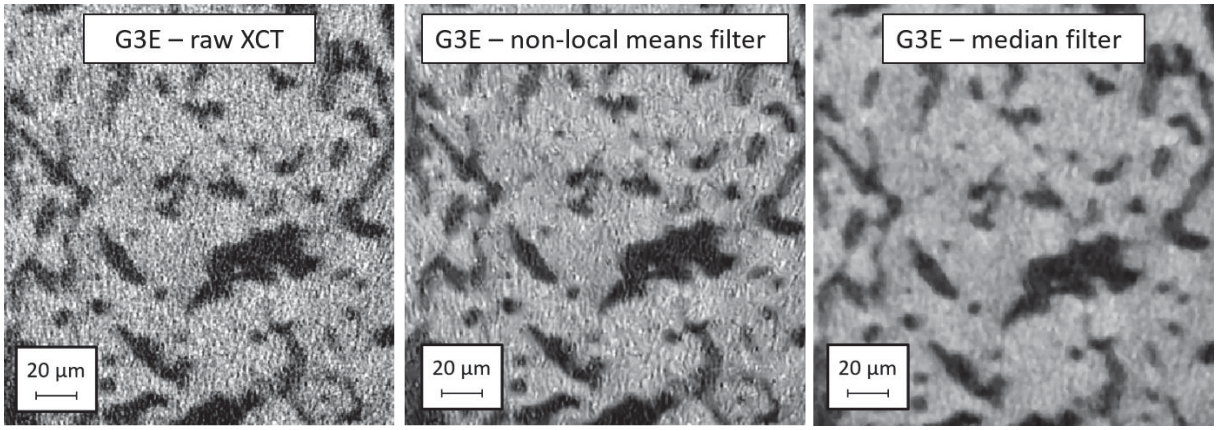

Figure 12: Images of µ-XCT-scan of G3E. The raw image is shown next to images filtered with the non-local means filter and the median filter.

Segmentation

The result of different segmenting techniques is shown in Figure 13. In the present work, the automated threshold method (i.e. Otsu's method) proved to be the best choice for segmenting the images. In the case of the adaptive thresholding technique, results depended strongly on the choice of the window for the local threshold. If the window was too big, results resembled the images the AUTO threshold technique. If the window was chosen too small, often noise was detected as porosity. The reason for this is assumed to be that if the window for choosing a local threshold was so small that not a single pore appeared in the window, the algorithm chose an arbitrary threshold for segmenting the image. Measuring samples with different pore structures, this would lead to instable results for segmentation. The gain of choosing the adaptive thresholding technique was not significant. Like the adaptive thresholding method, also the watershed module proved to be very sensitive to input parameters set by the user.

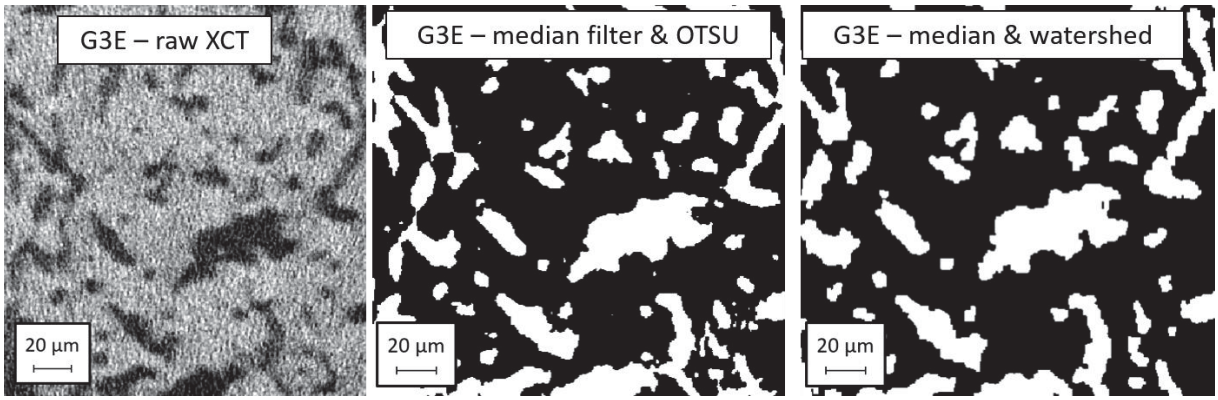

Figure 13: Sample G3E, filtered with median filter and segmented with OTSU's method and the watershed method.

Final procedure of pre-processing and segmentation

To find a final preprocessing and segmentation procedure, segmented images of the samples as shown in Figure 13 are compared to the original images. An algorithm must be found so that the results resemble images segmented manually. Also, the same procedure should be chosen for all samples so that the results can be compared. The process of finding a suitable preprocessing and segmentation algorithm was not straight forward. There are innumerable possible changes in parameters and combinations of different filtering and segmentation algorithms for the samples. Parameters that were suitable for sample A, often did not work (i.e. led to over-segmentation) with sample B and vice versa. A flow chart describing the final segmentation algorithm is shown in Figure 14. It consists in a nonlocal means filter, used in Avizo (with the module Non-local means filter) with settings for Interpretation in 3D (which means input will be interpreted as a 3D volume), spatial standard deviation on 5 (controls how the similarity between voxels decreases with distance – the higher the value, the blurrier the image), intensity standard deviation of 0.2, Search window size 10 (represents a radius of the search window in number of voxels) and local neighborhood 3. Then a histogram alignment was performed in x, y and z directions. The segmentation was done via AUTO threshold (with settings AUTO threshold low, mode 3D) with factorization criterion (which is based on Otsu's method). After segmentation, an opening of the binarized image was applied to get rid of small objects in the image that are supposed to be artefacts.

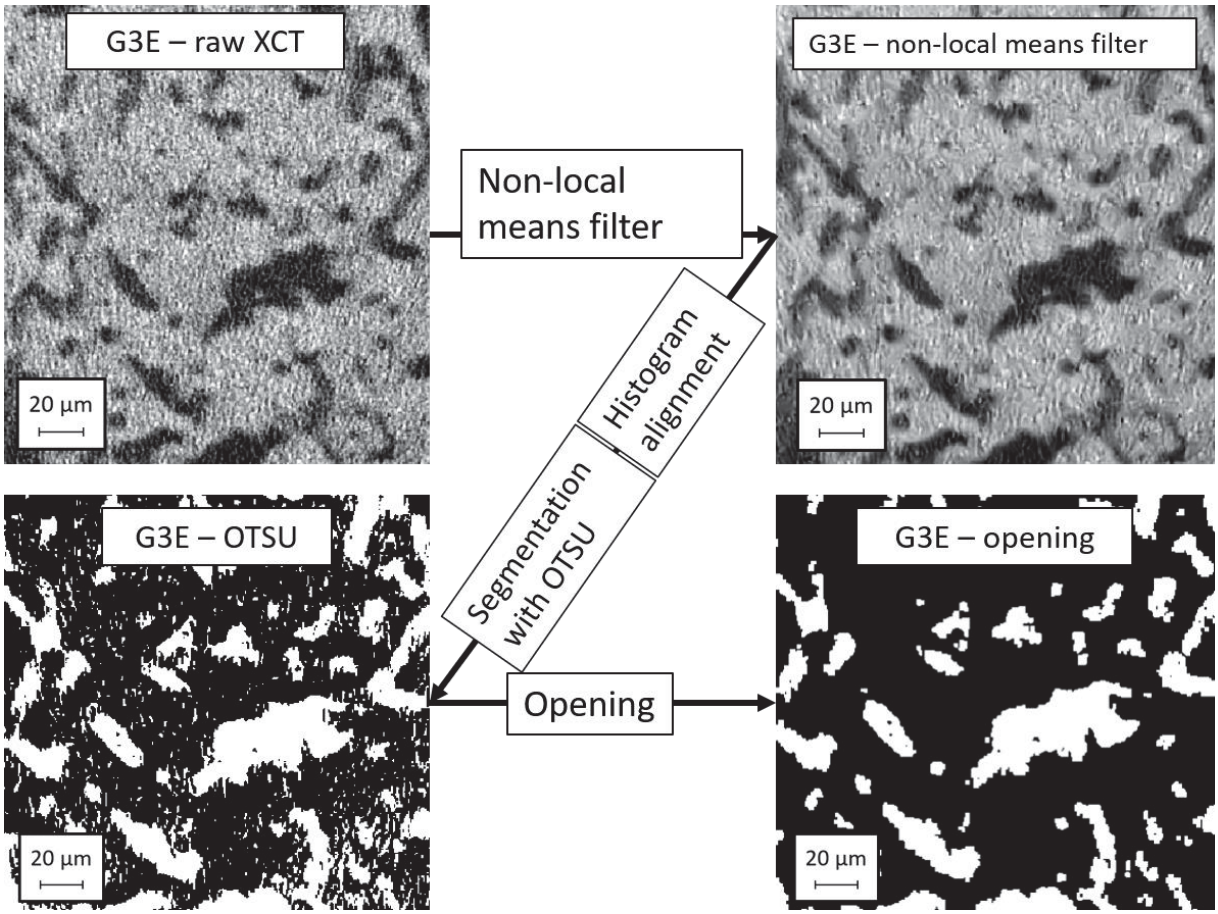

Figure 14: Final segmentation algorithm, shown on sample G3E.

3.7.2 Validation of pre-processing and segmentation by comparison of CT images to SEM images

For comparison, original µ-XCT-images, segmented images and the respective SEM images of the samples investigated in this work are shown in Figure 15.

For C3E (Figure 15a), pore structure as depicted in the µ-XCT and SEM are similar. Comparing the original CT image and the SEM image, the signal to noise ratio of the SEM image is notably better. This can lead to a loss of information regarding the pore structure. Smaller pores may be mistaken for noise and therefore unintentionally filtered out. In the case of C3E, the pore structure appears to be conserved well in the segmented CT image. Like in C3E, the pore structure of C5E (Figure 15b) appears to be reproduced well by the automated segmentation.

In the case of G3W (Figure 15c), in the SEM image, many thin elongated pores can be seen. By eye, this type of porosity is also visible in the original µ-XCT image. In the segmented sample, often the elongated pores are connected. The thin pores in the image were over-segmented which means that the pore volume is over-detected by the segmentation algorithm. Changing the threshold for the segmentation, pores in other areas were under-segmented. Apparently, for G3W, the contrast is not good enough to enable segmentation of the pore network without losing information. Qualitative investigations of the SEM images of G3W (see section “Microstructure investigations on SEM”) showed that there are two different types of porosity one deriving from the pore former, the other being intergranular porosity. The intergranular

porosity consists in smaller pores (about 1 to 3 µm). The signal-to-noise ratio did not enable to distinguish this type of porosity from noise in the µ-XCT. However, the intergranular porosity in the matrix material can lead to changes in density and consequently in contrast of the µ-XCT image. For the sake of comparability of the samples, the same procedure for segmentation was used for G3W.

Looking at the SEM image, G3WB (Figure 15d) has a more uniform pore structure compared to G3W. The resulting µ-XCT image and the segmentation appear accurate. This also counts for G5WB (Figure 15e), G3E (Figure 15f) and GC3E (Figure 15g). For G3E, that like G3W contained intergranular porosity, the pores seen in the CT images appear to be segmented accurately. However, the intergranular porosity cannot be seen in the segmented image.

In Figure 16, 3D representations of the segmented samples are shown in blue color. For each sample, the segmented $BaTiO_3$ – matrix (i.e. transparent pore structure) and the segmented pore structure (i.e. transparent $BaTiO_3$ – matrix) is shown.

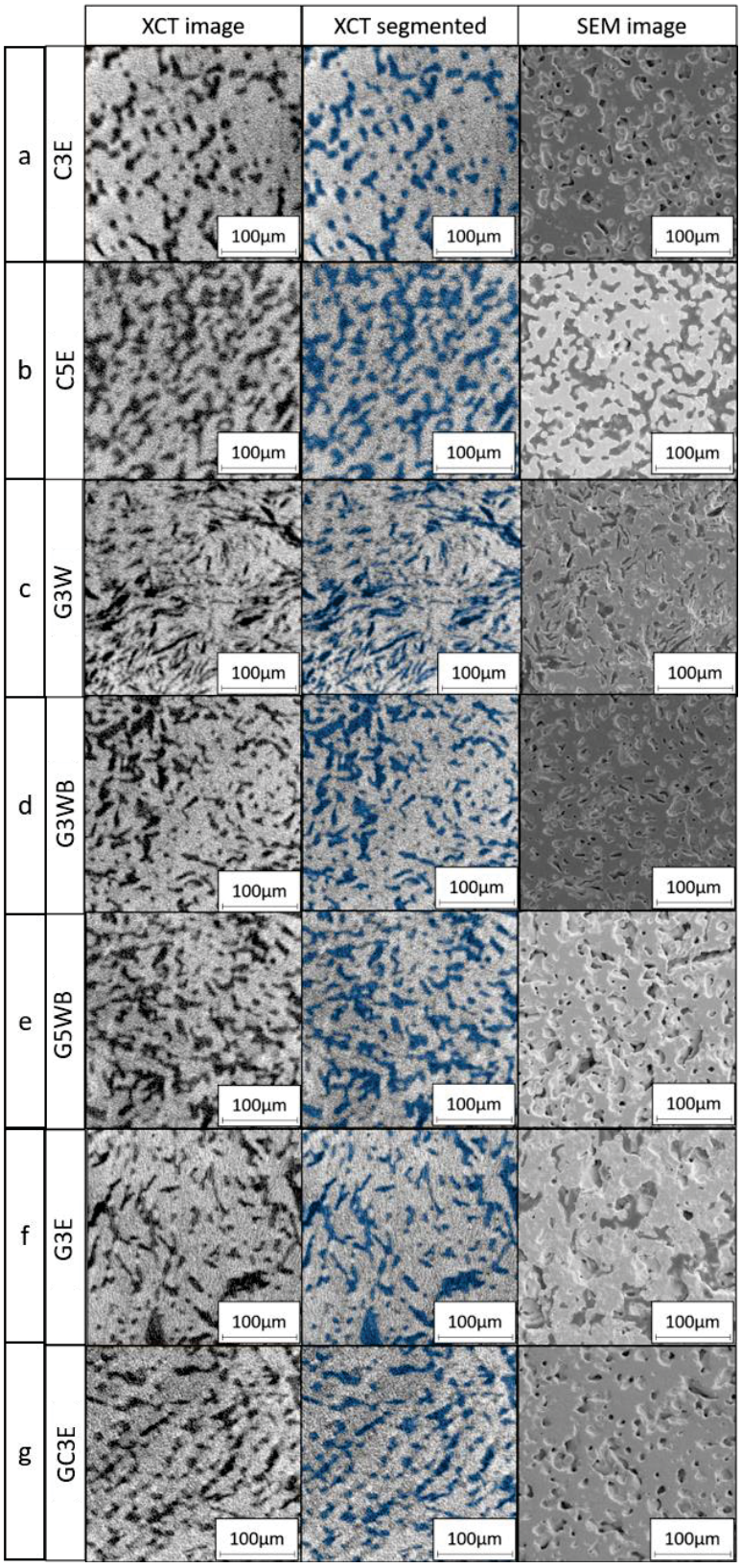

Figure 15: Original µ-XCT-image, segmented image and the respective SEM image of the samples C3E (a), C5E (b), G3W (c), G3WB (d), G5WB (e), G3E (f) and GC3E (g).

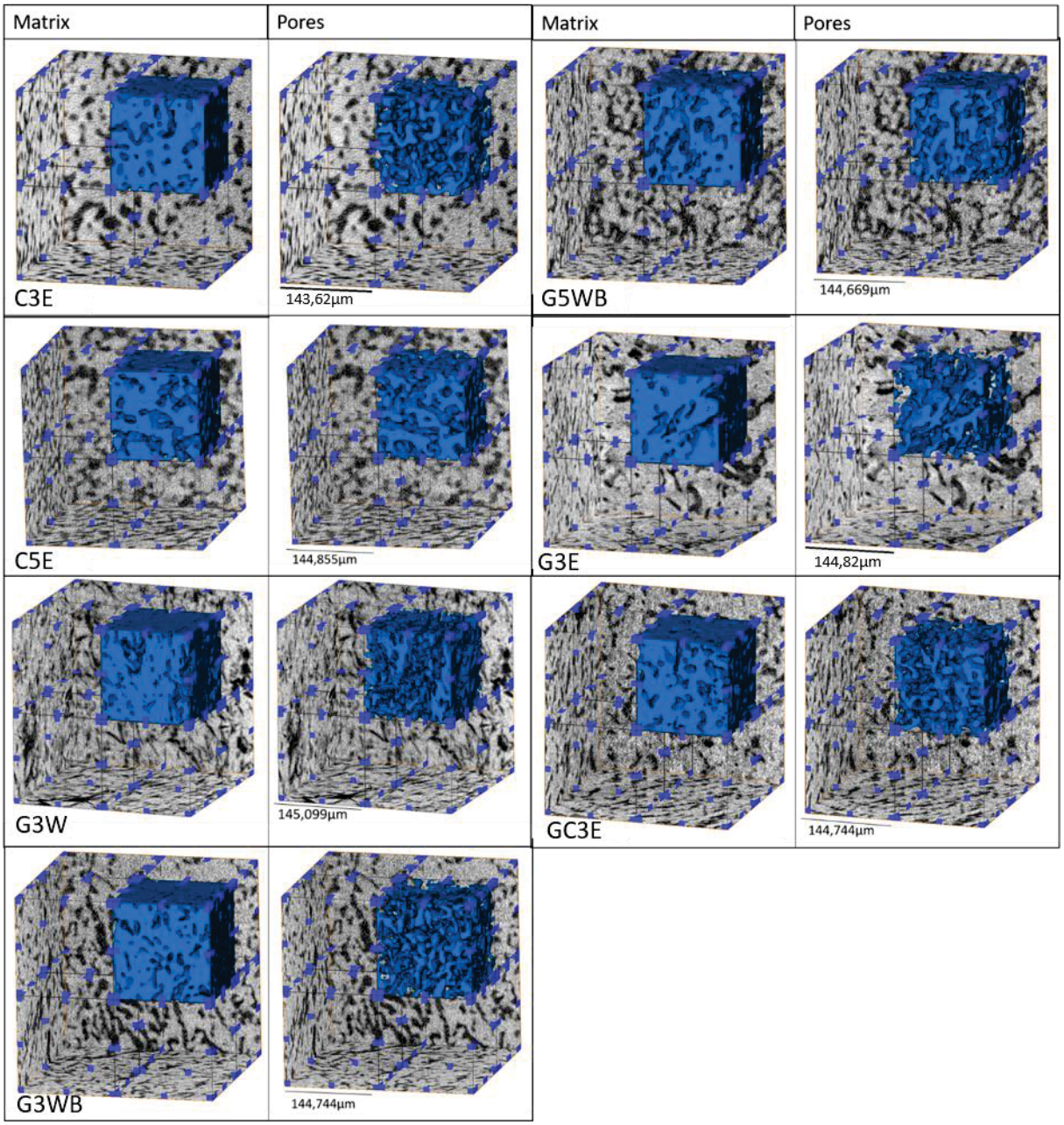

Figure 16: 3D representations of matrix and pore structure of the samples C3E, C5E, G3W, G3WB, G5WB, G3E and GC3E.

3.7.3 3D porosity from µ-XCT

As done for pre-processing and segmentation, software application Avizo (Thermo Fisher Diagnostics Austria GmbH, Vienna, Austria) was also used to calculate the porosity from µ-XCT measurements. To make a statistical evaluation, the segmented VOI was subdivided into eight sub-volumes. The porosity was calculated for each sub-volume. A mean value and a standard deviation of the porosity were calculated.

The porosity was determined by calculating the fraction of the volume of the pore phase and the total volume ($BaTiO_3$ and pore). The volume of $BaTiO_3$ and pore phase is the sum of the respective voxels multiplied by the volume of a voxel.

3.7.4 3D pore structure analysis via topological skeletons

To produce porous samples, $BaTiO_3$ powder was mixed with high amounts of pore former powders (up to 50 vol%). Therefore, a porosity between 20% and 50% is expected. To examine the pore structure and to gain further understanding about the distribution of the pores inside the sample, it is helpful visualize the segmented pore structure either in 2D (e.g. cross-sections) or in 3D (e.g. 3D-representations of the pore structure). As shown in Figure 17, with higher porosity, the pore structure becomes less transparent. In images (either cross sections or projections of the 3D representations), pores cover the sight over pore structures lying beneath. As a result, it is difficult to have an adequate impression of the pore structure. To attain further understanding, one can thin the structure until a skeleton remains. This illustration of the structure enables better visibility and allows conclusions about the distribution of the pores.

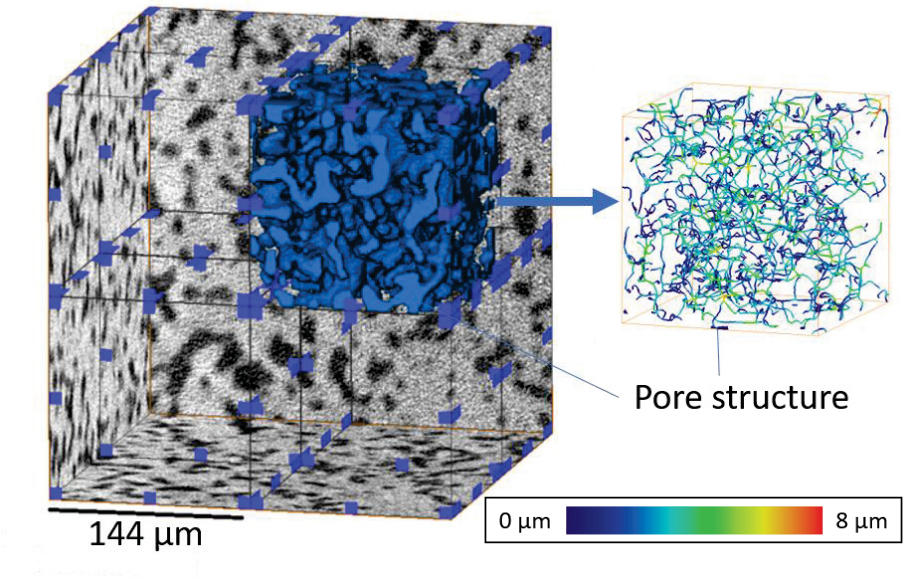

Figure 17:3D-rendering of VOI before and after skeletonization of the pore structure, shown on sample C3E. Before skeletonization, the pore structure is non-transparent, i.e. it is not possible to see pores beneath the surface of the VOI. Skeletonization enhances the visibility of the pores inside the VOI. The colour of the skeleton indicates the radius of the pore. On the bottom of the figure, a heatmap is shown indicating the approximate value of the radius.

Skeletonization was done in Avizo with the module “Auto Skeleton”. The Auto Skeleton module includes thinning of the pore network and the calculation of the radius of the pore channel. Information regarding the skeletonization algorithm can be found in the “Avizo User’s guide” [47].

The resulting skeletonized pore networks of the samples are visually compared regarding:

- The pore distribution. Comparing the skeletons, one can qualitatively compare the distribution of the pores regarding density (i.e. the number of pores per volume) and homogeneity.
- The radius of the pore channels. The radius is indicated by the colour of the lines. An impression can be gained if a sample has pores of higher or lower radius. Also, spatial variations in pore radius can be compared. According to the documentation in Avizo,

the radius of the skeleton at a given point is the distance to the closest voxel assigned to the non-pore phase.

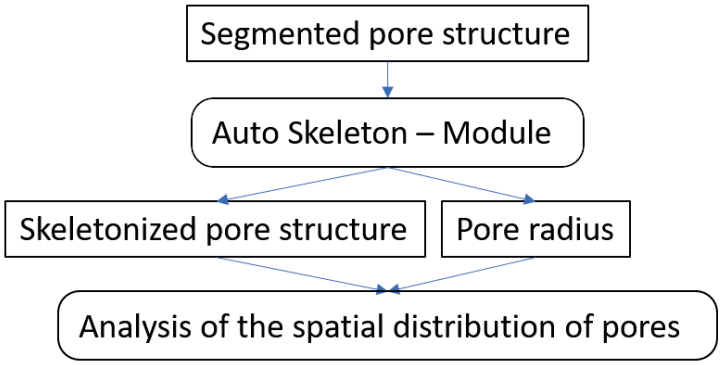

Figure 18: The aim of the procedure in this section (3.7.4) is to get a more transparent 3D – structure. This way a better understanding about the distribution of the pore structure can be attained. Consequently, the pore network can be analysed regarding the spatial distribution of the pores, e.g. homogeneity, density of pores etc.

3.7.5 Validation of the Skeletonization process

In Figure 19, the skeletonized pore network of the samples investigated in this work is shown. The pore structure is represented by colored lines. The color indicates the radius of the pore channel. For orientation purposes, a coordinate system is shown on the bottom of Figure 19. The heat map indicates an approximate value of the radius of the pore channels. It is shown on the bottom of Figure 19.

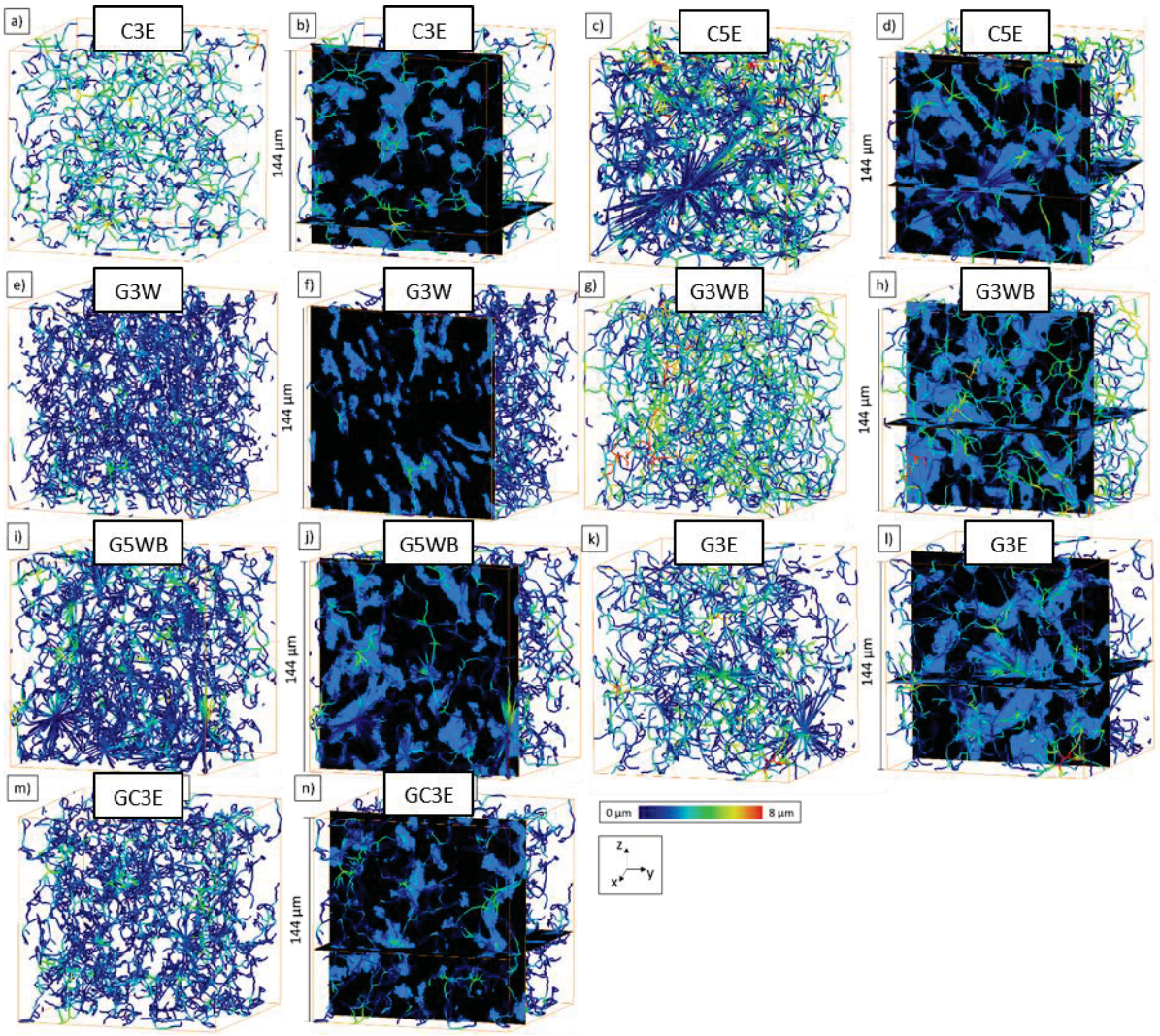

Figure 19: Skeletonized pore structures of the samples analysed in this work. To validate the skeletonization of the pore networks, the skeleton of each single sample was compared to the cross section of the sample.

To validate the skeletonization of the samples, skeletons are visually compared to a cross section of the original pore structure. A skeletonized sub-volume and the cross section of C3E are shown in Figure 19a and b. From visual appearance, the skeleton is an accurate representation of the original structure. The number of thinned lines and the spacing between the lines resemble the original pore network.

In Figure 19c and d, the skeleton and the cross section of C5E are shown. For C5E, the number of lines in the skeleton appears higher than the number of pore channels in the cross section. The color of the lines indicates that there are many thin pore channels. This is not in agreement with observations of the cross section. It appears that in the process of skeletonization the pores or pore channels were split into several lines. This led to the formation of artifacts consisting in several thin (indicated by color) linear lines connected by a single nod. Due to their shape, these artifacts are referred to as starring artifacts (i.e. in the form of a star). In the Avizo user guide, these artifacts are referred to as “star-shaped sets of connected segments in the spatial graph” [47]. According to the user guide, it may be the sign of too much noise in the data.

In G3W, the visual appearance of the skeleton and the cross section of the sample are similar (see Figure 19e and f). The pore network of G3W consists in thin elongated pores. For G3WB (Figure 19g and h) the skeletonization worked accurately. The skeleton shows pore channels with varying radius. G5WB (Figure 19i and j) and G3E both have several starring artifacts, like C5E. In both cases, the density of pores in the respective skeletons appears higher than what is suggested by the cross sections. For GC3E, the skeletonization appears accurate. No starring artifacts can be seen. The pore structure consists in thin pores, the pore radius appears uniform.

Table 3: Summary of the Validation of the skeletons

Sample name	Pore former	Solvent	Binder	Vol-% pore former	Validation of Skeletonization
C3E	Corn starch	Ethanol	No	30	OK
C5E	Corn starch	Ethanol	No	50	Starring artefacts
G3W	Graphite	Water	No	30	OK
G3WB	Graphite	Water	Yes	30	OK
G5WB	Graphite	Water	Yes	50	Starring artefacts
G3E	Graphite	Ethanol	No	30	Starring artefacts
GC3E	Graphite and Corn starch	Ethanol	No	30 (15 + 15)	OK

3.7.6 µ-XCT - separating pores via watershed algorithm

To produce samples with a distinct pore structure, pore former particles were added to the powder before the pressing step. The idea is that the resulting pore structure inherits the morphology of the pore former particles. Therefore, making a particle analysis (e.g. analysis of the particle size distribution) on the resulting pores (i.e. the voids left by the pore former particles in the sintering step) can be a valid approach to analyze the pore structure. Resulting parameters can be directly compared to the pore former particles.

The pores in all samples formed a highly interconnected pore structure (see Figure 20). The pore structure must be separated to make a particle analysis on the pores. The separation was done with the “separate objects” – module on Avizo. According to the Avizo manual [47], the module is based on a watershed algorithm (Chamfer conservative). The accuracy of the “separate objects” – module was validated by visual comparison of the pore structure before and after application of the “separate objects” – module (i.e. comparison of cross sections and 3D representations of the VOI).

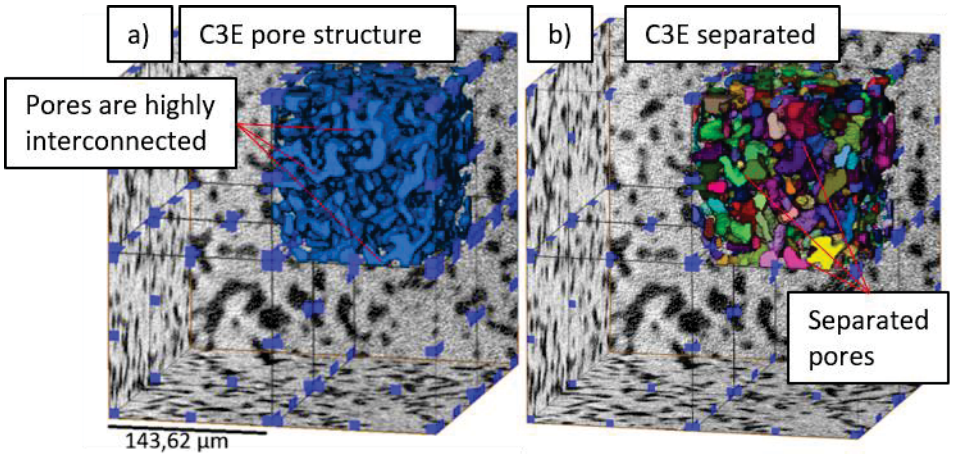

Figure 20: The segmented pore structure is shown in blue colour (a). It is highly interconnected. The pores separated via watershed algorithm are shown in (b). For illustration purposes, pores in (b) are shown in different colour (256-bit colour depth). Shown on sample C3E.

After separating the pores, the pore structure was analyzed regarding size and shape:

- To attain the pore size distribution, the Feret diameter was measured and the distribution of the diameter was determined. The distribution was then compared to the pore former particles.
- Pore volume and pore surface area were measured. Like the Feret diameter, these values are an indicator about the pore size distribution in a sample. The relationship between surface area and volume of the pore structure indicates the pore shape.

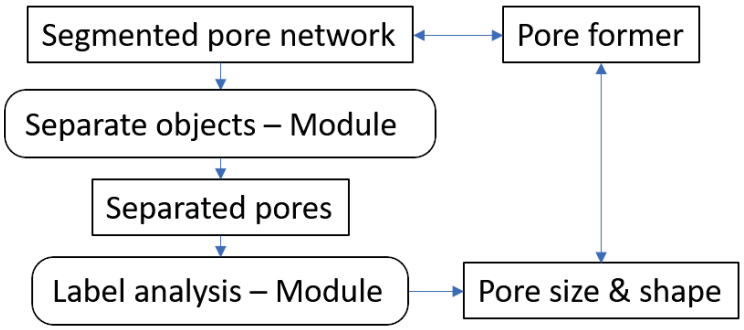

Figure 21: The aim of the procedure in this section (3.7.6) is to attain pore parameters that can be compared to the pore former.

3.7.7 Validating the separation of pores via watershed algorithm

Validation of the watershed method is done by visual comparison of the samples before and after applying the algorithm. Two approaches were tried to visualize the samples, one approach was looking at cross sections of the samples. The other is to compare 3D representations of the pore structures. For demonstration purposes, both validation approaches are shown for samples C3E and G3E in Figure 22. In the cross sections, the $BaTiO_3$-substrate is shown in black color. The pores are shown in white color for the samples before separating and labeling. After the separation, the pores are labeled by color. This way, it is possible to distinguish different pores by eye. Comparing the cross sections, it appears that several pores are cut arbitrarily, i.e. in the 2D representation of the binary image we don't see any differentiation of the pore (see Figure 22, "G3E separated"). However, looking at 3D

representations of the pore structure, the separation of the network is easier to comprehend (see Figure 22, bottom row).

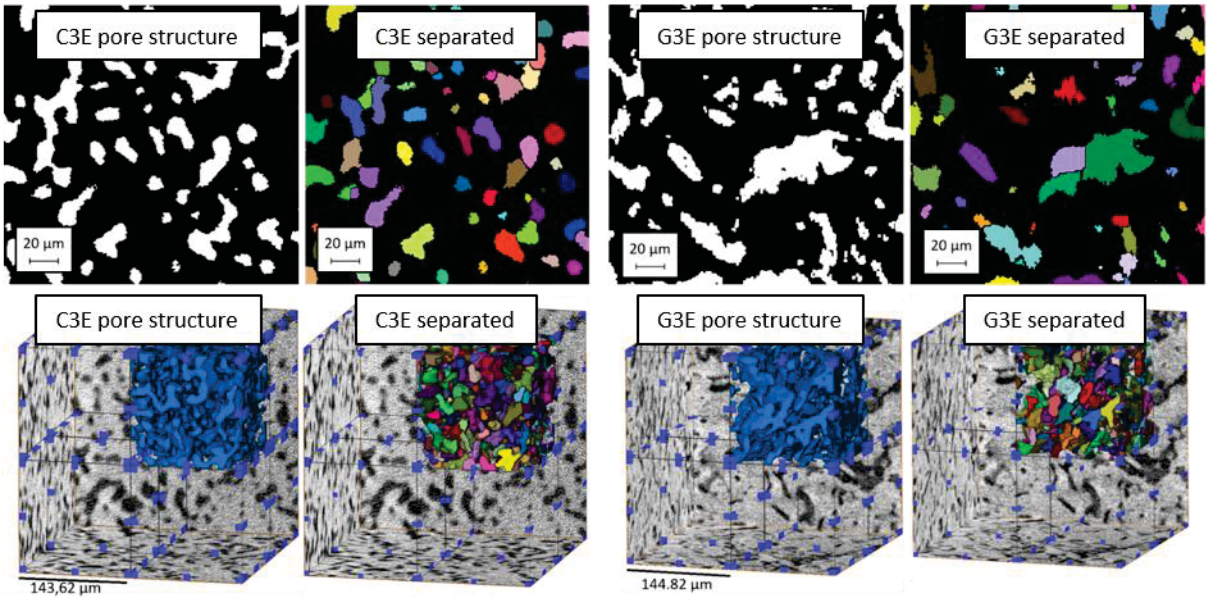

Figure 22: Validating the separation and labelling algorithm for samples C3E and G3E. To validate the samples, cross sections and 3D representations of the samples are compared before and after separating and labelling. For illustration purposes, after separation, pores are shown in different colour (256-bit colour depth). In the cross sections, $BaTiO_3$ is shown in black, the pores in white. The separated pores are shown in varying colours to visually distinguish one pore from another. In the three-dimensional representation, the pores are shown in blue colour before and in different colours after separation and labelling.

In Figure 23, 3D representations are shown for the samples investigated in this work. From visual impression, the “separate objects” – algorithm and the labelling of the pores worked accurately on the pore networks.

Due to the high interconnectivity of the pore structure, often the pore necks are relatively large with respect to the pore sizes (see e.g. Figure 22, “G3E separated”). Separating the pores therefore results in a distorted form, i.e. sharp edges, flat surfaces.

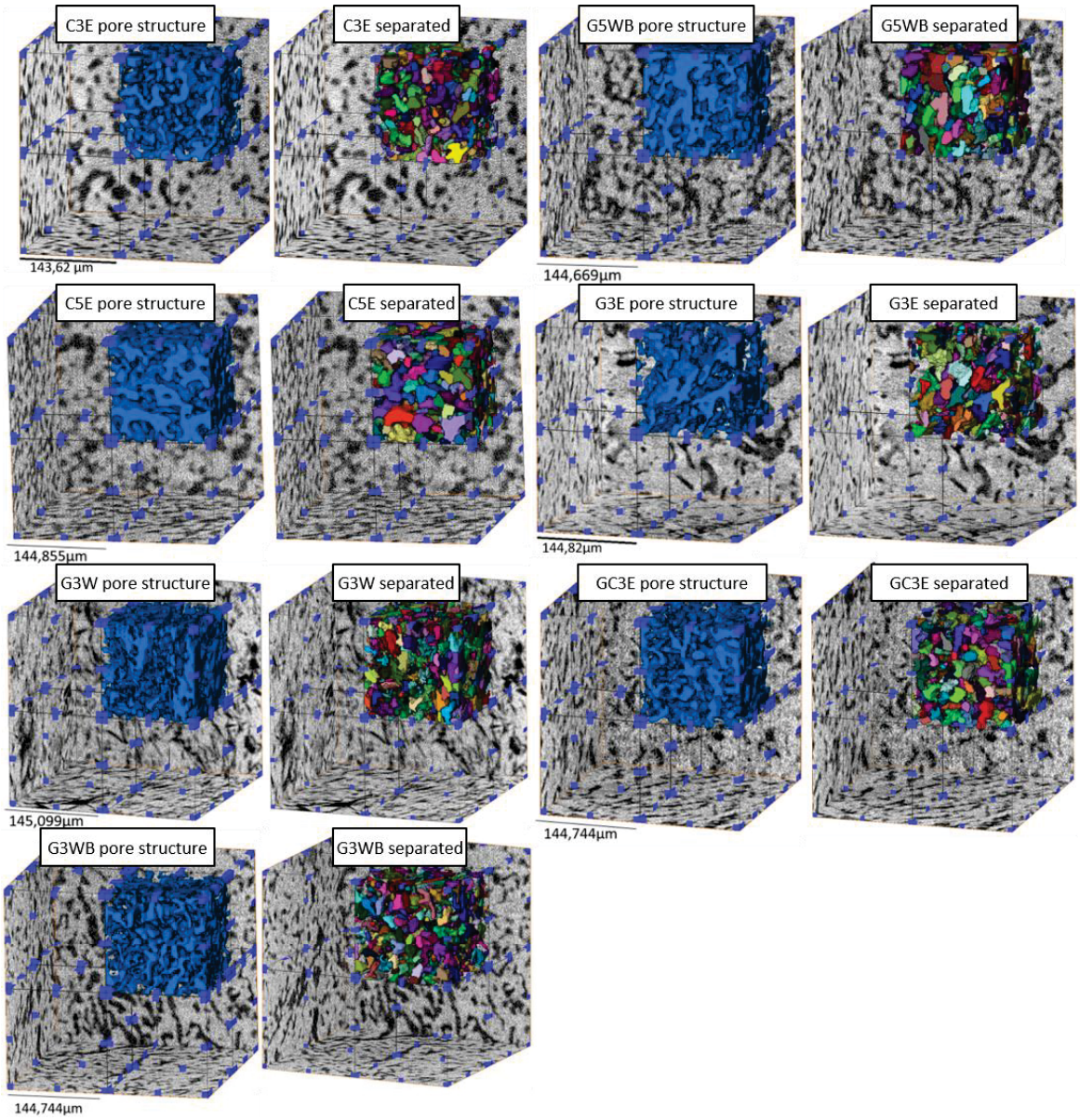

Figure 23: Validation of the "separate objects via watershed" algorithm. VOIs of the samples investigated in this work are shown before and after applying the separate objects module. For illustration purposes, after separation, pores are shown in different colour (256-bit colour depth). From visual impression, the algorithm separated the pores well.

3.7.8 3D analysis of pores separated via watershed algorithm – Illustration of the pore diameter

Particle-size analysis is a measurement of the size distribution of individual particles in a soil or a powder sample[66]. The size of a particle can be measured with several different methods and instrumentations. Depending on the instrumentation, different ranges of particle sizes are covered. In the present work, the size of the pores left by the pore formers is to be measured. The pore size is represented by the maximum Feret diameter $\delta_{F,max}$ in this section. The pore formers have a particle size range of about 10 µm to 30 µm.

The distribution of $\delta_{F,max}$ can be presented as:

- Sum distribution Q_r: It displays the percentage of the pores beneath a given $\delta_{F,max}$. An example of a sum distribution is shown in Figure 24c and d.

- Density distribution q_r: It shows the number (or the percentage) of pores ΔQ_r in a range of $\delta_{F,max}$ between $\delta_{F,max,u}$ and $\delta_{F,max,o}$:

$$q_r(\delta_{F,max,u}, \delta_{F,max,o}) = \frac{\Delta Q_r}{\delta_{F,max,o} - \delta_{F,max,u}} = \frac{\Delta Q_r}{\Delta\delta_{F,max}} \quad (2)$$

  As you decrease the range $\Delta\delta_{F,max} = \delta_{F,max,o} - \delta_{F,max,u}$, q_r becomes:

$$q_r(\delta_{F,max}) = \frac{\Delta Q_r}{\Delta\delta_{F,max}} = \frac{dQ_r(\delta_{F,max})}{d\delta_{F,max}} \quad (3)$$

Index r indicates the weight of the particles in the measurement. In Q_0 and q_0, the particles are counted, where every particle has the same weight. In this case, it is denominated as Histogram analysis (Figure 24a and b). In Q_3, each particle is weighted by its volume, in analogy to the sieving analysis, where the mass of the particles is measured. This means that Q_3 shows the volume percentage of pores beneath a given $\delta_{F,max}$. Examples of Q_3 and q_3 are shown in Figure 24c to f.

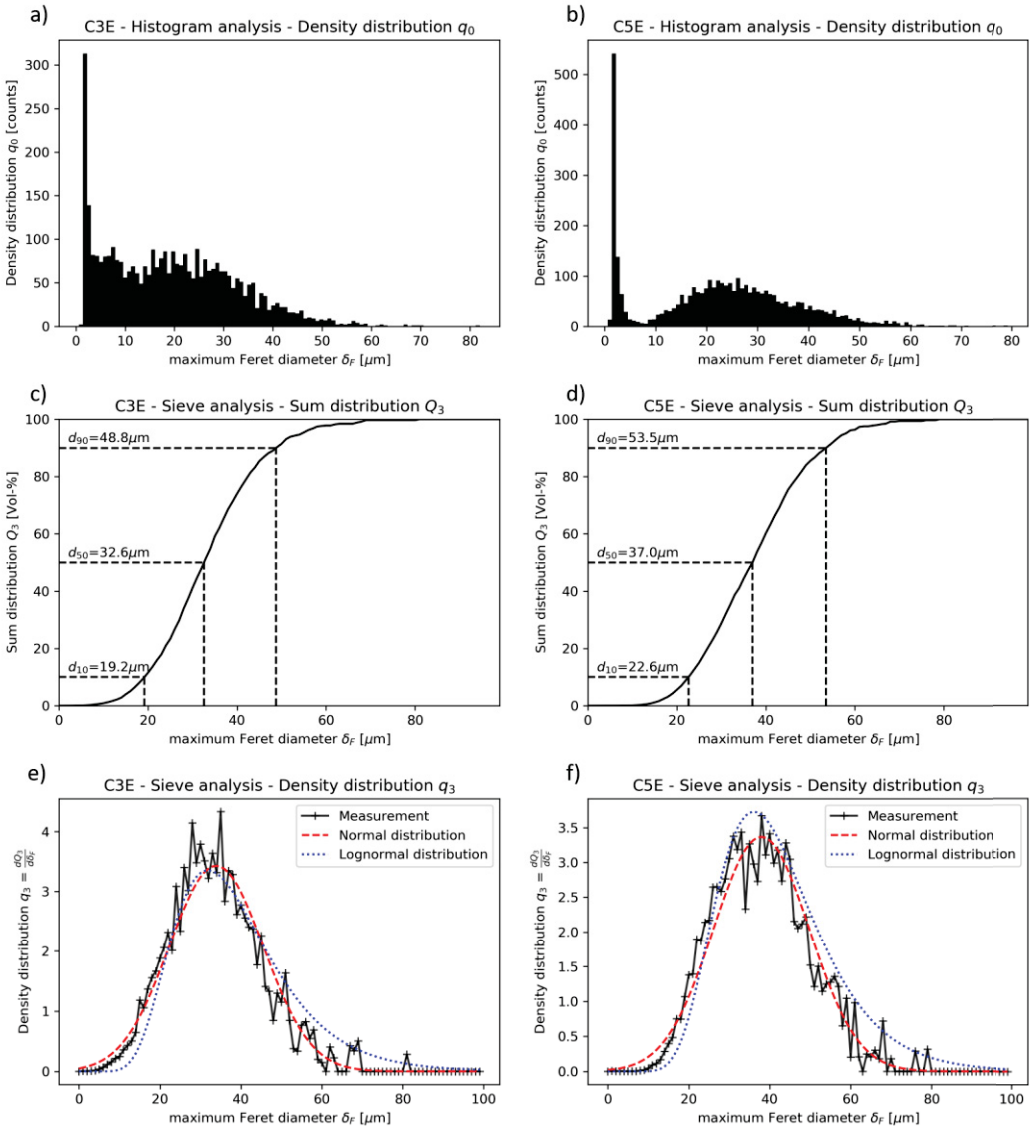

Figure 24: Particle size analysis via histogram analysis (density distribution q_0, (a) and (b)) and sieving analysis (sum distribution Q3, (c) and (d), and density distribution q_3, (e) and (f)) for samples C3E (a, c and e) and C5E (b, d and f). In q_0, there is a peak suggesting that most of the pores have a $\delta_{F,max}$ less than 5 µm. This is not in agreement with observations of cross sections of the samples or 3D representations. Looking at cross sections, most of the pores have a diameter between 10 and 50 µm. A second peak at higher pore diameter between (15 and 25µm) is visible, but not very pronounced. In the case of sample C3E(c), it is barely visible. Looking at q_3, the peak at small diameters is not present. Peaks at a higher diameter are well visible. This makes it possible to evaluate the pore diameter of the samples.

3.7.9 3D analysis of pores separated via watershed algorithm – Validation of the diameter distributions q_0, Q_3 and q_3

In Figure 24a and b, q_0 has a dominant peak at low diameters, suggesting that most of the pores have a pore size less than 5 µm. This is not in agreement with observations of the 3D representations (see Figure 22 or Figure 23) or the cross sections (Figure 22) of the samples. Looking at cross sections, the diameter of most pores is estimated between 10 and 50 µm. In q_0, a second peak at higher pore diameter between (15 and 25µm) is visible. The peak is not very pronounced compared to the peak at δ_F smaller than 5µm. In the case of sample C3E, it is barely visible. Looking at q_3, the peak at diameter less than 5µm is not present. Peaks at a higher diameter are well visible. Generally, the distribution q_3 is unimodal. In several samples

such as G3WB and G5WB, the peak is broader. Also, it is to be noted that for all samples, q_3 contains a considerable amount of noise.

Parameter d_x is a relevant parameter of sum distribution Q_3, where x percent of the total pore volume has a maximum Feret diameter δ_F less than d_x. For the pore former graphite, values d_{10}, d_{50} and d_{90} are given by the supplier. Therefore, the same values for all samples are shown in Table 4.

In the pore size distribution q_3, the particle size distribution is approximated with a normal (i.e. Gaussian) and lognormal distribution. For comparison, curves of normal distribution and lognormal distributions are plotted over q_3 (see Figure 25). From visual comparison, the peak appears more accurate in the lognormal curve. Statistical evaluations for both distributions are shown in Table 4. Comparing d_{50} to the mean value calculated assuming a normal and a lognormal distribution, the mean value of the lognormal distribution appears more accurate. Generally, the values of lognormal mean, the normal mean and d_{50} correlate for all samples.

Table 4: Parameters regarding the distribution of the maximum Feret diameter $\delta_{F,max}$, measured with label analysis, using the sieving analysis q3. SD for standard deviation.

Sample	d_{10} [µm]	d_{50} [µm]	d_{90} [µm]	Mean lognormal [µm]	SD lognormal [µm]	Mean normal [µm]	SD normal [µm]
C3E	19,3	32,6	48,8	32,9	1,4	33,9	11,6
C5E	22,6	37	53,5	37,1	1,4	37,9	11,8
G3W	21,3	38,1	61,9	38,6	1,5	40,7	16,1
G3WB	21,1	39,2	61,9	39	1,5	41,3	16,2
G5WB	23,3	39,3	60,2	39,5	1,4	40,9	13,8
G3E	22,4	41,3	63,3	40,5	1,5	42,6	15,5
GC3E	20,1	34,4	55,1	34,8	1,5	36,3	13,2

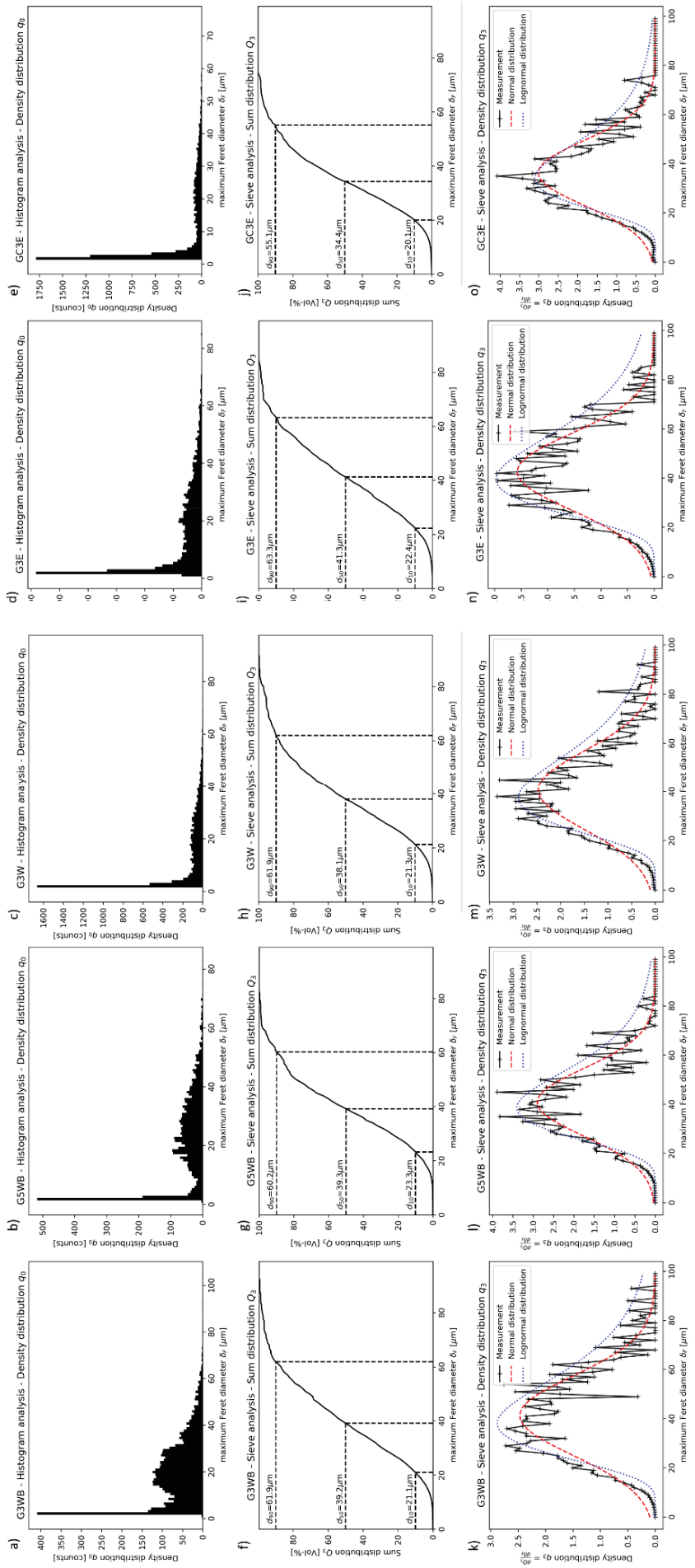

Figure 25: Particle size analysis via histogram analysis (density distribution q_0) and sieving analysis (density distribution q_3). Particle size analysis via histogram analysis (density distribution q_0, a to e) and sieving analysis (sum distribution Q3, f to j, and density distribution q_3, k to o).

3.8 RAMAN investigations

A chemical analysis of the substrate was performed with a RAMAN set-up. RAMAN measurements were performed in a LabRAM HR-800 system (Horiba Jobin Yvon, Villeneuve d'Ascq, France) using a 633 nm HeNe laser as excitation source. Measurements were performed in backscattering configuration with a 100× longworking distance objective (LMPLFLN, Olympus, Tokyo, Japan). The confocal pinhole was left full open (i.e. 1000 µm width). The inelastically scattered light was dispersed with an 1800 gr/mm grating and collected with a Peltier-cooled Charged Coupled Device (CCD) detector.

The spectra were measured at different positions on the sample surface, covering the pore ground as well as the fractured surface of the samples which is supposed to be the matrix surface. The raw RAMAN spectra were then compared to spectra of $BaTiO_3$ in papers such as [67] and [68]. Also, RAMAN spectra were measured for RAMAN shifts from 800 to 1800 cm^{-1}; this spectral range is useful to determine whether there is any unreacted carbon in the sample.

Figure 26: Picture of RAMAN set-up Horiba LabRAM HR Evolution [69].

4 Results

4.1 Processing evaluation

The density of corn starch was 1.4975 g/cm³ with a standard deviation of 0.0014 g/cm³. The weight loss in the oven was 10.81 %. This weight loss was considered when calculating the amount of pore formers in the $BaTiO_3$ – pore former mixture, as the mixture would be dried in oven before being pressed.

The calcined $BaTiO_3$ powder had a particle size of 800 to 1000 nm, as estimated from SEM images. It was mixed to pore formers as described in section “Mixing with pore formers” (3.2). Relevant parameters regarding mixing are listed in Table 5.

Table 5: Porous BaTiO3 - samples, listed with the relevant processing parameters. PF for pore former. Sample GC3E contains 15 vol% graphite and 15 vol% corn starch.

Sample name	Pore former (PF)	Solvent	Binder	Vol-% PF	Comments
G3W	Graphite	Water	No	30	Broke d. pressing
G3WB	Graphite	Water	Yes	30	
C3E	Corn starch	Ethanol	No	30	
G5WB	Graphite	Water	Yes	50	Broke d. pressing
C5E	Corn starch	Ethanol	No	50	Broke d. sintering
GC3E	Graphite and Corn starch	Ethanol	No	30 (15 + 15)	Broke d. pressing
G3E	Graphite	Ethanol	No	30	Broke d. pressing

The samples G3W and G3WB had 30 vol-% pore former (graphite). The only difference between the samples was that for G3WB a binder (Resigel) was added. This way, the greens were prevented from breaking during pressing. However, the adding of a binder led to formation of solid agglomerates during oven drying (after wet ball mixing). The agglomerates could be disrupted during sieving. However, the sieving process took longer. This led to a higher exposure of the pore former to mechanical stress. Therefore, the pore former particles could have been damaged which would lead to a change in the pore morphology. Further investigations regarding the pore morphology are done with X-ray computed tomography in Leoben.

In the case of corn starch as pore former (C3E and C5E), the mix had to be done with ethanol. With water, strong agglomerates were formed that could be eliminated only by milling in a mortar. Therefore, ethanol was used as solvent. The green bodies with corn starch did not tend to break while pressing. Therefore, no binder was added.

For G5WB, the same additives were used as for G3WB, with 50 vol-% pore former. The green body of G5WB broke, although a binder was used.

In the case of GC3E, both corn starch and graphite were used as pore formers. The powders were added in equal volume percentage to the $BaTiO_3$ powder, ethanol was used as solvent. The green body broke while pressing. G3E also broke while pressing.

Sample C5E broke during sintering. It is assumed that the rapid burn out of the corn starch particles inside the green led to internal stress in the green.

4.2 Density & porosity estimation via geometrical and Archimedes method

The density of the samples was measured using the geometrical method and the Archimedes method as described in section 3.4. A relative density was then calculated. From the relative density, a porosity is calculated. The densities of the samples are listed in Table 6. For illustration purposes, a diagram of the pore former part and the porosities calculated with both methods is shown in Figure 27.

Table 6: Relative densities and porosities of the porous samples, calculated with the geometrical method and the Archimedes method. Sample GC3E contains 15 vol% pore former graphite and 15 vol% pore former corn starch.

Sample name	Vol-% $BaTiO_3$-matrix	Relative density, calculated using the geometrical method	Relative density, calculated using the Archimedes method	Vol-% pore former	Porosity, calculated using the geometrical method	Porosity, calculated using the Archimedes method
G3W	70%	66,11%	88,90%	30%	33,89%	11,10%
G3WB	70%	74,63%	90,08%	30%	25,37%	9,92%
C3E	70%	71,77%	89,31%	30%	28,23%	10,69%
G5WB	50%	61,21%	93,71%	50%	38,79%	6,29%
C5E	50%	-	96,04%	50%	-	3,96%
GC3E	70%	68,67%	89,85%	30% (15%+15%)	31,33%	10,15%
G3E	70%	68,77%	89,91%	30%	31,23%	10,09%

The values of relative density diverge significantly depending on the method used to measure the relative density. In the case of G3WB, the geometrical method yields a relative density of about 75% while the Archimedes method yields 90%. The volume content of pore former in the G3W mixture was 30%. Therefore, a relative density of 70% was expected. In the case of G5WB, the content of pore former was higher compared to G3WB. Therefore, the relative density is expected to be lower. The relative density measured with the geometrical method follows the expected trend while the Archimedes method yields higher values of relative density.

The inverse trend for the densities measured with Archimedes method and the Geometrical method can be caused by the water entering the pores of the samples. This way, the density would be overestimated (measuring with Archimedes method). The higher the porosity, the higher is the probability that the pores are interconnected which would lead to more pores being filled by water.

For the geometric measurements, the samples were measured with a micrometer to determine the volume of the samples. Calculating the volume, it is assumed that the sample

is an ideal cylinder with flat plane surfaces on top and bottom. However, the edges were slightly rounded. Also, the sample surface had a certain roughness. This could have led to an overestimation of the volume and the resulting porosity in the geometric measurements.

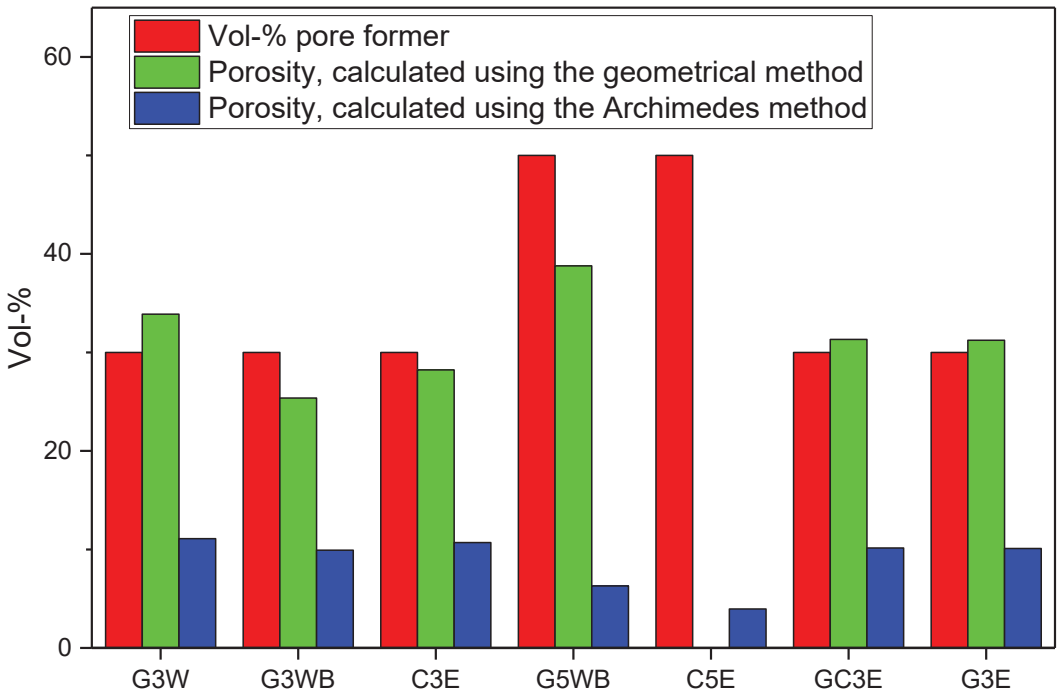

Figure 27: Chart of porosities and pore former part.

4.3 Qualitative characterization of the microstructure in 2D via SEM

The microstructure of the samples was investigated both on the fractured surface as well as on the polished surface. Images are taken with a SEM. The fractured surface neither requires the sample to be cut nor polished. A green body is difficult to polish due to its structural instability. Therefore, the fractured surfaces of the green and the sintered samples were investigated with SEM and compared. To compare the microstructure of the sintered samples, SEM images were taken on the polished surface of the samples. The pore structure is easier to compare on a flat surface. The appearance of the pores is not distorted by the roughness of the surface as it would be on a fractured surface. In Table 7, results of the qualitative investigations of the samples via SEM are summed up. The pore size, the pore shape and the connectivity of the pores are estimated qualitatively from 2D images.

Table 7: Results from the qualitative investigations of the samples in 2D via SEM.

Samples	Pore former (PF)	PF [vol %]	estimated pore size [µm]	Pore shape	Connectivity
C3E	Corn starch	30	10 to 30	rounded	~
C5E	C	50	20 to 40	rounded	++
G3W	G	30	10 to 30	elongated	~
G3WB	G	30	10 to 30	elongated	~
G3E	G	30	20 to 60	elongated	+
G5WB	G	50	20 to 40	elongated and isometric	+
GC3E	G + C	30	10 to 30	elongated and isometric	~

Figure 28 shows SEM images of the fractured surface of G3W, of both the green body (Figure 28a) and the sintered sample (Figure 28b). In Figure 28b, the elongated pores left by the pore former are clearly visible. However, it is difficult to correlate the pores to the pore former in the green in Figure 28a.

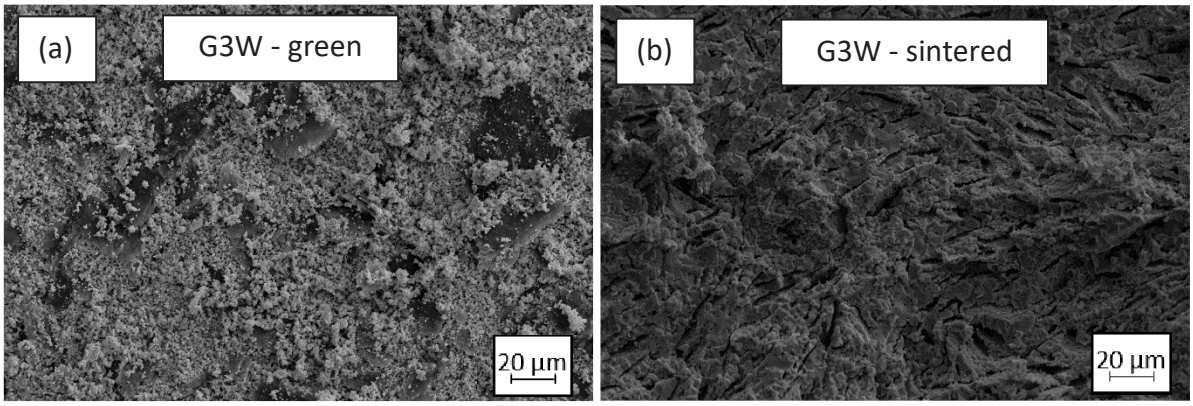

Figure 28: SEM images of fracture surfaces of green body (a) and sintered sample (b) of G3W. In (a), the graphite lamellas are visible as a darker contrast with respect to the BT powder. In (b), elongated pores can be seen. These result from the burnt-out graphite particles.

4.3.1 Comparing the microstructure of samples produced with the same pore former and varying mixing parameters (G3W, G3WB and G3E)

The sintered samples were embedded in resin, cut and polished. At first, three samples with 30 vol% pore former were prepared, where the pore former was graphite. Three different configurations of binder and solvent were prepared. The microstructure was studied with the SEM. A SEM image of the polished cross section of each sample is shown in Figure 29. Generally, the orientation of the pores appears to be randomly distributed. G3W (Figure 29a) and G3WB (Figure 29b) both were processed with water as solvent. In G3WB, a binder was added. The addition of the binder has a significant effect on pore size distribution and morphology. In G3W (Figure 29a), 2 types of pores appear. One type of pores is similar in size and shape to the graphite particles (elongated, estimated 25µm in length). Therefore, these

pores are supposed to be the ones left by the pore former. Then, there are also several smaller pores between the grains of the $BaTiO_3$ matrix. These pores are addressed to as intergranular pores and originate from incomplete densification of the matrix. Further, in G3W (Figure 29a) a darker contrast ascribed to some resin which has infiltrated the material can be seen, an indication that the pores are interconnected. This feature is not visible in G3WB (Figure 29b). In the sample G3WB, pores left by the pore former are well visible. They correspond well to the pores in G3W (Figure 29a) in size and shape. No intergranular pores can be seen on G3WB (Figure 29b), meaning that the ceramic matrix is well densified.

Comparing the microstructures of G3W (Figure 29a) and G3E (Figure 29c), both have intergranular porosity. Generally, G3W (Figure 29a) appears to have smaller pores deriving from the pore former. This means that the pore former was more agglomerated in G3E. The bigger pores in G3E are infiltrated by resin, again indicating an interconnected network of pores.

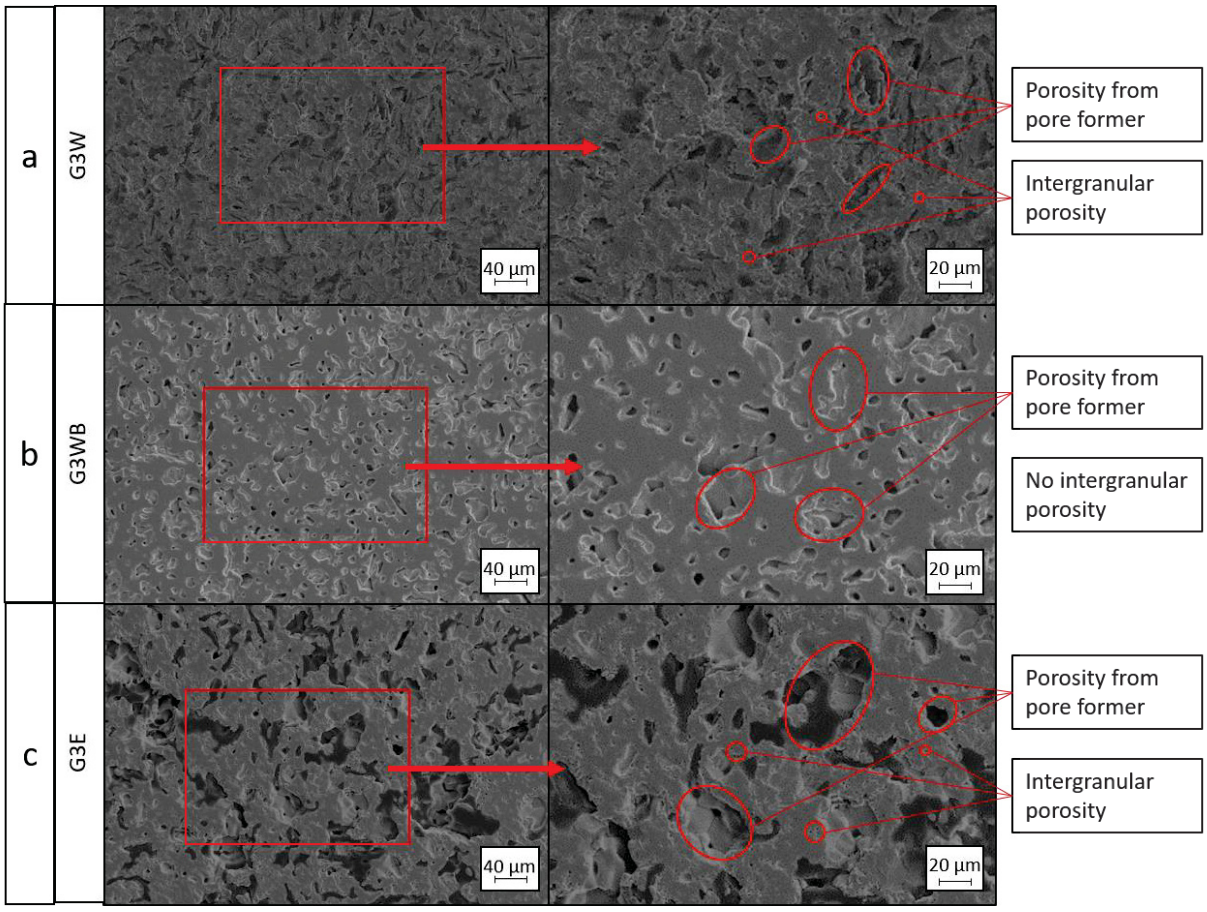

Figure 29: 2D - SEM images of the polished surfaces of the samples G3W(a), G3WB(b) and G3E(c).

4.3.2 Comparing the microstructures of samples produced with different pore formers (G3E, C3E and GC3E)

Samples are prepared using different pore formers, namely graphite and corn starch. The total pore former content for each sample was 30 vol-%. For G3E, graphite was used, for C3E corn starch. For GC3E, both pore formers were used in equal proportions (15vol% graphite, 15vol% corn starch). For all samples, ethanol was used as solvent, no binder was added. The sintered

samples were cut and polished. The polished surface was investigated with SEM. Images are shown in Figure 30.

In the microstructure of G3E (Figure 30a), a mix of elongated pores and isometric pores is visible. In C3E (Figure 30b), the pores appear more rounded. The pores appear bigger in G3E, compared to C3E. In G3E, several bigger pores indicate that the pore former is agglomerated, as already described in section 4.3.1. The size of several bigger pores in C3E is estimated larger than the particle size of the added corn starch (estimated about 10-20µm). This leads to the conclusion that a fraction of the corn starch particles could not be completely de-agglomerated during mixing, like G3E. However, there are many isolated spherical pores of about 10-20 µm that can be attributed to single corn starch particles.

Comparing C3E (Figure 30b) and GC3E (Figure 30c), the porosity appears similar in both cases. In GC3E, there are more elongated pores. Position and orientation of the elongated pores are randomly distributed inside the sample. Cutting the sample, the pores are cut at different positions and angles. Looking at the cut surface, pores have a different appearance depending on their position and orientation. For G3WB and GC3E, this might lead to a misinterpretation of the image. Elongated pores can have a round appearance. Therefore, the fraction of elongated pores is underestimated from the SEM images.

To sum up, in C3E and GC3E, the pores are evenly distributed, and the pore size is in the same order of magnitude. In G3E, the degree of agglomeration of the pores appears higher leading to pores in a size range of 20 to 60 µm, whereas pores in C3E have a size of 10 to 30 µm. In G3WB, the pores have a size of about 10 to 30 µm. Comparing G3WB with the samples C3E and GC3E, the pores have a more elongated shape. In C3E, the pore shape is more rounded. GC3E has a mix of rounded pores and elongated pores.

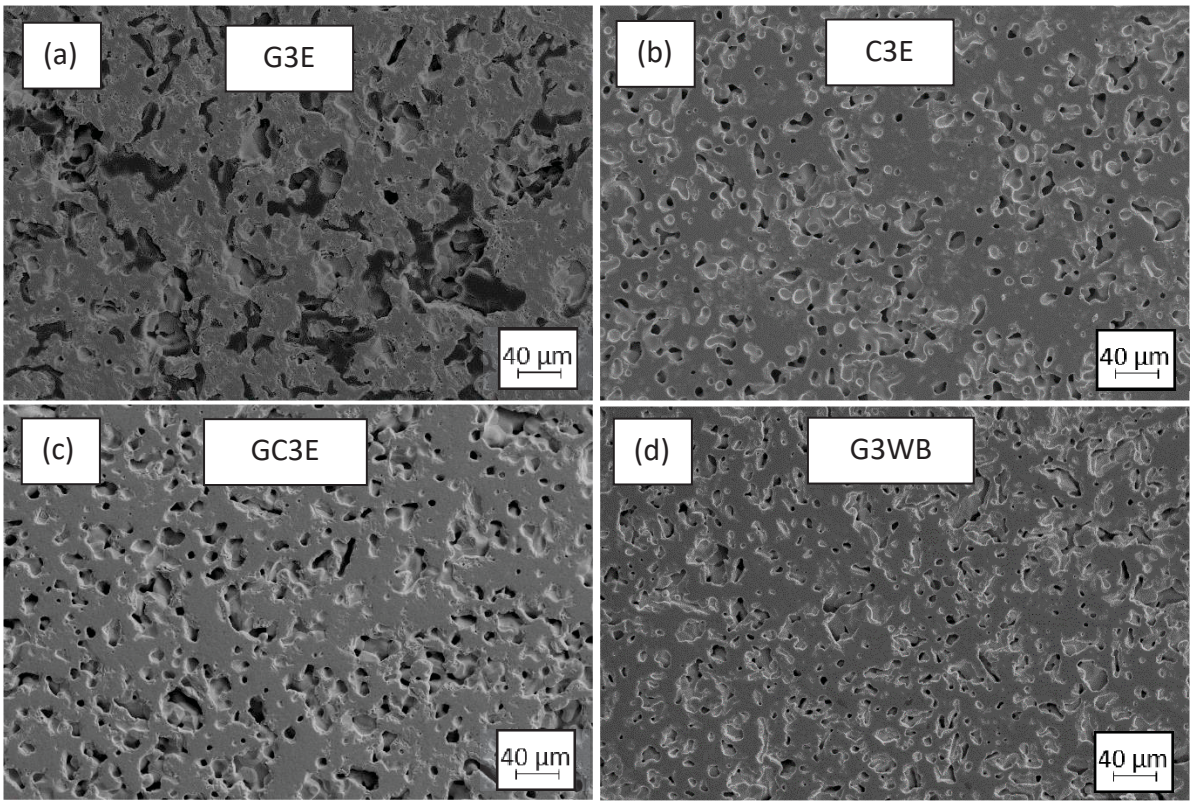

Figure 30: 2D - SEM images of the polished surfaces of the samples G3E(a), C3E(b), GC3E(c) and G3WB(d).

4.3.3 Comparing the microstructures of samples produced with varying amount of pore former corn starch (C3E and C5E)

C3E was prepared with 30 vol% corn starch, C5E with 50 vol% corn starch. The sintered samples were embedded, cut and polished. SEM – images of the polished cross sections of the samples are shown in Figure 31.

Looking at Figure 31, the pore shapes of C3E and C5E are similar. In C5E, there are more pores (i.e. higher porosity), the size of the pores is higher (about 20 to 40 µm) and the pores have a higher connectivity. In C3E, there are several isolated pores.

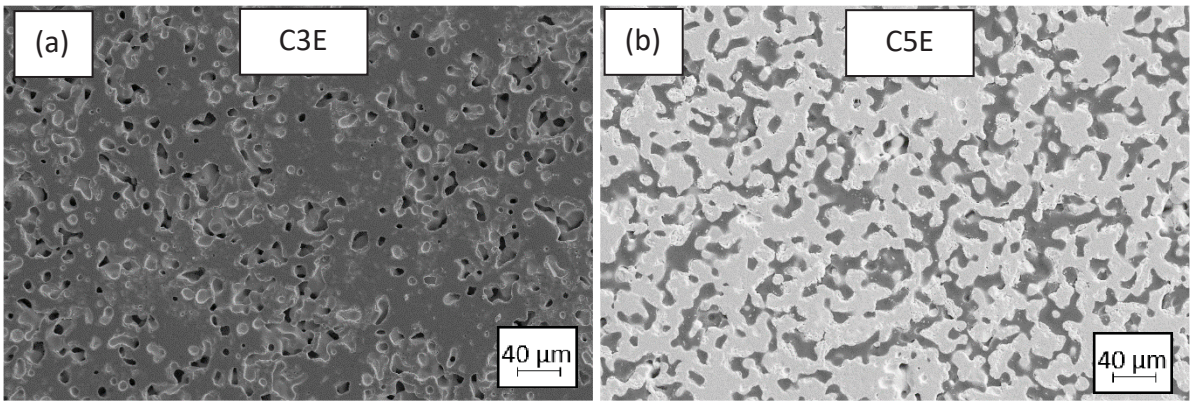

Figure 31: 2D - SEM images of the polished surfaces of the samples C3E(a) and C5E(b).

4.3.4 Comparing the microstructures of samples produced with varying amount of pore former graphite (G3WB and G5WB)

G3WB was prepared with 30 vol% graphite, G5WB with 50 vol% graphite. The sintered samples were embedded, cut and polished. The polished surfaces were investigated with the SEM. Images are shown in Figure 32.

Both in G3WB and G5WB, the pores have a similar shape. G5WB has a higher porosity. Also, there are more interconnections between pores. The pore size is estimated higher in G5WB (about 20 to 40 µm).

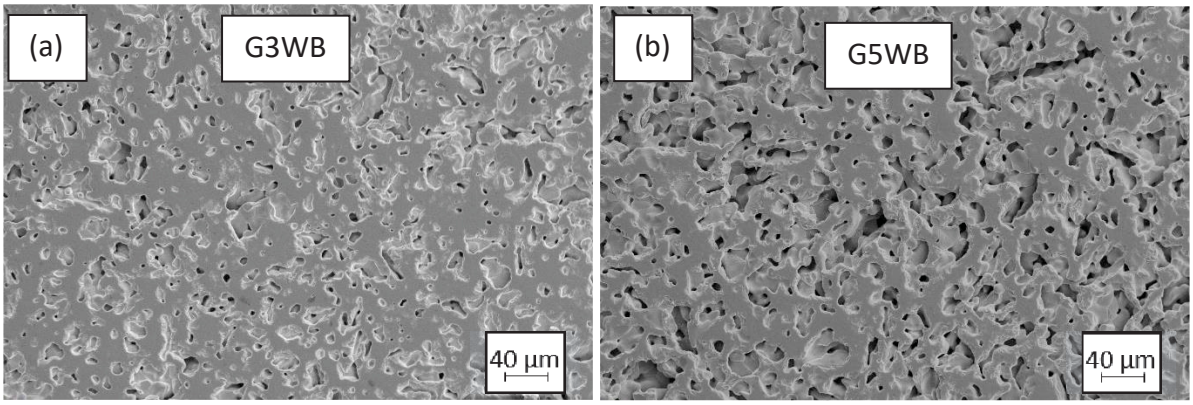

Figure 32: SEM images of the polished surfaces of the samples G3WB(a) and G5WB(b).

4.3.5 Microstructure of G5WB on the border

On the border of the sample G5WB, a change in contrast is visible. This phenomenon is shown in Figure 33. The sample was embedded in resin before. Therefore, it is assumed that the resin impregnated the sample up to a certain point before hardening. This leads to the conclusion that the pores in G5WB are highly interconnected.

At the border of the sample, most pores are filled with resin. Several pores that appear isolated in the image, are filled with resin. This leads to the conclusion that there are interconnections between the pores that are not visible in the image. Only the interconnections at the surface are visible in the images. Pores might appear isolated on the surface but be interconnected at a point below the surface.

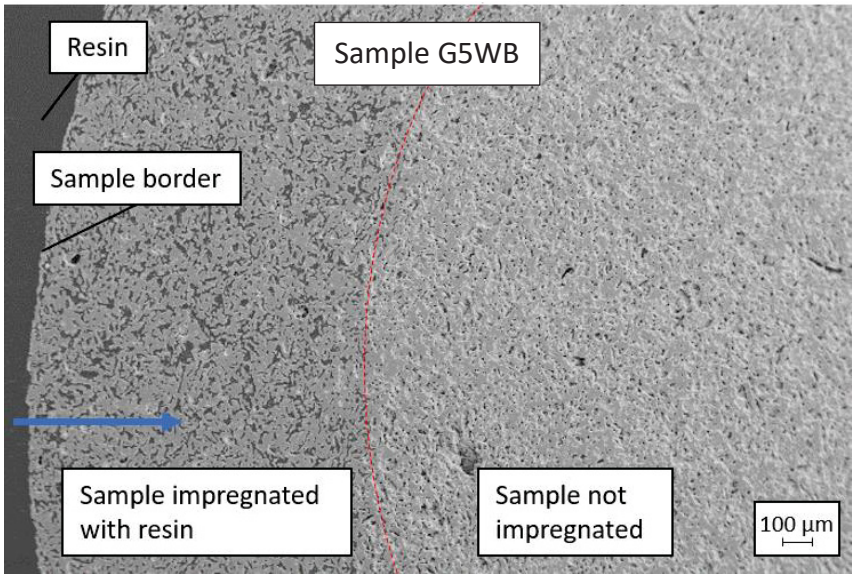

Figure 33: SEM image of the border of sample G5WB. Resin impregnated the sample, indicating that most of the pores are interconnected.

4.4 3D porosity from µ-XCT measurement

Each segmented VOI is a binarized representation, where the grey values of the voxels represent either $BaTiO_3$ or pore phase. The porosity is determined by calculating the fraction of the volume of the pore phase and the total volume ($BaTiO_3$ and pore). The volume of $BaTiO_3$ and pore phase is the sum of the respective voxels multiplied by the volume of a voxel.

To make a statistical evaluation of the samples, the VOI of each sample is cut into 8 sub-volumes. Each sub-volume is analysed separately regarding its porosity. A mean value and a standard deviation are calculated.

The statistical evaluation of the porosity of each sample is shown in Table 8, with mean value and standard deviations from the measurements with µ-XCT and with the geometric method. Also, the difference of the mean values for the measurements is shown. For illustration purposes, the mean values are shown in a bar chart (Figure 34) with error bars representing the standard deviation of the measurements.

Table 8: Porosity, measured with µ-XCT and with the geometric method.

Sample	Pore former	PF part	Porosity in µ-XCT	standard deviation	Porosity geometric	standard deviation	Porosity difference
C3E	CS	30%	23,28%	1,91%	28,23%	5,75%	4,95%
C5E	CS	50%	33,87%	3,36%			
G3W	G	30%	25,88%	3,28%	33,89%	3,99%	8,01%
G3WB	G	30%	24,78%	6,24%	25,37%	2,13%	0,59%
G5WB	G	50%	31,20%	3,11%	38,79%	3,70%	7,59%
G3E	G	30%	22,47%	1,75%	31,23%	2,42%	8,76%
GC3E	G + CS	30%	24,19%	2,86%	31,32%	2,76%	7,13%

4.4.1 Measurement analysis

Generally, in the mean value of porosity there is a difference between the geometric and the µ-XCT measurement. This difference is similar for most of the samples, at about 5 - 10 %. This indicates a possible systematic error between the measurements. For the geometrical measurements, possible sources of error are discussed in section 4.2, concluding that the geometric measurements possibly overestimated the porosity.

As already discussed in section 3.7.2, a portion of the porosity of the samples (intergranular porosity) could not be detected via µ-XCT. This may have led to an underestimation of the porosity in the samples measured via µ-XCT.

It must be noted that the error bar for the geometric measurements represents the standard deviation of the measurements of the mass, length and the diameter of the cylinder-like samples calculated via propagation of error to a standard deviation of the porosity of the samples. Measuring with µ-XCT, different volumes inside the sample are measured and therefore the deviation of the measurements represents local variations of the porosity inside the samples.

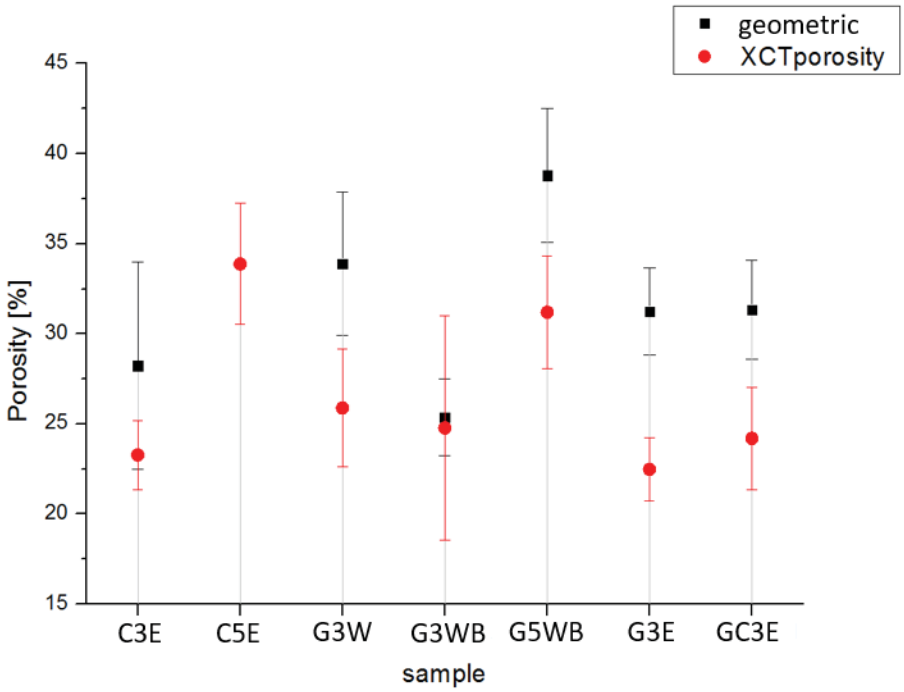

Figure 34: Porosity, measured with µ-XCT and with the geometric method.

4.4.2 Analysis of the sample porosities

As shown in Figure 34, both in the geometric measurements and the µ-XCT analysis, a trend to higher porosity with higher pore former part can be seen. G5WB (mixed with 50 vol% pore former graphite) has a significantly higher porosity both in the geometric (38,79%) and the µ-XCT measurement (31,2%) than G3WB (30 vol% pore former graphite, porosity geometric 24,78 %, µ-XCT 25,37 %). This also counts for C5E (mixed with 50 vol% pore former corn starch), measured with µ-XCT (33,87 %), compared to C3E (30 vol% pore former corn starch, porosity geometric 28,23 %, µ-XCT 23,28 %). It was not possible to measure the geometric porosity of C5E because it broke during sintering.

Samples C3E, G3E and GC3E were produced with 30 vol% pore former and solvent Ethanol. In the µ-XCT measurements, the samples had the smallest porosity and the smallest standard deviation in porosity. The low standard deviation of the µ-XCT measurements indicates an evenly distributed porosity.

Samples G3W, G3WB and G3E were prepared with 30 vol% graphite. G3E has a slightly lower mean porosity than the other samples. G3E was mixed with Ethanol, G3W and G3WB with water.

The higher standard deviation of the porosity in G3WB indicates that the porosity is not as evenly distributed as e.g. G3E. This was not observed qualitatively on the SEM images.

4.5 3D pore structure analysis via topological skeleton

In Table 3, parameters regarding the processing of the samples are summed up. As evidenced in section 3.7.5, samples C5E, G5WB and G3E contained starring artefacts and therefore are not considered. The next step is to visually compare the skeletons of the samples. The skeletons give a visual impression of the pore distribution. Comparing the skeletons, one can intuitively compare the distribution of the pores regarding density and homogeneity. The radius of the pore channels is indicated by the colour of the lines. An impression can be gained if a sample has pores of higher or lower radius. Also, spatial variations in pore radius are compared. Samples produced at similar parameters are analysed and compared hereinafter.

4.5.1 Comparing the microstructures of samples produced with different pore formers (C3E and GC3E)

Skeletonized pore networks of C3E and GC3E are shown in Figure 35. Both samples were produced using Ethanol as solvent. C3E was produced with 30 vol-% pore former corn starch, GC3E with 15 vol-% corn starch and 15 vol-% graphite. The minimum, maximum, median, mean and the lognormal mean pore radius and the standard deviation (SD) of the pore radius are shown for samples C3E and GC3E in the table below:

Sample	min [µm]	median [µm]	mean [µm]	lognormal mean [µm]	max [µm]	normal SD [µm]
C3E	0,29	2,54	2,49	1,92	8,07	1,39
GC3E	0,29	0,98	1,39	0,96	6,20	1,12

Generally, median, mean and lognormal mean of the pore channel radii correlate well. The standard deviation of the pore radius is similar (1,39 µm in C3E, 1,12 µm in GC3E). Looking at Figure 35, both samples have a homogeneous distribution of pores. This is also indicated by the standard deviation (table above), which is similar in both samples. In GC3E, the distribution of pores is denser than in C3E, i.e. there are more pores per unit volume in GC3E than in C3E. The radius of the pore channels is smaller in GC3E (mean radius 1,39 µm) than in C3E (2,49 µm).

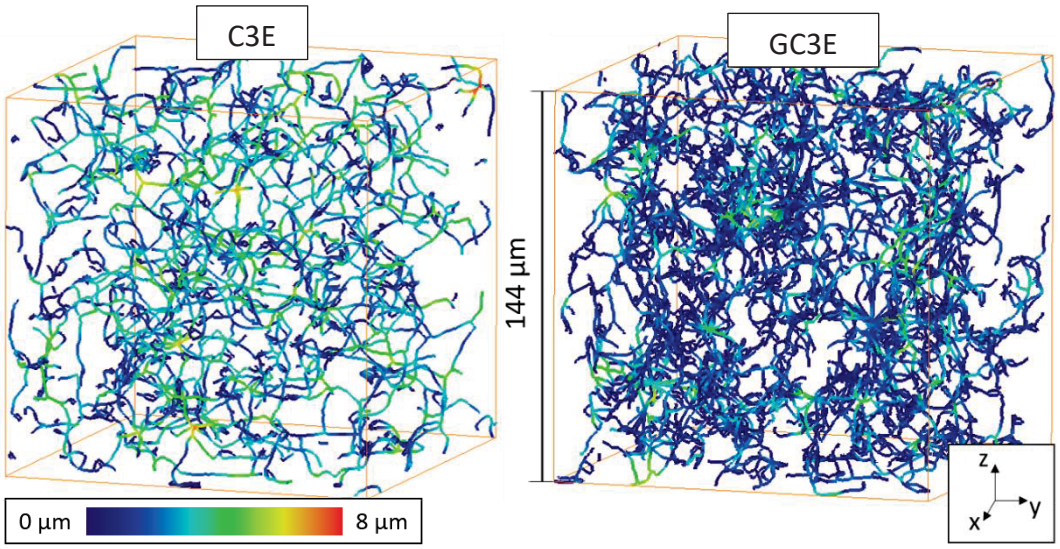

Figure 35: Skeletonized pore networks of samples C3E and GC3E. Colours are indicating the radius of the pore channels.

4.5.2 Comparing the microstructure of samples produced with the same pore former and varying mixing parameters (G3W and G3WB)

Skeletonized pore networks of G3W and G3WB are shown in Figure 36. G3W and G3WB were prepared with 30 vol% pore former graphite. In G3WB, a binder was added. The minimum, maximum, median, mean and the lognormal mean pore radius as well as the standard deviation (SD) are shown for samples G3W and G3WB in the table below:

Sample	min [µm]	median [µm]	mean [µm]	lognormal mean [µm]	max [µm]	normal SD [µm]
G3W	0,28	0,89	1,18	0,85	6,37	0,93
G3WB	0,29	2,52	2,78	2,23	9,69	1,61

Looking at Figure 36, G3W has a thinner and denser pore network, the radius appears uniform (like GC3E in Figure 35). The distribution of the lines is homogeneous. G3WB (mean radius 2,78 µm) overall has a higher pore radius than G3W (mean radius 1,18 µm). Also, the variation of the radius is stronger. The distribution of the lines in G3WB appears homogeneous. However, there are local differences in the pore radius. There are several pores on the bottom left in G3WB with higher pore radius. Apparently, the addition of a binder led to an increase of the pore radius. The standard deviation of the pore radii is higher in G3WB (1,61µm) than in G3W (0,93µm). This indicates a less homogeneous distribution of the pore radii in G3WB.

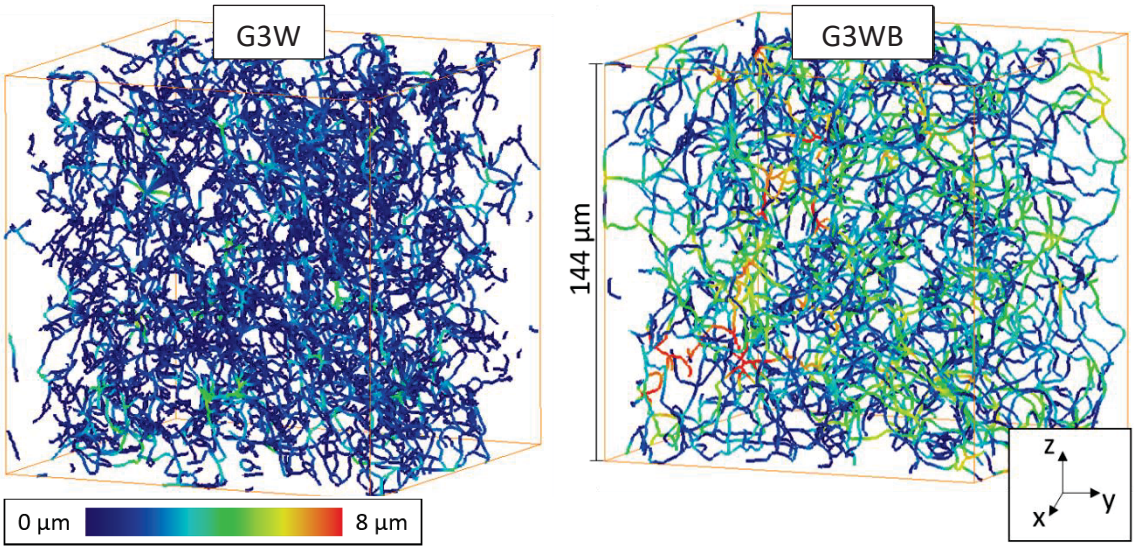

Figure 36: Skeletonized pore networks of samples G3W and G3WB. Colours are indicating the radius of the pore channels.

4.6 3D analysis of pores separated via watershed algorithm

4.6.1 Feret diameter and effective pore diameter

As explained in section “Theory”, the Feret diameter of a particle depends on the angle at which it is measured on the particle. In section 3.7.8, the maximum Feret diameter was measured for each sample. However, the maximum Feret diameter might lead to higher values of the pore sizes compared to what is measured in the sieve analysis of the pore former. According to Fernlund et al. [70], both the maximum and the minimum diameter should be considered to attain a more accurate pore diameter. Therefore, to compare the size distributions of the pores and the pore former particles, an effective diameter is calculated. This is done by measuring the maximum and the minimum Feret diameter of the pore and calculating the arithmetic mean value. The resulting sum distributions of C3E and G3E are shown in Figure 37. The statistical parameters are shown in Table 9.

Table 9: Parameters regarding the distribution of the effective Feret diameter

Sample	d10 [µm]	d50 [µm]	d90 [µm]	Mean normal [µm]	SD normal [µm]	Mean lognormal [µm]	SD lognormal [µm]
C3E	15,3	25,0	36,6	26,1	8,3	25,7	22,8
C5E	17,9	28,8	41,0	29,7	9,0	29,3	26,3
G3E	17,0	30,9	47,7	32,3	11,7	31,0	28,8
G3W	15,8	28,5	45,2	30,5	11,9	29,2	27,1
G3WB	15,8	29,6	47,0	31,3	12,3	29,9	27,9
G5WB	17,8	30,3	46,1	31,5	10,6	30,7	28,1
GC3E	15,9	26,4	41,0	27,8	9,7	27,1	24,5

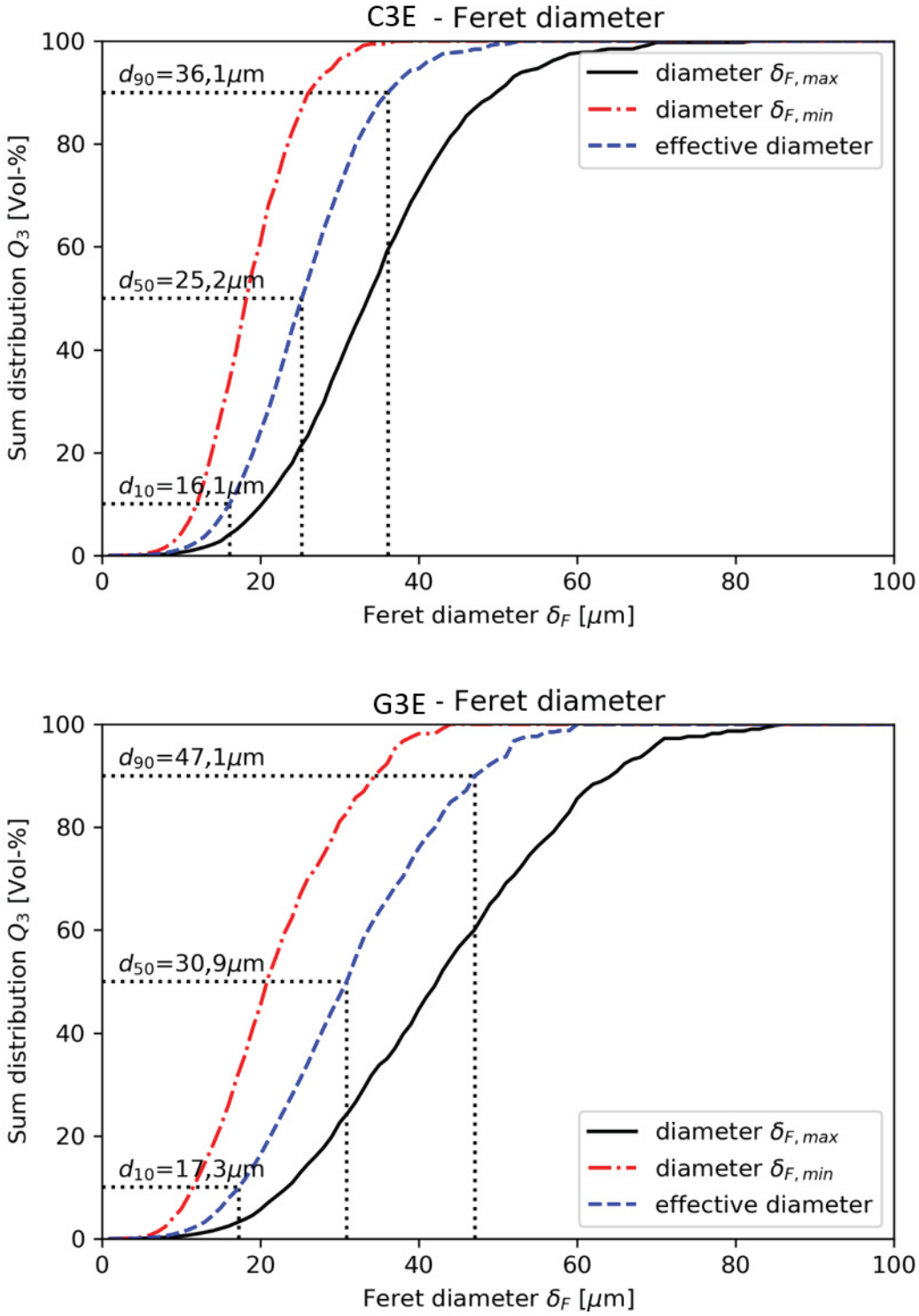

Figure 37: Minimum Feret diameter $\delta_{F,min}$, maximum Feret diameter $\delta_{F,max}$ and effective diameter of samples C3E and G3E. The Feret diameters were measured using the label analysis module in Avizo. Parameters d_{10}, d_{50} and d_{90} are shown of the effective diameter.

4.6.2 Comparison of effective Feret diameter $\delta_{F,eff}$

Feret diameter $\delta_{F,eff}$ is used as a measure of the pore size in the samples produced in this work. In the following sections, the distribution of the effective Feret diameter $\delta_{F,eff}$ is compared for samples produced with varying pore former part, changing pore former and changing the mixing medium/adding a binder.

4.6.2.1 Comparing the effective Feret diameter $\delta_{F,eff}$ of samples produced with the same pore former and varying mixing parameters (G3W, G3WB and G3E)

G3W, G3WB and G3E were prepared with 30 vol% pore former graphite. G3W was prepared with solvent water and no binder, G3WB with solvent water and a binder, G3E with solvent ethanol and no binder. For comparison of $\delta_{F,eff}$, sum distributions Q_3 of $\delta_{F,eff}$ are shown in Figure 38. Relevant parameters regarding the distribution of $\delta_{F,eff}$ are shown in following table:

Sample	d_{10} [µm]	d_{50} [µm]	d_{90} [µm]	Mean normal [µm]	SD normal [µm]	Mean lognormal [µm]	SD lognormal [µm]
G3E	17,0	30,9	47,7	32,3	11,7	31,0	28,8
G3W	15,8	28,5	45,2	30,5	11,9	29,2	27,1
G3WB	15,8	29,6	47,0	31,3	12,3	29,9	27,9
Graphite powder	10,8	27,0	53,0				

Looking at Figure 38, the samples have similar pore size distributions. G3W has the smallest lognormal mean $\delta_{F,eff}$ of G3W (29,2 µm), and Adding a binder led to a higher lognormal mean $\delta_{F,eff}$ (G3WB; 29,9 µm). The use of Ethanol as solvent led to the highest lognormal mean $\delta_{F,eff}$ (G3E; 31,0 µm). The difference between the lognormal mean $\delta_{F,eff}$ of G3W (29,2 µm), G3WB (29,9 µm) and G3E (31,0 µm) is small considering the difference in $\delta_{F,eff}$ to sample C3E (25,7 µm; produced with 30 vol% corn starch). Comparing $\delta_{F,eff}$ to the particle size of the pore former (Graphite, see table above), d_{50} of graphite (27,0 µm) and the samples (between 28,5 µm and 30,9 µm) are similar. A higher d_{10} and a lower d_{90} of the sample pores compared to the Graphite powder indicate that the pores have a narrower size distribution.

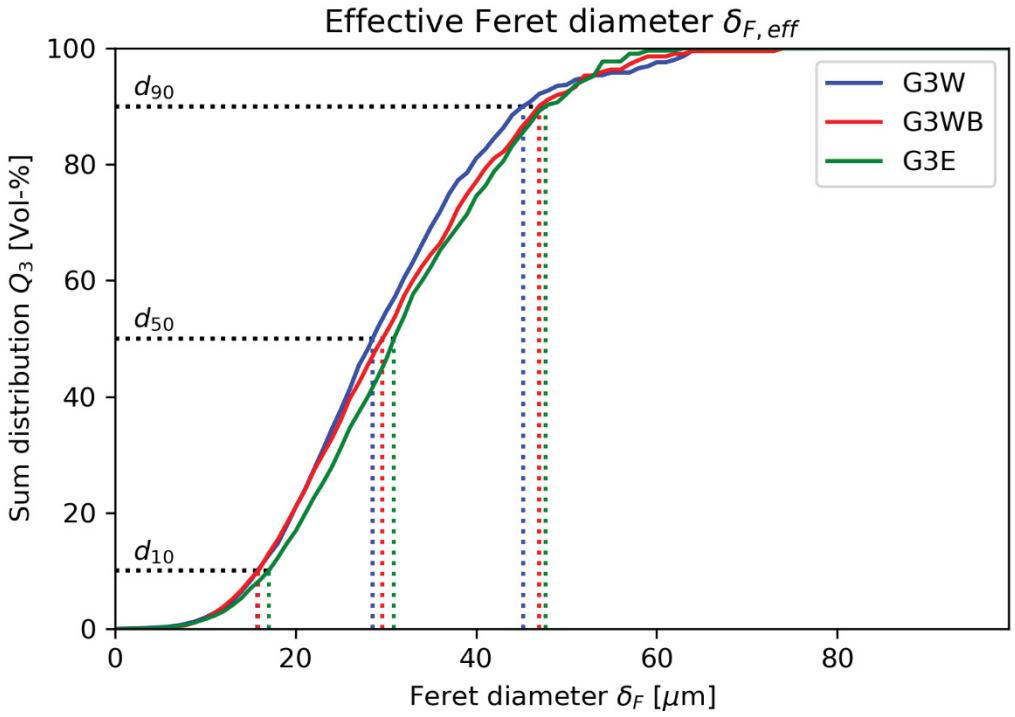

Figure 38: Sum distribution Q_3, of the effective Feret diameter $\delta_{F,eff}$, shown for samples G3W, G3WB and G3E. G3W was prepared with solvent water and no binder, G3WB with solvent water and a binder, G3E with solvent ethanol and no binder.

4.6.2.2 Comparing the effective Feret diameter $\delta_{F,eff}$ of samples produced with varying amount of pore former graphite (G3WB and G5WB)

Both samples G3WB and G5WB were prepared with pore former graphite. G3WB was mixed with 30 vol% pore former, G5WB with 50 vol%. For comparison of $\delta_{F,eff}$, sum distributions Q_3 of $\delta_{F,eff}$ are shown in Figure 39. Relevant parameters regarding the distribution are shown in following table:

Sample	d10 [µm]	d50 [µm]	d90 [µm]	Mean normal [µm]	SD normal [µm]	Mean lognormal [µm]	SD lognormal [µm]
G3WB	15,8	29,6	47,0	31,3	12,3	29,9	27,9
G5WB	17,8	30,3	46,1	31,5	10,6	30,7	28,1

Looking at the table above, the lognormal mean $\delta_{F,eff}$ of G5WB is higher than G3WB. For a direct comparison, the sum curves of G3WB and G5WB are shown in Figure 39. The curves cut at $\delta_{F,eff} \approx 35\ \mu m$. G3WB has a lower d_{10} and a higher d_{50} than G5WB, indicating a broader distribution of $\delta_{F,eff}$. This means that the sample produced with higher pore former part has a narrower distribution of $\delta_{F,eff}$.

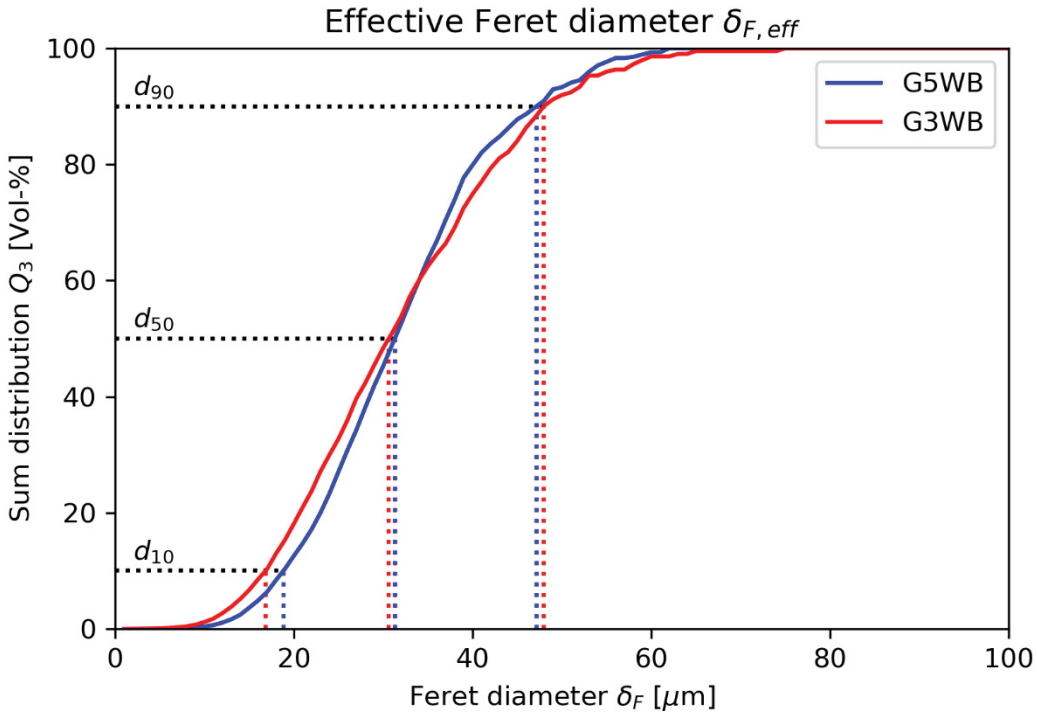

Figure 39: Sum distribution Q_3, of the effective Feret diameter $\delta_{F,eff}$, shown for samples G3WB and G5WB. G3WB was produced with 30 vol% pore former graphite, G5WB with 50 vol% graphite.

4.6.2.3 Comparing the effective Feret diameter $\delta_{F,eff}$ of samples produced with different pore formers (C3E, G3E and GC3E)

Samples C3E, G3E and GC3E were produced with 30 vol% pore former, solvent Ethanol and no binder. C3E was produced with pore former corn starch, G3E with graphite and GC3E with equal amounts of corn starch and graphite. For comparison of $\delta_{F,eff}$, sum distributions Q_3 of $\delta_{F,eff}$ are shown in Figure 40. Relevant parameters regarding the distribution are shown in following table:

Sample	d10 [µm]	d50 [µm]	d90 [µm]	Mean normal [µm]	SD normal [µm]	Mean lognormal [µm]	SD lognormal [µm]
C3E	15,3	25,0	36,6	26,1	8,3	25,7	22,8
G3E	17,0	30,9	47,7	32,3	11,7	31,0	28,8
GC3E	15,9	26,4	41,0	27,8	9,7	27,1	24,5

Looking at the table above, G3E has the highest lognormal mean $\delta_{F,eff}$ (31,0 µm), followed by GC3E (27,1 µm) and C3E (25,7 µm). The sum curve of $\delta_{F,eff}$ is shown in Figure 40. GC3E has a unimodal distribution of $\delta_{F,eff}$ between the C3E and G3E. This means that adding pore former graphite leads to a higher $\delta_{F,eff}$.

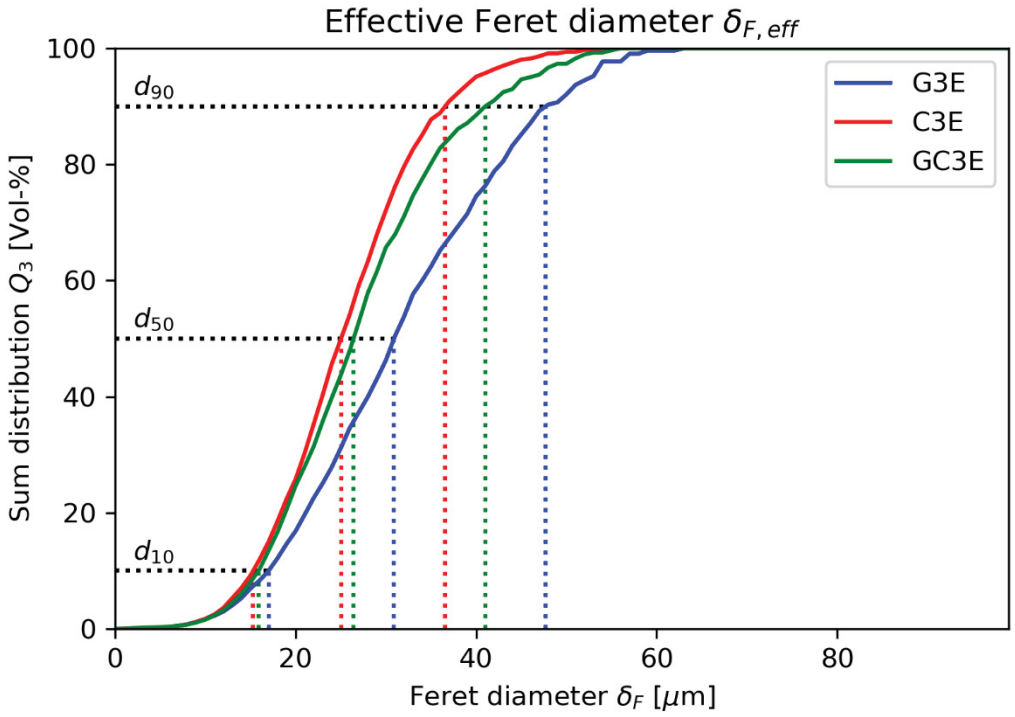

Figure 40: Sum distribution Q_3, of the effective Feret diameter $\delta_{F,eff}$, shown for samples C3E, G3E and GC3E. C3E was produced with pore former corn starch, G3E with graphite, GC3E with both corn starch and graphite.

4.6.2.4 Comparing the effective Feret diameter $\delta_{F,max}$ of samples produced with varying amount of pore former corn starch (C3E and C5E)

Both samples C3E and C5E were prepared with pore former corn starch. C3E was mixed with 30 vol% pore former, C5E with 50 vol%. For comparison of $\delta_{F,eff}$, sum distributions Q_3 of $\delta_{F,eff}$ are shown in Figure 41. Relevant parameters regarding the distribution are shown in following table:

Sample	d10 [µm]	d50 [µm]	d90 [µm]	Mean normal [µm]	SD normal [µm]	Mean lognormal [µm]	SD lognormal [µm]
C3E	15,3	25,0	36,6	26,1	8,3	25,7	22,8
C5E	17,9	28,8	41,0	29,7	9,0	29,3	26,3

Looking at the table above, C5E has a higher mean value of $\delta_{F,eff}$ (mean lognormal = 29,3 µm) than C3E (25,7 µm). For a direct comparison of $\delta_{F,eff}$, the sum curves of C3E and C5E are shown in Figure 41. The slopes of the curves appear similar, the curve of C5E is shifted to higher $\delta_{F,eff}$. The shift of the sum distribution to higher $\delta_{F,eff}$ in sample C5E suggests that, for corn starch, the higher pore former part led to a higher $\delta_{F,eff}$.

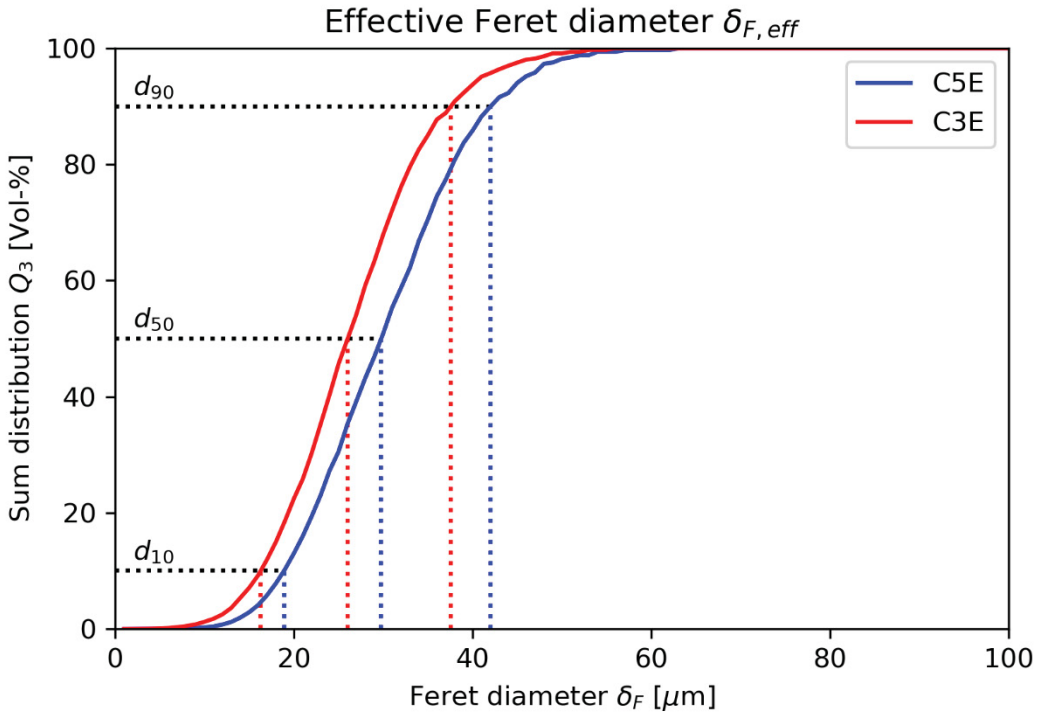

Figure 41: Sum distribution Q_3, of the effective Feret diameter $\delta_{F,eff}$, shown for samples C3E and C5E. C3E was produced with 30 vol% pore former corn starch, C5E with 50 vol% corn starch.

4.6.3 3D analysis of pores separated via watershed algorithm – Porosity and pore surface

The pore surface is the interface between pores and $BaTiO_3$. In this work, the pore surface area *Area3D* of a pore is defined as the number of side faces between the voxels assigned to the pore and voxels not assigned to the pore, multiplied by the area of a voxel side face. The pore surface depends on the porosity and the morphology of the pores, i.e. pore size and shape. Generally, also the interconnectivity of the pores plays a role. In this section, the pores are already separated, and the cut surface is counted as pore surface.

In Figure 42, the added surface area of the pores is plotted against the porosity for the samples analysed in this work. Assuming the pore morphology did not differ for each sample and if the pores were not interconnected, a linear correlation between the porosity and the pore surface would be expected.

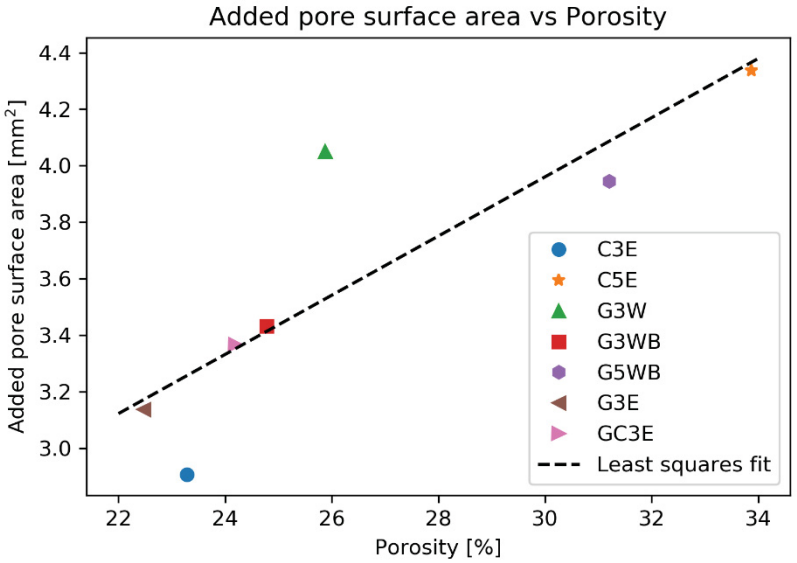

Figure 42: Added pore surface area vs porosity for the samples analysed in this work. To calculate the added pore surface area for each sample, in this figure is the added Area3D of all pores in the respective sample. The porosity values are taken from section 4.4. Generally, a trend between Area3D and the porosity is visible. Area3D increases monotonically with the porosity. C3E and G3W deviate from the trend.

Generally, a linear trend between the surface area and the porosity is visible, as shown by the linear fit. The surface area increases monotonically with the porosity. C3E and G3W deviate from the trend. Apparently, the pore morphology varies between the samples.

For G3W, the added pore surface area is higher with respect to the porosity. Comparing G3W to G3WB, the pore surface area of G3W (4,0 mm²) is significantly higher than in G3WB (3,4 mm²), the porosity is similar (25,88 % for G3W, 24,78 % for G3WB). This indicates that the pore shape of the samples is different, G3W having more elongated pores.

For C3E, the added pore surface area is low with respect to the porosity. Comparing C3E to G3E and GC3E, C3E has the lowest added pore surface area (2,9 mm²), G3E is in the middle (3,15 mm²), GC3E has the highest pore surface area (3,35 mm²). The porosity of C3E (23,28%) is between G3E (22,47%) and GC3E (24,19%). This indicates that C3E has more rounded pores.

As can be seen in Figure 42, the two samples (C3E and G3W) do not follow the linear trend. This leads to the conclusion that for samples C3E and G3W, the pore morphology, i.e. size and shape is different compared to the other samples.

4.7 RAMAN investigations

RAMAN spectra on the samples investigated in this work are shown in Figure 43. The peaks presumably deriving from $BaTiO_3$ are assigned to modes according to papers by authors such as Shiratori et al. [67] or Kholodkova et al. [68]. In Table 10, the RAMAN shift of the respective peaks is shown for all samples. For comparison, literature values are given below.

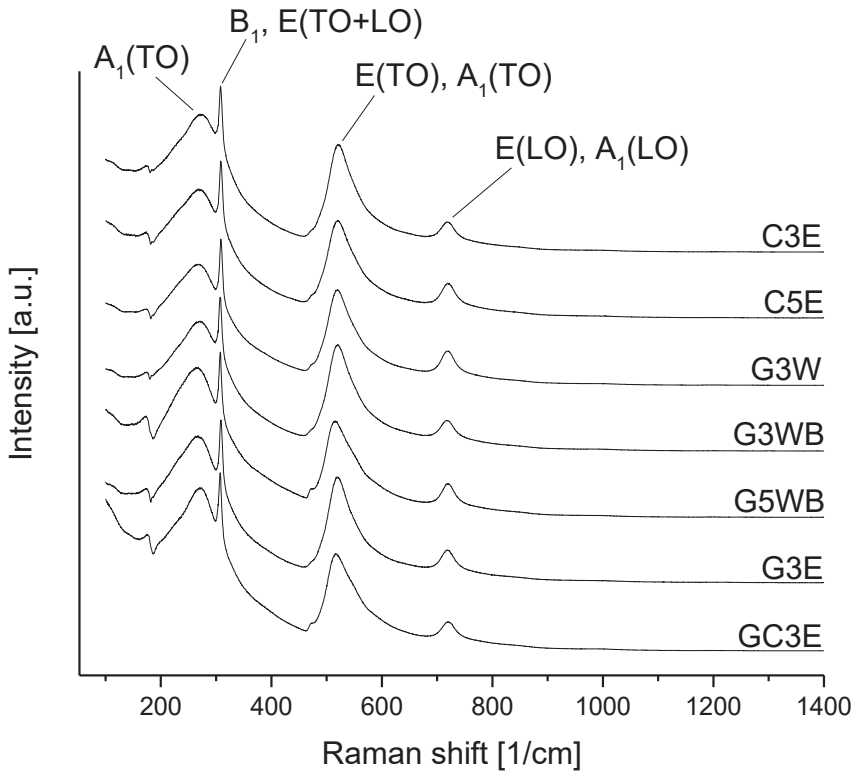

Figure 43: RAMAN spectra of porous $BaTiO_3$. Strong bands are labelled. Their position is then compared to literature values of $BaTiO_3$ in Table 10.

The RAMAN spectra of the samples are similar, their features resemble the spectrum of pure $BaTiO_3$ in the orthorhombic phase [71]. Spectra on the pore ground and in the matrix didn't show any significant difference. The introduction of different pore formers before sintering appears not to affect the chemical composition of the samples.

Table 10: RAMAN shift of peaks as labelled in Figure 43. Beneath, values from literature are shown for comparison.

	A_1(TO) mean [cm^{-1}]	A_1(TO) SD [cm^{-1}]	B_1, E(TO+LO) mean [cm^{-1}]	B_1, E(TO+LO) SD [cm^{-1}]	E(TO), A_1(TO) mean [cm^{-1}]	E(TO), A_1(TO) SD [cm^{-1}]	E(LO), A_1(LO) mean [cm^{-1}]	E(LO), A_1(LO) SD [cm^{-1}]
C3E	267,6	6,2	307,2	0,5	516,0	4,6	720,2	2,3
C5E	272,1	4,4	309,0	0,4	522,4	2,4	718,6	0,8
G3W	270,0	2,2	308,8	0,3	520,8	2,5	718,5	0,3
G3WB	267,0	2,6	306,5	1,0	515,0	3,4	717,8	2,5
G5WB	265,2	6,3	308,2	0,8	516,6	3,4	720,4	3,2
G3E	272,0	3,3	308,7	0,5	520,8	2,3	718,8	1,2
GC3E	269,5	8,2	307,5	0,6	517,3	3,7	719,5	1,7
Literature								
Shiratori et al.	257		306		515		716	
Kholodkova et al.	254		310		517		718	
Gajovic et al.	250		307		515		715	

In Figure 44, RAMAN spectra are shown for RAMAN shifts from 800 to 1800 cm^{-1}; this spectral range is useful to determine whether there is any unreacted carbon in the sample. For each sample, two spectra are shown. The spectra were measured at different positions on the sample surface. From Figure 2 it is evident that there are peaks (1000 cm^{-1}, 1200 cm^{-1} and 1450 cm^{-1}) that are not directly related to the $BaTiO_3$-spectrum. These peaks can be attributed to higher-order RAMAN scattering of $BaTiO_3$, which can be considered as the overtone of first-order RAMAN scattering [72]. Second-order RAMAN scattering is reported for a number of orthorhombic perovskites [73].

Other visible peaks do not appear in all measurements. These can be attributed to residuals from the pore formers or epoxy resin. The low intensity of the peaks indicates that they are present with only a small amount. Peaks at 1600 cm^{-1} indicate the presence of residual graphite in G3W, G5WB and G3E. C5E, which was prepared with corn starch, shows a peak at the same position. This leads to the conclusion that the peak does not clearly derive from the existence of residual graphite (or corn starch). Another possibility is the contamination of the sample with resin. The sample was embedded in resin for preparation purposes. Some of the resin infiltrated the sample. It is possible that the RAMAN spectrum shows traces of the epoxy resin, visible as carbon-related peak.

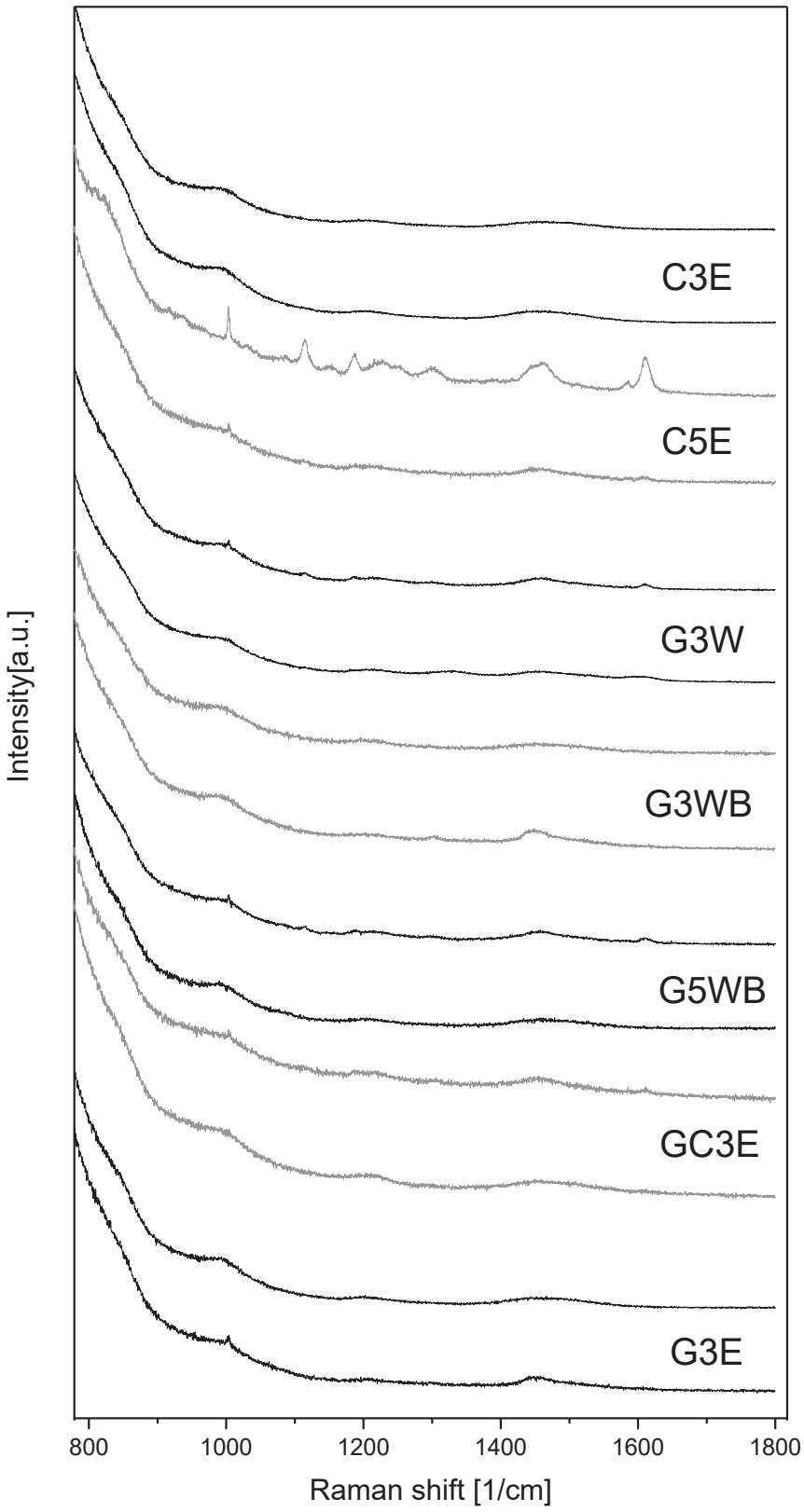

Figure 44: RAMAN spectra for porous $BaTiO_3$ samples. Spectra are shown for RAMAN shifts from 800 to 1800 cm^{-1}; this spectral range is useful to determine whether there is any unreacted carbon in the sample. For each sample, two spectra are shown. The spectra were measured at different positions on the sample surface. There are peaks (1000 cm^{-1}, 1200 cm^{-1} and 1450 cm^{-1}) that are not directly related to the $BaTiO_3$-spectrum.

In Figure 45, RAMAN spectra are shown of measurements on sample C3E, which was produced with pore former corn starch. The spectra were measured at different positions on the sample surface. Measuring RAMAN spectra on different spots of sample C3E, there were peak shifts and changes in the spectral signature of the RAMAN spectra. These changes could be due to (1) orthorhombic to tetragonal transition (from top to bottom of Figure 45) or also (2) to a change in orientation of crystallites. If the grains are very large, going from one grain with one orientation to another one with a different orientation could cause such changes [74]. Polarised RAMAN studies, as done in [75,76], would lead to a definitive conclusion about the nature of the changes in the spectra of C3E.

According to Gajovic et al. [71], the peaks at 250, 307, 515 and 715 cm^{-1} indicate the presence of orthorhombic or tetragonal $BaTiO_3$ phase. The lack of a peak at 640 cm^{-1} indicates that there is no hexagonal phase. The sharp peak at 307 cm^{-1} signals that all samples show presence of long-range ferroelectric phase [71]. According to Frey and Payne [77], the RAMAN spectra of tetragonal and orthorhombic phases are similar. Subtle differences in the spectra are reported in the range of 180 to 195 cm^{-1}. For single crystals of tetragonal $BaTiO_3$, a positive intensity peak can be observed at 180 cm^{-1} when the appropriate crystal orientation is chosen. For other orientations and for powders, often a negative peak is observed near 180 to 185 cm^{-1}. For the orthorhombic phase, a positive peak is visible at 193 to 195 cm^{-1}. The change in the RAMAN spectra in C3E measured at different positions suggests a coexistence of tetragonal and orthorhombic phase in the sample.

There are several reasons for the presence of a (stable) orthorhombic phase of $BaTiO_3$. According to Frey and Payne [77], a reduction in grain size (well beneath 100 nm) can lead to an enhanced stability of the orthorhombic phase at room temperature. According to Gajovic et al. [71] and Philippot et al. [60], the orthorhombic phase can be explained by possible strain of the matrix. The calcined $BaTiO_3$ particles have a particle size of 800 to 1000 nm. It is assumed that the grain size of the sintered $BaTiO_3$ is not significantly small to induce an orthorhombic phase. Therefore, the latter argument (strain) seems to count for C3E. Local strains of the $BaTiO_3$ matrix could have been induced by mechanical impact on the samples while cutting. Another possibility is that the pore former (corn starch) could have caused strains in the sample while burning out. This is also suggested by the fact that C5E, which was mixed with higher amounts of corn starch, broke during sintering.

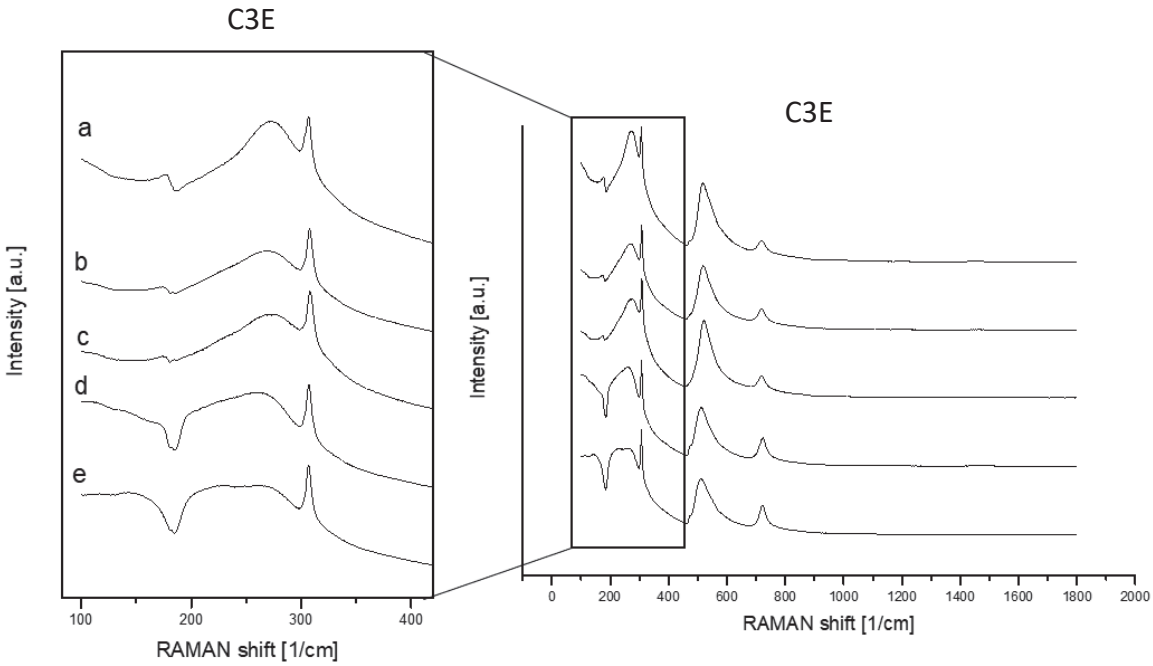

Figure 45: RAMAN spectra of sample C3E. The spectra were measured at different positions on the sample surface. Measuring RAMAN spectra on different spots of sample C3E, there were peak shifts and changes in the spectral signature of the RAMAN spectra. These changes could be due to (1) orthorhombic to tetragonal transition (from top to bottom) or also (2) to a change in orientation of crystallites. If the grains are very large, going from one grain with one orientation to another one with a different orientation could cause such changes [74].

5 Discussion

5.1 Chemical analysis via RAMAN

Investigations of the RAMAN spectra in section 4.7 led to the conclusion that the samples analyzed in this work consist in pure $BaTiO_3$ in the orthorhombic phase. Spectra on the pore ground and in the matrix didn't show any significant difference. The introduction of different pore formers before sintering appears not to affect the chemical composition of the samples. The sharp peak at 307 cm^{-1} (see peak of mode B_1, E(TO+LO) in Figure 43) signals that all samples show presence of long-range ferroelectric phase [71].

Changes in the RAMAN spectra in C3E (in the range of 180 to 195 cm^{-1}, shown in Figure 45) measured at different positions could be due to (1) orthorhombic to tetragonal transition (from top to bottom of Figure 45) or also (2) to a change in orientation of crystallites. If the grains are very large, going from one grain with one orientation to another one with a different orientation could cause such changes [74]. Polarised RAMAN studies, as done in [75,76], would lead to a definitive conclusion about the nature of the changes in the spectra of C3E. The (potential) coexistence of the phases is attributed to possible strain of the matrix ($BaTiO_3$) in the sinter process or while cutting the samples.

5.2 Comparing the pore size measured with different methods

In Table 11, results of the investigations of the pore size are summed up. The table includes the pore size estimated via SEM in 2D, the lognormal mean Feret diameter $\delta_{F,eff}$ from investigations of the porous structure separated via watershed algorithm (3D-µ-XCT), and the pore radius mean value from skeletonization (3D-µ-XCT).

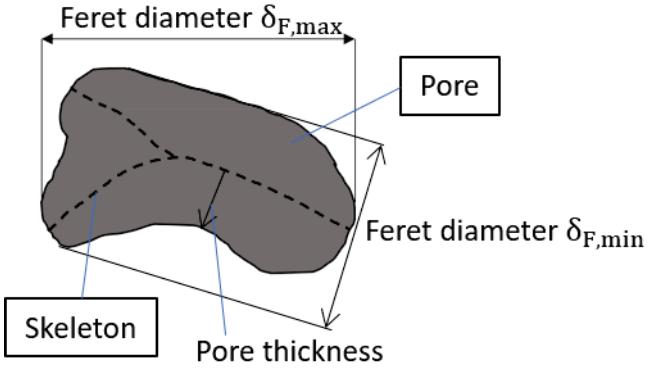

Figure 46: Scheme of Feret diameter δ_F and pore radius from skeletonization on a single pore. Feret diameter δ_F is the distance between 2 parallel lines (in 2D) or planes (in 3D) touching the object (i.e. the pore) on opposite sides. $\delta_{F,eff}$ is the mean of $\delta_{F,min}$ (i.e. the minimum δ_F) and $\delta_{F,max}$ (i.e. the maximum δ_F). Pore radius from skeletonization is the distance to the closest matrix (i.e. non-pore) voxel.

The pore size estimated via SEM (between 10 and 60 µm) and Feret diameter $\delta_{F,eff}$ (lognormal mean value = 25,7 to 31µm) correlate well. The radius from skeletonization is significantly smaller (between 1,18 µm and 2,78 µm). The difference of the values from skeletonization and watershed is attributed to the methodology of skeletonization, as shown in Figure 46. The pore radius from skeletonization can be interpreted as the radius of the pore channel. In case of a convex pore, $\delta_{F,eff}$ can be interpreted as the mean pore diameter. It is supposed that the

difference between $\delta_{F,eff}$ and pore radius indicates the pore shape. In the case of elongated pores or non-convex pores, the pore radius becomes smaller, the Feret diameter remains the same (or does not change as much as the pore radius). This appears to be the case for samples G3W and G3WB: $\delta_{F,eff}$ is similar (G3W 29,2 µm, G3WB 29,9 µm), the skeleton mean radius is different (G3W 1,18 µm, G3WB 2,78 µm). This indicates a different pore shape, with more elongated pores in G3W. From visual comparison of the cross sections of samples G3W and G3WB (e.g. Figure 15c and d), this statement appears to be valid.

Table 11: Results of investigations of the pore size via SEM (2D), Feret diameter analysis from µ-XCT (3D), and radius analysis from skeletonization (µ-XCT, 3D).

Samples	pore size estimated from SEM [µm]	mean lognormal $\delta_{F,eff}$ [µm]	skeletonization mean [µm]
C3E	10 to 30	25,7	2,49
C5E	20 to 40	29,3	-
G3W	10 to 30	29,2	1,18
G3WB	10 to 30	29,9	2,78
G3E	20 to 60	31,0	-
G5WB	20 to 40	30,7	-
GC3E	10 to 30	27,1	1,39

5.3 Pore morphology - interconnectivity of the pore structures

Looking at images of the cross sections from SEM, it appears that samples produced at lower pore former part have a considerable amount of isolated pore structures (see e.g. samples G3WB or C3E in Figure 30). However, skeletons of the 3D pore structure from µ-XCT evidence that all samples investigated in this work have highly interconnected pore structures (see Figure 35 and Figure 36).

5.4 Comparison of the pore morphology of the samples analysed in this work

The pore morphology analysis of the samples includes analysis of the pore size, the pore form and the spatial distribution of the pores.

5.4.1 Comparison of samples produced with the same pore former and varying mixing parameters (G3W, G3WB and G3E)

Pore size:

Generally, the pore size of the samples produced with graphite is in the same order of magnitude. Differences in pore size are attributed to the pore former being (slightly) agglomerated in the mixing procedure when a binder was added or when Ethanol was used as solvent.

- As shown in section 4.6.2.1, $\delta_{F,eff}$ of samples produced with graphite correlates well with the particle size of pore former graphite. Value d_{50} of graphite (27,0 µm) and the samples (between 28,5 µm and 30,9 µm) are similar. A higher d_{10} and a lower d_{90} of

the sample pores compared to the Graphite powder indicate that the pores have a narrower size distribution than the pore former.

- G3W (solvent water, no binder) yields the lowest $\delta_{F,eff}$ (mean lognormal = 29,2 µm), followed by G3WB (solvent water, binder, mean lognormal = 29,9 µm) and G3E (solvent Ethanol, no binder, mean lognormal = 31,0 µm).
- Results of $\delta_{F,eff}$ correlate well with the pore size estimated from investigations with SEM. In SEM, G3E (20 to 60 µm) showed bigger pores compared to G3W and G3WB (10 to 30 µm).

Pore shape:

In the investigations, G3W showed to have the pores with the most elongated shape, followed by G3WB and G3E.

- Pore radius from skeletonization revealed different radii of the pore network for G3W (mean radius = 1,18 µm) and G3WB (2,78 µm). As pointed out in section 5.2, the radius is an indicator of the pore shape. A smaller mean radius indicates that the pore has a more elongated shape. This means that G3W has pores of similar size like G3WB, but the pores are more elongated.
- The analysis of the pore surface area in section 4.6.3. led to the conclusion that the pore surface area of G3W (4.0 mm²) is significantly higher than in G3WB (3,4mm²). This indicates that the pore shape of the samples is different, G3W having more elongated pores. The results agree with results of radius from skeleton analysis (see point above).

Distribution of pores:

Generally, the porosity is distributed well in all samples. G3WB showed some local variations in the distribution of the pores.

- Skeletonized pore networks of G3W and G3WB (see Figure 36 in section 4.5.2) show differences regarding the distribution of pores: In G3W, the pores are evenly distributed. The distribution of the lines in G3WB appears homogeneous. However, there are local differences in the pore radius of G3WB. The standard deviation of the pore radii is higher in G3WB (1,61µm) than in G3W (0,93µm). This indicates a less homogeneous distribution of the pore radii in G3WB.
- Measurements of the porosity of the samples in 3D via µ-XCT (section 4.4) reveal a higher standard deviation of the porosity in sample G3WB (µ-XCT porosity standard deviation = 6,24%) than in G3W (3,28%) or G3E (1,75%). The standard deviation was calculated from porosities at different positions in the samples. A high standard deviation of the porosity therefore indicates that the pores are not evenly distributed throughout the sample.

5.4.2 Comparison of samples produced with different pore formers (C3E, G3E and GC3E)

Pore size:

Both $\delta_{F,eff}$ and the pore size in SEM are higher in the sample produced with graphite (G3E) than in the sample produced with corn starch (C3E). The reason is assumed to be the bigger size of the graphite particles.

- G3E has the highest $\delta_{F,eff}$ (lognormal mean = 31,0 µm), followed by GC3E (27,1 µm) and C3E (25,7 µm). The sum curve of $\delta_{F,eff}$ is shown in Figure 40. GC3E has a unimodal distribution of $\delta_{F,eff}$ between the C3E and G3E. This means that samples produced with pore former graphite have a higher $\delta_{F,eff}$. This also counts for G3W (mean lognormal = 29,2 µm) and G3WB (29,9µm).
- Results from SEM in 2D yield similar pore sizes for C3E and GC3E (10 to 30 µm) and higher pore sizes for G3E (20 to 60 µm).

Pore shape:

Generally, the assumption that the porous structure inherits the shape of the pore formers can be confirmed by the analysis in 3D (µ-XCT) and 2D (SEM). Samples produced with pore former graphite show more elongated pores compared to samples produced with corn starch.

- Analysis from skeletonization of the pore structure (section 4.5.1) revealed different radii of the pore network for C3E (mean radius = 2,49 µm) and GC3E (1,39 µm). As pointed out in section 5.2, the radius is an indicator of the pore shape. A smaller mean radius indicates that the pore has a more elongated shape. This means that GC3E has more elongated pores than C3E.
- From qualitative comparison of the samples by looking at cross sections on SEM (see Figure 30 in section 4.3.2) GC3E had more elongated pores than C3E.

5.4.3 Comparison of samples produced with varying amount of pore former (C3E, C5E, G3WB and G5WB)

Pore size:

Samples produced with corn starch show a clear tendency to higher $\delta_{F,eff}$ with higher pore former part. This was not the case for samples produced with pore former graphite.

- Investigations with SEM (section 4.3) revealed a higher pore size at higher pore former part for samples produced with corn starch as well as samples produced with graphite. Samples produced with 30 vol% pore former had pore sizes between 10 and 30 µm, samples with 50 vol% 20 to 40 µm.
- In samples produced with corn starch, $\delta_{F,eff}$ clearly increased at higher pore former content. Comparing C5E (50 vol% corn starch) to C3E (30 vol% corn starch), C5E had higher values of d_{10} (17,9 to 15,3 µm), d_{50} (28,8 to 25,0 µm) and d_{90} (41,0 to 36,6 µm). Comparing samples G5WB (50 vol% graphite) to G3WB (30 vol% graphite), G5WB had higher d_{10} (17,8 to 15,8 µm) and d_{50} (30,3 to 29,6 µm), but a lower d_{90} (46,1 to 47,0 µm).
- In this section, samples are compared that are produced with different pore formers and with different solvents (G3WB and G5WB with water, C3E and C5E with Ethanol).

Therefore, phenomena related to a different pore former can also be attributed to the change of the solvent. As discussed in section 5.4.1, the use of water as solvent can increase $\delta_{F,eff}$ for samples produced with graphite.

6 Conclusion

In this work, porous samples with distinct pore morphology/pore size and varying porosities were processed. Investigations in 2D via SEM and 3D via µ-XCT led to the conclusion that the pore morphology varied significantly changing the pore former. Samples produced with pore former graphite had more elongated pores than corn starch. The pore size distribution correlates well with the particle size distribution of the original pore former powder. In samples produced with solvent Ethanol, a higher pore size compared to the other samples was evidenced, which indicates that Ethanol led to agglomeration of the pore former powder while mixing.

Skeletonized 3D representations reveal that pore structures in all samples are highly interconnected. Generally, the pores are well distributed in all samples. The porosity is similar in samples produced with the same amount of pore former, regardless of the type of pore former. As expected, a higher pore former part resulted in an increase in porosity. From qualitative investigations of the skeletal 3D representations, it appears that the density of pores is slightly higher in samples produced with graphite than with corn starch at similar porosities. This also depends on the mixing medium and the use of a binder. The sample produced with graphite, with mixing medium water and no binder had a high density (i.e. number of pores per volume) of thin pores. The addition of a binder led to thicker pores and a lower density of pores.

Samples produced with graphite tended to break in the pressing procedure. This can be a problem with respect to reproducibility of the samples. The sample produced with 50 vol% corn starch broke during sintering. This can be attributed to the rapid burn out of the pore former and the resulting pressures due to the combustion of the pore former in the sinter process.

The 3D characterization yielded quantitative and qualitative results that led to a better understanding of the microstructure of the porous samples as a result of changing parameters regarding the processing of the samples. Microstructural parameters were determined that could be directly related to processing parameters.

Investigations of the RAMAN spectra led to the conclusion that the samples analyzed in this work consist in pure $BaTiO_3$ in the orthorhombic phase. The introduction of different pore formers before sintering appears not to affect the chemical composition of the samples.

Changes in the RAMAN spectra in C3E, measured at different positions, suggest a coexistence of tetragonal and orthorhombic phase in the sample. The coexistence of the phases is attributed to possible strain of the matrix ($BaTiO_3$) in the sinter process or while cutting the samples.

The next step is to characterize the samples regarding their functional properties, i.e. their dielectric permittivity. This way, a better understanding of the effect of the microstructure on the functional properties of the material can be achieved and proper design guidelines can be established. Studies such as [4] have already applied FEM simulations to investigate the

permittivity of porous $BaTiO_3$. A potential approach includes the segmented 3D representations as input for further FEM simulations to characterize the dielectric properties of the porous $BaTiO_3$ samples, in combination with experimental measurements of the dielectric permittivity of the samples.

The results presented in this work are in preparation for being published in the Journal of the European Ceramic Society.

References

[1] W. E. Lee and W. M. Rainforth, *Ceramic microstructures*, Chapman & Hall, London, 1994.

[2] E. C. Hammel, O.L.-R. Ighodaro, and O. I. Okoli, “Processing and properties of advanced porous ceramics: An application based review,” *Ceramics International*, vol. 40, no. 10, pp. 15351–15370, 2014.

[3] E. Roncari, C. Galassi, F. Craciun et al., “A microstructural study of porous piezoelectric ceramics obtained by different methods,” *Journal of the European Ceramic Society*, vol. 21, no. 3, pp. 409–417, 2001.

[4] R. Stanculescu, C. E. Ciomaga, L. Padurariu et al., “Study of the role of porosity on the functional properties of (Ba,Sr)TiO 3 ceramics,” *Journal of Alloys and Compounds*, vol. 643, pp. 79–87, 2015.

[5] Z. Chen, X. Wang, F. Giuliani et al., “Microstructural characteristics and elastic modulus of porous solids,” *Acta Materialia*, vol. 89, pp. 268–277, 2015.

[6] A. R. Studart, U. T. Gonzenbach, E. Tervoort et al., “Processing Routes to Macroporous Ceramics: A Review,” *Journal of the American Ceramic Society*, vol. 89, no. 6, pp. 1771–1789, 2006.

[7] C. S. Olariu, L. Padurariu, R. Stanculescu et al., “Investigation of low field dielectric properties of anisotropic porous Pb(Zr,Ti)O 3 ceramics: Experiment and modeling,” *Journal of Applied Physics*, vol. 114, no. 21, p. 214101, 2013.

[8] Q. Lin, Y. Al-Khulaifi, M. J. Blunt et al., “Quantification of sub-resolution porosity in carbonate rocks by applying high-salinity contrast brine using X-ray microtomography differential imaging,” *Advances in Water Resources*, vol. 96, pp. 306–322, 2016.

[9] S. V. Kuryntsev and A. K. Gilmutdinov, “The effect of laser beam wobbling mode in welding process for structural steels,” *The International Journal of Advanced Manufacturing Technology*, vol. 81, 9-12, pp. 1683–1691, 2015.

[10] L. C. Chan, X. Z. Lu, and K. M. Yu, “Multiscale approach with RSM for stress–strain behaviour prediction of micro-void-considered metal alloy,” *Materials & Design*, vol. 83, pp. 129–137, 2015.

[11] D. Leitlmeier and Degischer, H. P. & Flankl, H. J., “Development of a Foaming Process for Particulate Reinforced Aluminum Melts,”.

[12] L. Holzer, F. Indutnyi, P. GASSER et al., “Three-dimensional analysis of porous BaTiO3 ceramics using FIB nanotomography,”.

[13] L. Padurariu, L. Curecheriu, C. Galassi et al., “Tailoring non-linear dielectric properties by local field engineering in anisotropic porous ferroelectric structures,” *Applied Physics Letters*, vol. 100, no. 25, p. 252905, 2012.

[14] M. T. Buscaglia, M. Bassoli, V. Buscaglia et al., “Solid-State Synthesis of Ultrafine BaTiO3 Powders from Nanocrystalline BaCO3 and TiO2,” *Journal of the American Ceramic Society*, vol. 88, no. 9, pp. 2374–2379, 2005.

[15] C. Pithan, D. Hennings, and R. Waser, “Progress in the Synthesis of Nanocrystalline BaTiO3 Powders for MLCC,” *International Journal of Applied Ceramic Technology*, vol. 2, no. 1, pp. 1–14, 2005.

[16] H. M. Al-Allak, T. V. Parry, G. J. Russell et al., “Effects of aluminium on the electrical and mechanical properties of PTCR BaTiO3 ceramics as a function of the sintering temperature,” *Journal of Materials Science*, vol. 23, no. 3, pp. 1083–1089, 1988.

[17] K. Park, “Characteristics of porous BaTiO3-based PTC thermistors fabricated by adding graphite powders,” *Materials Science and Engineering: B*, vol. 107, no. 1, pp. 19–26, 2004.

[18] J. I. Roscow, J. Taylor, and C. R. Bowen, “Manufacture and characterization of porous ferroelectrics for piezoelectric energy harvesting applications,” *Ferroelectrics*, vol. 498, no. 1, pp. 40–46, 2016.

[19] M. F. Ashby, T. Evans, N. A. Fleck et al., *Metal foams: a design guide*, Elsevier, 2000.

[20] C. J. Buchko, L. C. Chen, Y. Shen et al., “Processing and microstructural characterization of porous biocompatible protein polymer thin films,” *Polymer*, vol. 40, no. 26, pp. 7397–7407, 1999.

[21] C. Galassi, “Processing of porous ceramics: Piezoelectric materials,” *Journal of the European Ceramic Society*, vol. 26, no. 14, pp. 2951–2958, 2006.

[22] F. F. Lange, “Powder processing science and technology for increased reliability,” *Journal of the American Ceramic Society*, vol. 72, no. 1, pp. 3–15, 1989.

[23] W. M. Sigmund, N. S. Bell, and L. Bergström, “Novel powder-processing methods for advanced ceramics,” *Journal of the American Ceramic Society*, vol. 83, no. 7, pp. 1557–1574, 2000.

[24] L. C. Klein and R. H. Woodmann, “Porous silica by the sol-gel process,” in *Key Engineering Materials*, vol. 115, pp. 109–124, 1996.

[25] J.-G. Kim, “Fabrication of porous Ba (Ti, Sb) O3 ceramics and electrical properties,” *Materials Science and Engineering: A*, vol. 347, 1-2, pp. 306–310, 2003.

[26] Z.-Y. Deng, J.-F. Yang, Y. Beppu et al., “Effect of agglomeration on mechanical properties of porous zirconia fabricated by partial sintering,” *Journal of the American Ceramic Society*, vol. 85, no. 8, pp. 1961–1965, 2002.

[27] D.-M. Liu, “Fabrication of hydroxyapatite ceramic with controlled porosity,” *Journal of materials science: materials in medicine*, vol. 8, no. 4, pp. 227–232, 1997.

[28] J.-G. Kim, J.-H. Sim, and W.-S. Cho, “Preparation of porous (Ba, Sr) TiO3 by adding corn-starch,” *Journal of Physics and Chemistry of Solids*, vol. 63, no. 11, pp. 2079–2084, 2002.

[29] J.-G. Kim, J.-G. Ha, T.-W. Lim et al., “Preparation of porous BaTiO3-based ceramics by high-energy ball-milling process,” *Materials Letters*, vol. 60, no. 12, pp. 1505–1508, 2006.

[30] S. Lautenschlager, “Reconstructing the past: methods and techniques for the digital restoration of fossils,” *Royal Society open science*, vol. 3, no. 10, p. 160342, 2016.

[31] E. H. Lehmann, P. Vontobel, E. Deschler-Erb et al., “Non-invasive studies of objects from cultural heritage,” *Nuclear Instruments and Methods in Physics Research Section A: Accelerators, Spectrometers, Detectors and Associated Equipment*, vol. 542, 1-3, pp. 68–75, 2005.

[32] R. L. Abel, S. Parfitt, N. Ashton et al., “Digital preservation and dissemination of ancient lithic technology with modern micro-CT,” *Computers & Graphics*, vol. 35, no. 4, pp. 878–884, 2011.

[33] E. L. Ritman, “Micro-computed tomography-current status and developments,” *Annual review of biomedical engineering*, vol. 6, pp. 185–208, 2004.

[34] Z. Sun, C. K. C. Ng, and C. S. Dos Reis, “Synchrotron radiation computed tomography versus conventional computed tomography for assessment of four types of stent grafts used for endovascular treatment of thoracic and abdominal aortic aneurysms,” *Quantitative imaging in medicine and surgery*, vol. 8, no. 6, p. 609, 2018.

[35] T. Bultreys, L. van Hoorebeke, and V. Cnudde, “Simulating secondary waterflooding in heterogeneous rocks with variable wettability using an image-based, multiscale pore network model,” *Water Resources Research*, vol. 52, no. 9, pp. 6833–6850, 2016.

[36] Z. Yan, O. Guillon, C. L. Martin et al., “Correlative Studies on Sintering of Ni/BaTiO 3 Multilayers Using X-ray Computed Nanotomography and FIB-SEM Nanotomograhy,” *Journal of the American Ceramic Society*, vol. 98, no. 4, pp. 1338–1346, 2015.

[37] G. J. Ramos, P. C. de Oliveira, R. Surmas et al., “Evaluation of the conventional and synchrotron X-ray tomography applied to heterogeneous oil reservoir rocks,” *Brazilian Journal of Radiation Sciences*, vol. 7, 3A, 2019.

[38] N. A. Seaton, “Determination of the connectivity of porous solids from nitrogen sorption measurements,” *Chemical Engineering Science*, vol. 46, no. 8, pp. 1895–1909, 1991.

[39] M. A. Vicente, J. Mínguez, and D. C. González, “The Use of Computed Tomography to Explore the Microstructure of Materials in Civil Engineering: From Rocks to Concrete,” in *Computed Tomography - Advanced Applications,* A. M. Halefoglu, Ed., InTech, 2017.

[40] G. T. Herman, “Image reconstruction from projections,” *The fundamental of computerized tomography*, pp. 260–276, 1980.

[41] E. N. Landis and D. T. Keane, “X-ray microtomography,” *Materials characterization*, vol. 61, no. 12, pp. 1305–1316, 2010.

[42] V. Cnudde and M. N. Boone, “High-resolution X-ray computed tomography in geosciences: A review of the current technology and applications,” *Earth-Science Reviews*, vol. 123, pp. 1–17, 2013.

[43] F. Arzilli, A. Cilona, L. Mancini et al., “Using synchrotron X-ray microtomography to characterize the pore network of reservoir rocks: A case study on carbonates,” *Advances in Water Resources*, vol. 95, pp. 254–263, 2016.

[44] S. Diamond, “Mercury porosimetry: an inappropriate method for the measurement of pore size distributions in cement-based materials,” *Cement and concrete research*, vol. 30, no. 10, pp. 1517–1525, 2000.

[45] D. Wildenschild and A. P. Sheppard, “X-ray imaging and analysis techniques for quantifying pore-scale structure and processes in subsurface porous medium systems,” *Advances in Water Resources*, vol. 51, pp. 217–246, 2013.

[46] L. M. Keller, L. Holzer, P. Schuetz et al., “Pore space relevant for gas permeability in Opalinus clay: Statistical analysis of homogeneity, percolation, and representative volume element,” *Journal of Geophysical Research: Solid Earth*, vol. 118, no. 6, pp. 2799–2812, 2013.

[47] Thermo Fisher Scientific Inc, “Avizo User’s guide,” https://assets.thermofisher.com/TFS-Assets/MSD/Product-Guides/user-guide-avizo-software.pdf.

[48] S. Jayaraman, S. Esakkirajan, and T. Veerakumar, *Digital Image Processing*, Tata McGraw-Hill Education, 2009.

[49] L. Jin and D. Li, “A switching vector median filter based on the CIELAB color space for color image restoration,” *Signal Processing*, vol. 87, no. 6, pp. 1345–1354, 2007.

[50] Mathworks, “Mathworks documentation/Types of morphological operations,”.

[51] Open CV, “Image Segmentation with Watershed Algorithm,”.

[52] M. Sezgin and B. Sankur, “Survey over image thresholding techniques and quantitative performance evaluation,” *Journal of Electronic imaging*, vol. 13, no. 1, pp. 146–166, 2004.

[53] N. Otsu, “A threshold selection method from gray-level histograms,” *IEEE transactions on systems, man, and cybernetics*, vol. 9, no. 1, pp. 62–66, 1979.

[54] Robert Fisher, Simon Perkins, Ashley Walker and Erik Wolfart, “http://homepages.inf.ed.ac.uk/rbf/HIPR2/skeleton.htm,”.

[55] scikit-image library, “Skeletonize (scikit),”.

[56] S. D. N. Lourenço, “Wettability of crushed air-dried minerals,” *Géotechnique Letters*, vol. 5, July–September, pp. 173–177, 2015.

[57] L. Opilik, T. Schmid, and R. Zenobi, “Modern Raman imaging: vibrational spectroscopy on the micrometer and nanometer scales,” 2013.

[58] H. Hayashi, T. Nakamura, and T. Ebina, “In-situ Raman spectroscopy of BaTiO3 particles for tetragonal–cubic transformation,” *Journal of Physics and Chemistry of Solids*, vol. 74, no. 7, pp. 957–962, 2013.

[59] R. L. McCreery, *Raman spectroscopy for chemical analysis*, John Wiley & Sons, 2005.

[60] G. Philippot, M. Albino, R. Epherre et al., “Local Distortions in Nanostructured Ferroelectric Ceramics through Strain Tuning,” *Advanced Electronic Materials*, vol. 1, no. 10, p. 1500190, 2015.

[61] L. Bokobza, J.-L. Bruneel, and M. Couzi, “Raman Spectra of Carbon-Based Materials (from Graphite to Carbon Black) and of Some Silicone Composites,” *C*, vol. 1, no. 1, pp. 77–94, 2015.

[62] R. Hardis, J. L.P. Jessop, F. E. Peters et al., “Cure kinetics characterization and monitoring of an epoxy resin using DSC, Raman spectroscopy, and DEA,” *Composites Part A: Applied Science and Manufacturing*, vol. 49, pp. 100–108, 2013.

[63] Y. Ji, Y. He, Y. Cui et al., “Raman spectroscopy provides a rapid, non-invasive method for quantitation of starch in live, unicellular microalgae,” *Biotechnology journal*, vol. 9, no. 12, pp. 1512–1518, 2014.

[64] P. Graves and D. Gardiner, “Practical raman spectroscopy,” *Springer*, 1989.

[65] Z. Xu, Z. He, Y. Song et al., “Topic Review: Application of Raman Spectroscopy Characterization in Micro/Nano-Machining,” *Micromachines*, vol. 9, no. 7, p. 361, 2018.

[66] G. W. Gee and D. Or, “2.4 Particle-size analysis,” *Methods of soil analysis. Part*, vol. 4, no. 598, pp. 255–293, 2002.

[67] Y. Shiratori, C. Pithan, J. Dornseiffer et al., “Raman scattering studies on nanocrystalline BaTiO3 Part I—isolated particles and aggregates,” *Journal of Raman Spectroscopy*, vol. 38, no. 10, pp. 1288–1299, 2007.

[68] A. A. Kholodkova, M. N. Danchevskaya, Y. D. Ivakin et al., “Crystalline barium titanate synthesized in sub- and supercritical water,” *The Journal of Supercritical Fluids*, vol. 117, pp. 194–202, 2016.

[69] Horiba France SAS, “Labram HR Evolution,”.

[70] J. Fernlund, “The effect of particle form on sieve analysis: a test by image analysis,” *Engineering Geology*, vol. 50, 1-2, pp. 111–124, 1998.

[71] A. Gajović, J. V. Pleština, K. Žagar et al., “Temperature-dependent Raman spectroscopy of BaTiO 3 nanorods synthesized by using a template-assisted sol-gel procedure,” *Journal of Raman Spectroscopy*, vol. 44, no. 3, pp. 412–420, 2013.

[72] W. H. Weber, K. C. Hass, and McBride, JR, “Raman study of CeO 2: second-order scattering, lattice dynamics, and particle-size effects,” *Physical Review B*, vol. 48, no. 1, p. 178, 1993.

[73] P. McMillan and N. Ross, “The Raman spectra of several orthorhombic calcium oxide perovskites,” *Physics and Chemistry of Minerals*, vol. 16, no. 1, pp. 21–28, 1988.

[74] Min-Su Jang, Masaaki Takashige, Seiji Kojima et al., “Oblique Phonons with Special Concern to the Soft Phonon in Tetragonal BaTiO3,”.

[75] M. El Marssi, F. Le Marrec, I. A. Lukyanchuk et al., “Ferroelectric transition in an epitaxial barium titanate thin film: Raman spectroscopy and x-ray diffraction study,” *Journal of Applied Physics*, vol. 94, no. 5, pp. 3307–3312, 2003.

[76] M. Nakajima, T. Fujisawa, K. Nishida et al., “Polarized Raman Study for Epitaxial PZT Thick Film with the Mixture Orientation of (100)/(001),” *Key Engineering Materials*, 421-422, pp. 99–102, 2009.

[77] M. H. Frey and D. A. Payne, “Grain-size effect on structure and phase transformations for barium titanate,” *Physical Review B*, 54.5, no. 3158, 1996.